

RAY BASED FINITE DIFFERENCE METHOD  
FOR TIME DOMAIN ELECTROMAGNETICS

A THESIS SUBMITTED TO  
THE GRADUATE SCHOOL OF NATURAL AND APPLIED SCIENCES  
OF  
MIDDLE EAST TECHNICAL UNIVERSITY

BY

MEHMET ÇİYDEM

IN PARTIAL FULFILLMENT OF THE REQUIREMENTS FOR THE DEGREE  
OF  
DOCTOR OF PHILOSOPHY  
IN  
ELECTRICAL AND ELECTRONICS ENGINEERING

SEPTEMBER 2005

Approval of the Graduate School of Natural and Applied Sciences

---

Prof. Dr. Canan ÖZGEN  
Director

I certify that this thesis satisfies all the requirements as a thesis for the degree of Doctor of Philosophy.

---

Prof. Dr. İsmet ERKMEN  
Head of Department

This is to certify that we have read this thesis and that in our opinion it is fully adequate, in scope and quality, as a thesis for the degree of Doctor of Philosophy.

---

Doç. Dr. S. Sencer KOÇ  
Supervisor

Examining Committee Members (first name belongs to the chairperson of the jury and the second name belongs to supervisor)

Prof. Dr. Mustafa KUZUOĞLU	(METU, EE)	_____
Doç. Dr. S. Sencer KOÇ	(METU, EE)	_____
Prof. Dr. Ayhan ALTINTAŞ	(Bilkent Üniv., EE)	_____
Doç. Dr. Özlem AYDIN ÇİVİ	(METU, EE)	_____
Yrd. Doç. Dr. Vakur B. ERTÜRK	(Bilkent Üniv., EE)	_____

**I hereby declare that all information in this document has been obtained and presented in accordance with academic rules and ethical conduct. I also declare that, as required by these rules and conduct, I have fully cited and referenced all material and results that are not original to this work.**

Name, Last name : MEHMET ÇİYDEM

Signature :

## ABSTRACT

### RAY BASED FINITE DIFFERENCE METHOD FOR TIME DOMAIN ELECTROMAGNETICS

Çiydem, Mehmet

Ph.D., Department of Electrical and Electronics Engineering

Supervisor : Doç. Dr. S. Sencer KOÇ

September 2005, 130 pages

In this study, novel Ray Based finite difference method for Time Domain electromagnetics (RBTD) has been developed. Instead of solving Maxwell's hyperbolic partial differential equations directly, Geometrical Optics tools (wavefronts, rays) and Taylor series have been utilized. Discontinuities of electromagnetic fields lie on wavefronts and propagate along rays. They are transported in the computational domain by transport equations which are ordinary differential equations. Then time dependent field solutions at a point are constructed by using Taylor series expansion in time whose coefficients are these transported discontinuities. RBTD utilizes grid structure conforming to wave fronts and rays and treats all electromagnetic problems, regardless of their dimensions, as one dimensional problem along the rays. Hence CFL stability condition is implemented always at one dimensional equality case on the ray. Accuracy of RBTD depends on the accuracy of grid generation and numerical solution of transport equations. Simulations for isotropic medium (homogeneous/inhomogeneous) have been conducted. Basic electromagnetic phenomena such as propagation, reflection and refraction have been implemented. Simulation results prove that RBTD eliminates numerical dispersion inherent to FDTD and is promising to be a novel method for computational electromagnetics.

Keywords: Geometrical Optics, Wave front, Ray, Discontinuity, Finite Differences, Taylor series.

## ÖZ

### ZAMANSAL ELEKTROMANYETİK İÇİN IŞIN TABANLI SONLU FARKLAR YÖNTEMİ

Çiydem, Mehmet

Doktora, Elektrik ve Elektronik Mühendisliği Bölümü

Tez Yöneticisi : Doç. Dr. S. Sencer KOÇ

Eylül 2005, 130 sayfa

Bu çalışmada, Zamansal elektromanyetik için, yeni bir Işın Tabanlı sonlu farklar Yöntemi (ITZY) geliştirilmiştir. Hiperbolik Maxwell kısmi türev denklemlerini doğrudan çözmek yerine; Geometrik Optik araçları (dalga cepheleri, ışınlar) ve Taylor serisinden yararlanılmıştır. Elektromanyetik alan kesintileri dalga cepheleri üzerinde bulunur ve ışın çizgileri boyunca yayılırlar. Bunlar, adi türev denklemleri olan taşıma denklemleri ile hesaplama ızgarasında taşınırlar. Daha sonra herhangi bir noktada, katsayıları bu kesintiler olan Taylor serisi marifetiyle zamansal elektromanyetik alan çözümleri oluşturulur. ITZY’de hesaplama ızgarasının dalga cepheleri ve ışınlar ile örtüşmesi gerekmektedir. ITZY tüm elektromanyetik problemleri ışınlar boyunca tek boyutlu probleme indirgemektedir. Bunun neticesi olarak, CFL kararlılık şartı ışın üzerinde hep eşitlik halinde tek boyutlu gerçekleşmiştir. ITZY’nin doğruluğu, hesaplama ızgarasının ve taşıma denklemlerinin sayısal çözümlerinin doğruluğuna bağlıdır. Homojen/inhomojen yönsüz ortamda benzetimler ile, yayılım, kırılım ve yansıma gibi temel elektromanyetik olaylar gösterilmiştir. Sonuçlar, ITZY’nin FDTD’de kalıtsal varolan sayısal saçınımı ortadan kaldırdığını ve etkin bir yöntem olarak gelecekte sayısal elektromanyetikte kullanılabileceğini göstermektedir.

Anahtar Kelimeler: Geometrik Optik, Dalga cephesi, Işın, Kesinti, Sonlu Farklar, Taylor serisi

## TABLE OF CONTENTS

<b>1</b>	<b><u>INTRODUCTION.....</u></b>	<b>1</b>
1.1	Contents.....	1
1.2	Achievements.....	2
<b>2</b>	<b><u>MAXWELL'S EQUATIONS.....</u></b>	<b>3</b>
2.1	Introduction.....	3
2.2	Basic Facts about Maxwell's Equations.....	3
2.3	Constitutive Relations.....	5
2.4	Power and Energy Stored.....	5
2.5	Electromagnetic Boundary Conditions.....	6
2.6	Wave Equation.....	7
<b>3</b>	<b><u>COMPUTATIONAL ELECTROMAGNETICS.....</u></b>	<b>8</b>
3.1	Introduction.....	8
3.2	History of Computational Electromagnetics.....	8
3.3	Classification of Electromagnetic Problems.....	12
3.4	Classification of Methods of Solutions of Maxwell's Equations.....	12
3.5	Capabilities of Methods of Solution.....	15
3.6	Features of Time Domain Finite Methods.....	15
3.6.1	Grid Structure.....	15
3.6.2	Numerical Dispersion.....	17
3.6.3	Numerical Stability.....	20
3.6.4	Absorbing Boundary Conditions.....	22
3.7	Characteristic Based Methods for Solutions of Maxwell's Equations.....	23
3.7.1	Method of Characteristic for Hyperbolic PDEs.....	23
3.7.2	Application to Maxwell's Equations.....	27
<b>4</b>	<b><u>ELECTROMAGNETIC APPROACH TO GEOMETRICAL OPTICS.....</u></b>	<b>30</b>
4.1	Introduction.....	30

4.2	Maxwell's Equations and Discontinuous Solutions .....	30
4.3	Discontinuity Conditions .....	31
4.4	Types of Discontinuity Hypersurfaces .....	33
4.5	Geometrical Optics .....	35
4.5.1	Definition of Geometrical Optics .....	35
4.5.2	Wave Fronts and Rays .....	35
4.5.3	Fermat's Principle.....	38
4.5.4	Power and Energy.....	38
4.5.5	Propagation of Geometrical Optics Fields.....	39
4.5.6	Solution of Transport Equations .....	40
4.5.7	Reflection/Refraction Across Discontinuity in the Medium.....	41
<b>5</b>	<b><u>GEOMETRICAL OPTICS FOR TIME-DOMAIN ELECTROMAGNETICS.....</u></b>	<b>47</b>
5.1	Introduction.....	47
5.2	Discontinuity Conditions for Higher Discontinuities .....	49
5.3	Propagation of Higher Discontinuities .....	51
5.4	Solutions of Higher Transport Equations .....	53
5.5	Initial Values for Transport Equations.....	54
5.6	Reconstruction of Time-Dependent Electromagnetic Fields.....	57
<b>6</b>	<b><u>NUMERICAL STUDIES.....</u></b>	<b>61</b>
6.1	Introduction.....	61
6.2	Sample Problem I: 1-D Propagating Plane Wave.....	61
6.2.1	Computational Grid .....	61
6.2.2	FDTD Implementation.....	62
6.2.2.1	Rectangular Pulse .....	63
6.2.2.2	Gaussian Pulse .....	66
6.2.3	RBTD Implementation .....	70
6.2.3.1	Rectangular Pulse .....	70
6.2.3.2	Gaussian Pulse .....	71
6.3	Sample Problem II: 1-D Plane Wave with Dielectric Interface.....	72
6.3.1	Computational Grid .....	72
6.3.2	FDTD Implementation.....	73
6.3.2.1	Rectangular Pulse .....	74

6.3.2.2	Gaussian Pulse .....	76
6.3.3	RBTD Implementation .....	78
6.3.3.1	Rectangular Pulse .....	80
6.3.3.2	Gaussian Pulse .....	81
6.4	Sample Problem III: Electric Dipole in Homogeneous Medium .....	83
6.4.1	Computational Grid .....	84
6.4.2	Spherical FDTD Implementation.....	85
6.4.2.1	Ramp Pulse .....	86
6.4.2.2	Gaussian Pulse .....	89
6.4.3	RBTD Implementation .....	92
6.4.3.1	Ramp Pulse .....	96
6.4.3.2	Gaussian Pulse .....	99
6.5	Sample Problem IV: Electric Dipole in Inhomogeneous Medium .....	102
6.5.1	Computational Grid .....	102
6.5.2	Spherical FDTD Implementation.....	103
6.5.3	Conformal FDTD Implementation .....	106
6.5.4	RBTD Implementation .....	111
6.6	Stability of Transport Equations .....	116
6.7	Grid Generation .....	116
6.8	Accuracy of RBTD .....	117
<b>7</b>	<b><u>CONCLUSION.....</u></b>	<b>119</b>
7.1	Conclusion.....	119
7.2	Further Study .....	121
	<b><u>BIBLIOGRAHPY.....</u></b>	<b>123</b>
	<b><u>CURRICULLUM VITA.....</u></b>	<b>130</b>

## LIST OF SYMBOLS

<b>Symbol</b>	<b>Description</b>	<b>Unit</b>
<b>E</b>	Electric field intensity	V/m
<b>D</b>	Electric flux density	C/m <sup>2</sup>
<b>H</b>	Magnetic field intensity	A/m
<b>B</b>	Magnetic flux density	Wb/ m <sup>2</sup>
<b>J</b>	Volume current density	A/m <sup>2</sup>
<b>J<sub>s</sub></b>	Surface current density	A/m
$\rho$	Volume charge density	C/m <sup>3</sup>
$\rho_s$	Surface charge density	C/m <sup>2</sup>
$\sigma$	Conductivity	mho/m
$\epsilon$	Permittivity of medium	F/m
$\epsilon_0$	$8.854 \times 10^{-12}$ (permittivity of free-space)	F/m
$\epsilon_r$	Relative permittivity	
$\mu$	Permeability of medium	H/m
$\mu_0$	$4\pi \times 10^{-7}$ (permeability of free-space)	H/m
$\mu_r$	Relative permeability	
n	Index of medium (index of refraction)	
c	299792458 (speed of light)	m/s
$v$	Phase velocity in a medium	m/s
$v_g$	Group velocity in a medium	m/s
<b>S</b>	Poynting vector	W/m <sup>2</sup>
$w_e$	Electric stored energy	J/ m <sup>3</sup>
$w_m$	Magnetic stored energy	J/ m <sup>3</sup>
$P_d$	Dissipated energy density (ohmic loss)	W/ m <sup>3</sup>

## LIST OF ABBREVIATIONS

ABC:	Absorbing Boundary Condition	MoC:	Method of Characteristics
AIAA:	American Institute of Aeronautics and Astronautics	MoM:	Method of Moments
AP:	Antennas & Propagation	MRTD:	Multi Resolution Time Domain
BC:	Boundary Condition	MTT:	Microwave Theory & Techniques
CFD:	Computational Fluid Dynamics	ODE:	Ordinary Differential Equation
CFL:	Courant-Friedrich-Lewy	PDE:	Partial Differential Equation
CEM:	Computational Electromagnetics	PEC:	Perfect Electric Conductor
CP:	Contour Path	PMC:	Perfect Magnetic Conductor
DE:	Differential Equation or Difference Equation	PML:	Perfectly Matched Layer
DSI:	Discret Surface Integral	PO:	Physical Optics
EM:	Electromagnetic	PTD:	Physical Theory of Diffraction
EMC:	Electromagnetic Compatibility	PSTD:	Pseudo Spectral Time Domain
FD:	Frequency Domain or Finite Difference	PW	Plane Wave
FDDE:	Frequency Domain Differential Equation	RBC:	Radiation Boundary Condition
FDIE:	Frequency Domain Integral Equation	RBTD:	Ray Based Finite Difference
FDTD:	Finite Difference Time Domain	RCS:	Radar Cross Section
FETD:	Finite Element Time Domain	STD:	Spectral Theory of Diffraction
FVTD:	Finite Volume Time Domain	TD:	Time Domain
GO:	Geometrical Optics	TDDE:	Time Domain Differential Equation
GTD:	Geometrical Theory of Diffraction	TDIE:	Time Domain Integral Equation
GY:	Generalized Yee	TDGO:	Time Domain Geometrical Optics
HF:	High Frequency	TDRO:	Time Domain Ray Optics
IC:	Initial Condition	TLM:	Transmission Line Matrix
IE:	Integral Equation	TEM	Transverse Electromagnetic
IEEE:	Institute of Electrical and Electronics Engineers	TSF:	Thin Slot Formulation
ITD:	Incremental Theory of Diffraction	UAT:	Uniform Asymptotic Theory
LPF:	Low Pass Filter	UTD:	Uniform Theory of Diffraction

# CHAPTER 1

## INTRODUCTION

### 1.1 Contents

Underlying motivation behind this study has been to develop dispersion free numerical algorithms for computational electromagnetics (CEM) because one of the major CEM methods, Finite Difference Time Domain (FDTD), is inherently dispersive. Toward this end, many CEM methods in literature have been studied. Finally we have ended up with novel method, called Ray Based Time Domain (RBTD) method by us, for the computation of time-dependent electromagnetic (EM) fields.

Chapter 2 discusses Maxwell's equations, which are 1<sup>st</sup> order Partial Differential Equations (PDEs), and fundamentals of EM theory. Chapter 3 presents a historical survey of CEM methods in literature and discusses basic features of time domain finite methods with an emphasis on FDTD, Finite Volume Time Domain (FVTD) and characteristic-based methods. Grid structures, numerical dispersion, stability, and absorbing boundary condition (ABC) features are investigated. Although characteristic-based methods have many advantageous such as well-posedness, directional signal propagation, which improves the stability, numerical dispersion performance, and ease of ABC implementation, the coefficient matrix of governing equation *cannot be diagonalised in higher dimensions*. FDTD is very popular method for EM simulations and is widely used. The main drawback of FDTD is inherent *numerical dispersion*. There are two main factors causing numerical dispersion: discretization of PDE Maxwell's equations (grid resolution, wavelength, time step) and propagation direction of wave in the grid. FDTD must obey CFL stability condition. There exists also *superluminal effect* in FDTD resulting from some modes traveling faster than light in the grid.

In Chapter 4 and 5, which are the main contributions of this thesis, we have introduced how to utilize Geometrical Optics (GO) to remedy above drawbacks of time domain finite methods. GO tools such as discontinuity, discontinuity hypersurfaces, wave fronts, rays have been explained in Chapter 4 from EM approach. Then this theory has been extended to include higher order discontinuities to construct time dependent EM fields in Chapter 5.

RBTD deals with discontinuities of field quantities, transport of them along rays (incident, reflected, refracted), and reflection/refraction of them at a boundary interface. After RBTD computes discontinuities in the computational domain, then it constructs time-dependent field by using Taylor series with coefficients being discontinuities at the point of interest. Chapter 6 presents numerous EM simulations for propagation, reflection and refraction of waves in isotropic homogeneous/inhomogeneous medium. Results for both FDTD and RBTD have been provided and compared. Then thesis concludes with Chapter 7 including conclusion and further study.

## 1.2 Achievements

In addition to RBTD, we have devised a novel grid structure for FDTD, which is *Conformal FDTD*, and observed that this approach removes dependence of numerical dispersion to propagation direction because grid conforming to wave fronts and rays has been aligned to follow ray direction. Then numerical dispersion only due to discretization of PDE remains left. To the best of our knowledge, conformal gridding in this sense for FDTD has been developed and implemented first in this thesis.

RBTD is also based on characteristic theory of PDEs because grid structure of RBTD has to be wave fronts and rays, which are the characteristics and bicharacteristics of PDEs. Thus RBTD preserve the advantageous of characteristic-based methods but does not deal with any matrix diagonalisation.

Honoring directional signal propagation and Ordinary Differential Equation (ODE) nature of transport equations provide to eradicate the numerical dispersion, which is the biggest advantage of RBTD over FDTD. RBTD not only eliminates *numerical dispersion* but also eliminates *superluminal effects* of FDTD. Contrary to FDTD, RBTD works on one of the field quantities, either **E** or **H**. FDTD must satisfy CFL stability condition while RBTD implements 1-D CFL condition (*magic time step*) along the rays. No matter what the dimension of problem is, it is treated as 1-D by RBTD. FDTD needs ABCs at the end of the computational domain. However in RBTD, after performing some pre-processing, discontinuities are determined and transported into computational domain as a spatial problem only. Hence no need to apply ABCs.

As far as the type of input waveform is concerned, there is no limitation for RBTD (smooth or discontinuous) whereas FDTD needs smooth excitations. However it is preferable to find the solution first for simple waveforms such as step, ramp or rectangular pulses. Then one can construct the response to an arbitrary waveform from the response of simpler waveform.

## CHAPTER 2

### MAXWELL'S EQUATIONS

#### 2.1 Introduction

Before Maxwell's work, many scientists studied the relationship between electricity and magnetism, but it was Maxwell who established the fundamental unification of electric and magnetic fields predicting electromagnetic wave phenomena. Nobel Laureate Richard Feynman has called it as the most outstanding achievement of 19<sup>th</sup>-century science. Maxwell's partial differential equations (PDEs) describe dynamic nature of electromagnetic (EM) phenomena. They are 1<sup>st</sup> order systems of linear hyperbolic PDEs relating electric and magnetic fields.

#### 2.2 Basic Facts about Maxwell's Equations

The electric part of the EM field governed by Maxwell's equations is described by two vectors  $\mathbf{D}(x,y,z,t)$  and  $\mathbf{E}(x,y,z,t)$  which are called *electric flux density* and *electric field strength* respectively. Associated with the vector field  $\mathbf{D}$  is the scalar function  $\rho(x,y,z,t)$ , which specifies the *charge density* (source charges and free charges in a conducting medium). The magnetic part of the EM field is described by two vectors  $\mathbf{B}(x,y,z,t)$  and  $\mathbf{H}(x,y,z,t)$ .  $\mathbf{B}$  is called *magnetic flux density*, and  $\mathbf{H}$  the *magnetic field strength*. Whenever there is any motion of charges, there also exists *current density*, namely  $\mathbf{J}(x,y,z,t)$ . Then Maxwell's equations in time domain (TD) can be expressed both in differential form and integral form as:

Table 2-1: Maxwell's equations in time domain

Differential form	Integral form
$\nabla \times \mathbf{E} = -\frac{\partial \mathbf{B}}{\partial t}$	$\int_C \mathbf{E} \cdot d\ell = -\int_A \left(\frac{\partial \mathbf{B}}{\partial t}\right) \cdot d\mathbf{A}$
$\nabla \times \mathbf{H} = \mathbf{J} + \frac{\partial \mathbf{D}}{\partial t}$	$\int_C \mathbf{H} \cdot d\ell = \int_A \left(\mathbf{J} + \frac{\partial \mathbf{D}}{\partial t}\right) \cdot d\mathbf{A}$
$\nabla \cdot \mathbf{D} = \rho$	$\int_A \mathbf{D} \cdot d\mathbf{A} = \int_V \rho dV$
$\nabla \cdot \mathbf{B} = 0$	$\int_A \mathbf{B} \cdot d\mathbf{A} = 0$

The first equations in Table 2-1 are known as Faraday's law (or Lenz law) and state that the work done by the electric field (*electromotive force*) on a unit electric charge carried around closed path  $C$  is equal to the time rate of decrease of the flux of magnetic induction through surface  $A$ . The second ones are Maxwell's generalization of Ampere's law and state that the work done by the magnetic field (*magnetomotive force*) on a unit magnetic charge carried around  $C$  is equal to the flux of the total current through  $A$ . In any volume  $V$  bounded by a surface  $A$ , the third equations, known as Gauss law, relate vector field  $\mathbf{D}$  on  $A$  to total charge in  $V$ . And the last ones are the restatement of a physical fact that no isolated magnetic charges exist in nature.

In frequency domain (FD) with  $e^{j\omega t}$  time convention, field variables and sources are phasors with angular frequency  $\omega$  dependence, that is,  $\mathbf{D}(x,y,z,\omega)$ ,  $\mathbf{E}(x,y,z,\omega)$ ,  $\mathbf{B}(x,y,z,\omega)$ ,  $\mathbf{H}(x,y,z,\omega)$  and  $\mathbf{J}(x,y,z,\omega)$ . Then Maxwell's equations can be rewritten as in Table 2-2.

Table 2-2: Maxwell's equations in frequency domain

Differential form	Integral form
$\nabla \times \mathbf{E} = -j\omega \mathbf{B}$	$\int_C \mathbf{E} \cdot d\ell = -j\omega \int_A \mathbf{B} \cdot d\mathbf{A}$
$\nabla \times \mathbf{H} = \mathbf{J} + j\omega \mathbf{D}$	$\int_C \mathbf{H} \cdot d\ell = \int_A (\mathbf{J} + j\omega \mathbf{D}) \cdot d\mathbf{A}$
$\nabla \cdot \mathbf{D} = \rho$	$\int_A \mathbf{D} \cdot d\mathbf{A} = \int_V \rho dV$
$\nabla \cdot \mathbf{B} = 0$	$\int_A \mathbf{B} \cdot d\mathbf{A} = 0$

Maxwell's equations are also consistent with conservation of charge, which is represented by *equation of continuity* for current density  $\mathbf{J}$ .

$$\nabla \cdot \mathbf{J} + \frac{\partial \rho}{\partial t} = 0 \quad (2.1)$$

It is convenient to regard  $\mathbf{J}$  as consisting of two parts: conduction current density  $\mathbf{J}_c$  and source current density (forced)  $\mathbf{J}_f$ .

$$\mathbf{J} = \mathbf{J}_f + \mathbf{J}_c \quad (2.2)$$

Although Maxwell's equations consist of four vector equations they are not all independent. Two divergence equations can be derived from two curl equations and the continuity equation by assuming zero initial conditions (ICs) for fields. Hence the following equations with proper ICs and boundary conditions (BCs) define an EM problem completely.

$$\nabla \times \mathbf{E} = -\frac{\partial \mathbf{B}}{\partial t}, \quad \nabla \times \mathbf{H} = \mathbf{J} + \frac{\partial \mathbf{D}}{\partial t} \quad (2.3)$$

### 2.3 Constitutive Relations

Eqn(2.3) relating four fundamental vectors  $\mathbf{E}$ ,  $\mathbf{D}$ ,  $\mathbf{H}$ , and  $\mathbf{B}$ , each having three components, represents twelve unknowns (field variables). System of differential equations (DE) is underdetermined since there are fewer equations than number of unknowns. Additional relations come from the physical nature of the medium called *constitutive relations*.

In *isotropic* medium, parameters  $\varepsilon$  (*permittivity*),  $\mu$  (*permeability*), and  $\sigma$  (*conductivity*) are scalars. If they are functions of  $(x,y,z)$  the medium is said to be *inhomogeneous*. Otherwise it is *homogeneous*. EM field vectors are related to each other in isotropic medium as follows:

$$\mathbf{D} = \varepsilon \mathbf{E}, \quad \mathbf{B} = \mu \mathbf{H}, \quad \mathbf{J}_c = \sigma \mathbf{E} \quad (2.4)$$

An *anisotropic* medium is again characterized by three medium parameters  $\boldsymbol{\varepsilon}$ ,  $\boldsymbol{\mu}$ ,  $\boldsymbol{\sigma}$  which are real, symmetric, positive definite matrices whose elements are functions of  $(x,y,z)$  in *inhomogeneous* medium and constants in *homogeneous* medium. In this case the relationships among field vectors are given as:

$$\mathbf{D} = \boldsymbol{\varepsilon} \mathbf{E}, \quad \mathbf{B} = \boldsymbol{\mu} \mathbf{H}, \quad \mathbf{J}_c = \boldsymbol{\sigma} \mathbf{E} \quad (2.5)$$

Now Maxwell's curl equations, Eqn(2.3), represent a determined system of PDEs with six equations for six field components ( $E_x, E_y, E_z, H_x, H_y, H_z$ ) in Cartesian coordinates. Then one can determine  $\mathbf{E}$  and  $\mathbf{H}$  uniquely with proper ICs/BCs.

Some additional remarks regarding medium parameters are in order. The medium in which the medium parameters are functions of frequency i.e.,  $\varepsilon(\omega)$ ,  $\mu(\omega)$ ,  $\sigma(\omega)$  are called *dispersive*. In *dispersive* media, *phase velocity*  $v$  is a function of  $\omega$ , which means that modulated or pulsed signal spreads and disperses as it propagates. This leads to the definition of *group velocity*  $v_g$ , the velocity of energy or information travel, which must necessarily consist of some collection of frequencies. If the medium parameters depend on field quantities (in powers or in other *nonlinear* way) such as  $\varepsilon(\mathbf{E})$ ,  $\mu(\mathbf{H})$  then it is said to be *nonlinear*. Expectedly, in *time-invariant* medium, medium parameters do not change with time. On the other hand, *time-varying* medium may have  $\varepsilon(t)$  or  $\mu(t)$ .

### 2.4 Power and Energy Stored

In electromagnetics, power and energy of EM fields is studied by means of *Poynting's theorem* which is mathematically

$$-\int_A (\mathbf{E} \times \mathbf{H}) \cdot d\mathbf{A} = \int_V \frac{\partial}{\partial t} (w_e + w_m) dV + \int_V (\mathbf{E} \cdot \mathbf{J}_c) dV \quad (2.6)$$

It describes the law of conservation of energy in a closed EM system in which no source is present. The law states that the time rate of decrease of EM energy in volume  $V$  is equal to the rate of increase of ohmic losses (heat) in  $V$  plus the radiation flowing out through the closed surface  $A$ . The *Poynting vector*  $\mathbf{S}(x,y,z,t)$  for instantaneous power flow is defined as:

$$\mathbf{S} = \mathbf{E} \times \mathbf{H} \quad (2.7)$$

The direction of  $\mathbf{S}$  gives us the direction of power flow. In Eqn(2.6),  $w_e$ ,  $w_m$ , and  $P_d$  stand for stored instantaneous *electric, magnetic energy densities* and *dissipated ohmic energy* respectively and are given by

$$w_e = \frac{1}{2} \mathbf{E} \cdot \mathbf{D}, \quad w_m = \frac{1}{2} \mathbf{H} \cdot \mathbf{B}, \quad P_d = \mathbf{E} \cdot \mathbf{J}_c = \sigma |\mathbf{E}|^2 \quad (2.8)$$

For time-harmonic fields ( $e^{j\omega t}$  convention), Poynting vector is

$$\mathbf{S} = \mathbf{Re} \{ \mathbf{E} e^{j\omega t} \} \times \mathbf{Re} \{ \mathbf{H} e^{j\omega t} \} \quad (2.9)$$

where  $\mathbf{E}$  and  $\mathbf{H}$  are phasors of  $\mathbf{E}$  and  $\mathbf{H}$  respectively. They are functions of  $(x,y,z)$  and can be complex vectors. Practically, average power density is more important and is found to be

$$\mathbf{S}_{\text{ave}} = \frac{1}{2} \mathbf{Re} \{ \mathbf{E} \times \mathbf{H}' \} \quad (2.10)$$

$\mathbf{E} \times \mathbf{H}'$  is called as complex Poynting vector where superscript ' indicates complex conjugate.

## 2.5 Electromagnetic Boundary Conditions

Maxwell's equations can be applied for any media to obtain the solution. But for the solution to be unique, they must satisfy the EM boundary conditions at the boundary separating the two media. To obtain these conditions, integral forms of Maxwell's equations are used. For this purpose, fields are resolved into tangential components, which are parallel to boundary, and normal components, which are perpendicular to boundary. At the boundary, EM fields satisfy the following conditions at any point  $(x,y,z)$  in time and frequency.

$$[\mathbf{n} \times \mathbf{E}] = \mathbf{n} \times (\mathbf{E}_1 - \mathbf{E}_2) = 0 \quad (2.11)$$

$$[\mathbf{n} \times \mathbf{H}] = \mathbf{n} \times (\mathbf{H}_1 - \mathbf{H}_2) = \mathbf{J}_s \quad (2.12)$$

$$[\mathbf{n} \cdot \mathbf{D}] = \mathbf{n} \cdot (\mathbf{D}_1 - \mathbf{D}_2) = \rho_s \quad (2.13)$$

$$[\mathbf{n} \cdot \mathbf{B}] = \mathbf{n} \cdot (\mathbf{B}_1 - \mathbf{B}_2) = 0 \quad (2.14)$$

where  $\mathbf{n}$ ,  $\mathbf{J}_s$ , and  $\rho_s$  are the unit normal vector to the boundary, surface current density and surface charge density respectively. Eqns(2.11), (2.14) state that tangential components of  $\mathbf{E}$  and normal components of  $\mathbf{B}$  are continuous across the boundary. But tangential components

of  $\mathbf{H}$  and normal components of  $\mathbf{D}$  are discontinuous by an amount of surface current density  $\mathbf{J}_s$  and surface charge density  $\rho_s$  as in Eqns(2.12), (2.13).

## 2.6 Wave Equation

Stated earlier, there are two independent, coupled, 1<sup>st</sup> order PDEs among Maxwell's equations, namely Eqn(2.3) relating  $\mathbf{E}$  and  $\mathbf{H}$ . Eliminating one of the fields, a 2<sup>nd</sup> order PDE can be obtained for the field. And that PDE is to be solved for the problem of interest with a proper method subject to ICs/BCs. In isotropic medium, one can obtain the following for  $\mathbf{E}$ .

$$\nabla^2 \mathbf{E} - \varepsilon\mu \frac{\partial^2 \mathbf{E}}{\partial t^2} = \mu \frac{\partial \mathbf{J}}{\partial t} + \nabla(\nabla \cdot \mathbf{E}) \quad (2.15)$$

In source free, nonconducting medium, Eqn(2.15) becomes

$$\nabla^2 \mathbf{E} - \varepsilon\mu \frac{\partial^2 \mathbf{E}}{\partial t^2} = 0 \quad (2.16)$$

This is generally referred to as vector *wave equation* in  $(x,y,z,t)$ -space. Noting that the permeability and permittivity of medium are in the form of

$$\mu = \mu_0 \mu_r, \quad \varepsilon = \varepsilon_0 \varepsilon_r \quad (2.17)$$

where  $\mu_0$ ,  $\mu_r$ ,  $\varepsilon_0$ , and  $\varepsilon_r$  are permeability of free space, relative permeability of medium, permittivity of free space and relative permittivity of medium respectively. Then Eqn(2.16) is expressed as:

$$\nabla^2 \mathbf{E} - \frac{\partial^2 \mathbf{E}}{\nu^2 \partial t^2} = \nabla^2 \mathbf{E} - \frac{\varepsilon_r \mu_r}{c^2} \frac{\partial^2 \mathbf{E}}{\partial t^2} = 0 \quad (2.18)$$

$\nu = (\varepsilon\mu)^{-1/2}$  and  $c = (\varepsilon_0\mu_0)^{-1/2}$  are phase velocity and speed of light respectively. For 1-D problems in homogeneous medium, differential operators acting on  $\mathbf{E}$  can be factorized as:

$$\left(\frac{\partial}{\partial x} - \frac{\partial}{\nu \partial t}\right) \left(\frac{\partial}{\partial x} + \frac{\partial}{\nu \partial t}\right) \mathbf{E} = 0 \quad (2.19)$$

Total solution  $\mathbf{E}(x,t)$  can be constructed as sum of right and left propagating waves with  $\nu$ .

$$\mathbf{E}(x,t) = \mathbf{f}(x - \nu t) + \mathbf{g}(x + \nu t) \quad (2.20)$$

In higher dimensions, this factorization is not possible and solution cannot be constructed easily. Counterpart of vector wave equation in frequency domain is referred to as *Helmholtz equation* and given by

$$\nabla^2 \mathbf{E} + k^2 \mathbf{E} = 0 \quad (2.21)$$

where  $k = \omega^2 \varepsilon\mu = 2\pi/\lambda$  is called the propagation constant or wave number of medium.  $\lambda$  is the wavelength.

## CHAPTER 3

### COMPUTATIONAL ELECTROMAGNETICS

#### 3.1 Introduction

Maxwell's equations formulated circa 1873 define EM phenomena. Although it had been more than a century since its establishment, very few analytical solutions can be found for specific problems. Now engineers and researchers worldwide use numerical methods with computers to obtain solutions for the purpose of EM wave propagation, radiation, guiding and scattering. In this chapter we present first a brief history of computational electromagnetics (CEM), classification of EM problems and methods of solutions. Then we discuss basic features of time domain finite methods with specific emphasis to Finite Difference Time domain (FDTD) and Finite Volume Time Domain (FVTD). Finally characteristic based methods for Maxwell's equations are introduced. The strong connection between the characteristic based methods and the novel method proposed in this thesis will be clear in Chapters 4 and 5 on which the scope of thesis heavily relies.

#### 3.2 History of Computational Electromagnetics

Early development of CEM was prompted by intellectual curiosity on the implications of Maxwell's equations, especially after Hertz's verification of wireless propagation in the 1880s. They concentrated on analytical solutions of Maxwell's equations for diffraction problems via separation of variables, asymptotic evaluation of integrals etc. Diffraction theory evolved toward Geometrical Optics (GO) till the World War II. In the following years, the present Geometrical Theory of Diffraction (GTD) was formulated and elaborated. In the late 1940s Luneburg, Friedlander, Kline [1], [2], [3] devised a general high frequency (HF) theory of diffraction by showing that a field, associated with each point on a GO ray, has an asymptotic expansion in inverse powers of the wave number,  $k$  (or  $\omega$ ). In the 1950s, Keller [4] formulated GTD. This was based on generalization of Luneburg's asymptotic series to include fields of diffracted rays arising from vertices, corners etc. He extended Fermat's principle to derive laws governing these rays. Then, by considering canonical problems, researches were able to determine various diffraction coefficients [5], [6], [7]. This branch of the study of Maxwell's equations has been called HF (Asymptotic) Methods.

Almost parallel to Keller's work, methods based on integral equation (IE) formulation and reduction of equations to practically manageable matrix formulations, previously known in other branches of science, was introduced to EM community during and after 1950s. In the mid 1960s, Harrington set the agenda for the next 20 years by working out a systematic, functional space description of EM interactions which he called the Method of Moments (MoM) [8]. After Harrington's formulation, most of the work in CEM at low and moderate frequencies has concentrated on refining MoM and applying it to variety of problems, even in HF diffraction coefficients for GTD analysis.

HF Method studies in the years after Keller has concentrated on overcoming the defects of GTD to obtain a uniform representation of fields by employing asymptotic or numerical methods. Beyond the GO and Physical Optics (PO), variants of GTD such as Uniform Asymptotic Theory of Diffraction (UAT), Uniform Theory of Diffraction (UTD), Physical Theory of Diffraction (PTD), Incremental Theory of Diffraction (ITD), and Spectral Theory of Diffraction (STD) have been developed. After 1990s, time domain versions of these HF techniques have been reported in literature [9], [10], [11], [12], [13], [14]. They generally utilize either time-domain Green's functions or inverse Fourier transformation to obtain time domain solutions.

Two successful approaches of Keller and Harrington have well served the EM community for classes of problem that can be handled. However by the early 1980s, it became clear that rigorous engineering tools are needed for structures that could not be well treated by either method. For example, electrically large structures having complex shape and material composition were not easily modeled using GTD or its variants due to chaotic ray behavior. MoM suffered from computer limitations for large structures because of its dense, full matrix, matrix inversion and storage. To alleviate these drawbacks, iterative formulation of MoM was developed and then MoM was able to solve  $10\lambda$  sized-structures using available computers at that time. But iterative MoM suffered from convergence. And much effort has been devoted to developing alternative to these frequency domain methods such as conjugate gradient, spectral domain, domain decomposition etc.

In 1966, Yee introduced a computationally efficient means of directly solving Maxwell's time-dependent curl equations using finite differences in Cartesian coordinates which is later called FDTD [15]. With this approach, the continuous EM field in a finite volume of space is sampled at distinct points in space and time. Wave propagation, scattering, and penetration phenomena are modeled in a self-consistent manner by marching in time, that is,

repeatedly implementing the finite difference (FD) analog of curl equations in the grid. Time marching continues as the numerical wave analogs propagate in the grid to causally connect the physics of modeled region and stops when the desired late time or steady state response is observed at the field points of interest. Yee algorithm is 2<sup>nd</sup> order accurate in space and time with a leap-frog scheme. The sampling in space at sub- $\lambda$  resolution is selected to properly sample continuous field distribution in the Nyquist sense to avoid aliasing. 5 to 20 samples per wavelength of the highest frequency of interest can be set depending on the application. The sampling in time is selected to ensure stability of the numerical algorithm.

FDTD method in principle provided EM modeling with a level of detail as high as MoM. Unlike MoM, it does not lead to a system of linear equations defined over the entire problem space. Updating field components requires knowledge of only adjacent fields computed in previous time step, available in memory. Therefore overall computer storage and running time requirements of FDTD is linearly proportional to  $N$ , the number of field unknowns in the finite volume of space. In fact, the goal of iterative MoM in 1980s was this order of  $N$  on surface discretization. It is evident that it would be higher for volumetric MoM modeling.

Despite potential advantages of Yee's formulation, FDTD was very limited until the early 1980s because of a number of basic problems. First Yee's formulation provided no simulation of the field sampling space extending to infinity. This deficiency caused spurious, nonphysical reflection of the numerical wave analogs at the outer boundaries of computational domain. Second, it was not evident how to treat an incident wave having an arbitrary duration or arbitrary angle of incidence or angle of polarization. Third, it provided no means to obtain sinusoidal steady state magnitude and phase data from the computed transient field response. Fourth, it told nothing about wave interactions with important structures such as wires, and slots having dimension smaller than one lattice cell. Fifth, it provided no means to compute far field radiation or scattering patterns. And finally, it required volumetric space discretization and at that time computer resources was prohibitive. By the mid-1980s, the major difficulties with FDTD were overcome. Extensive publications during 1970s and early 1980s have put the FDTD modeling on credible foundations. In 1975 Taflov and Brodwin published the correct numerical stability criterion for Yee's algorithm and first grid-based time integration of a 2-D electromagnetic wave interaction problem for sinusoidal steady state [16] as well as the first 3-D grid-based computational model of electromagnetic wave absorption in complex, inhomogeneous biological tissues [17]. Mur published the first efficient successful finite difference implementation of absorbing

boundary conditions for Maxwell's equations [18]. During the last 20 years, FDTD EM modeling of biomedical problems, frequency dependent dielectric permittivity, microstrips, antennas, picosecond devices has been introduced [19], [20], [21], [22], [23], [24]. With advent of high speed, high capacity computers now FDTD is able to solve approximately  $100\lambda$  sized structures.

In the mid 1970s, finite element method for Helmholtz equation has been introduced. With this approach, the continuous EM field is approximated by a set of piecewise linear functions, each is defined over a specific triangular spatial element. Then Finite Element Time Domain (FETD) emerged for direct solution of Maxwell's curl equations during 1980s. Related works with FETD has been conducted by Mei, Madsen, Cangellaris and others [25]. Here a key consideration is optimizing the efficiency of mesh generation and coordinate storage because they have great impact on the overall computer resource requirement of finite element code.

Another PDE based direct solution method of Maxwell's equation, the Finite Volume Time Domain (FVTD) has been reported by Shankar et al., Madsen, Ziolkowski and Shang in 1990s [26], [27], [28]. it can be considered as a variant of FDTD and relies on characteristic theory of hyperbolic PDE. Conservation form of Maxwell's curl equations is used. FVTD collocates  $\mathbf{E}$  and  $\mathbf{H}$  fields at the cell centers while FDTD staggers them in space and time. FVTD will be discussed under characteristic based methods in Section 3.7 in some detail.

In the late 1960s, 1970s and early 1980s available computer technology permitted the implementation of HF Methods and MoM for practical engineering problems. These two approaches which essentially limit the modeling to the surface of the structure of interest, presented a good match between computer resource needs of CEM algorithm and existing machines at that time. Realization of enormously enhanced computer speeds and storage capacities by 1980s enabled the direct solution of Maxwell's PDEs and spurred new research activity in the area of FDTD, FETD, and FVTD within the entirety of structure of interest. Again there was a good match between the computer resources needed by CEM algorithms and the resources of existing machines.

Pace and range of applications of FDTD, FETD, FVTD and related space-grid TD methods for solution of Maxwell's equations are expanding rapidly. And they will continue to attract interest of researchers for emergent technologies since these can readily incorporate nonlinear and dispersive effects of materials and devices over large bandwidth. In particular

there is a strong trend toward proving the accuracy and usefulness of FDTD modeling of high speed optical and electronic devices [29].

The number of papers in this area presented at IEEE also proves the recent expanding level of interest to these time domain finite methods. For example in 1980s, related with FDTD, there were almost 10 publications on the average per year, but this number is around 1000 in recent years [29]. The reasons of interest can be summarized [30] as:

- They have been found to be remarkably robust, providing highly accurate modeling. They use samples of both  $\mathbf{E}$  and  $\mathbf{H}$ , not only one of them.
- They yield either sparse matrices (when structured as FETD) or no matrices at all (when structured as FDTD or FVTD)
- They present systematic approach to deal with complex material properties and inhomogeneities. Here, specifying a new structure/medium is reduced to a problem of mesh generation rather than more complicated problem of reformulating and solving the IE in MoM which may require difficult derivation of geometry and medium dependent Green's functions.

### 3.3 Classification of Electromagnetic Problems

EM problems are classified in terms of the equations describing them, boundary conditions and region of solution as in Table 3-1, [31].

Table 3-1: Classification of EM Problems

Type of Equation	Type of Boundary Condition	Type of Solution Region
<ul style="list-style-type: none"> <li>▪ Differential</li> <li>▪ Integral</li> <li>▪ Integro-Differential</li> </ul>	<ul style="list-style-type: none"> <li>▪ Dirichlet</li> <li>▪ Neumann</li> <li>▪ Mixed</li> </ul>	<ul style="list-style-type: none"> <li>▪ Interior/Closed</li> <li>▪ Exterior/Open</li> </ul>

Exterior problems have generally open conducting bodies (electric/magnetic) and have apertures, cavities which make EM wave interaction complex while in interior ones, details of body's composition such as material loss, inhomogeneities, anisotropy assume key role.

### 3.4 Classification of Methods of Solutions of Maxwell's Equations

A number of methods exist for the solution of Maxwell's equations [32]. We may classify them with respect to some criteria. First, they may be classified whether the method is analytical or numerical. Commonly used analytical and numerical methods are listed below.

Table 3-2: Commonly used analytical and numerical methods

<b>Analytical Methods</b>	<b>Numerical Methods</b>
<ul style="list-style-type: none"> <li>▪ Separation of Variables</li> <li>▪ Series Expansion</li> <li>▪ Conformal Mapping</li> <li>▪ Integral Solutions</li> <li>▪ Perturbation Method</li> </ul>	<ul style="list-style-type: none"> <li>▪ Variational Method</li> <li>▪ Methods of Moment</li> <li>▪ Finite Difference Method</li> <li>▪ Finite Element Method</li> <li>▪ Finite Volume Method</li> <li>▪ TLM Method</li> </ul>

Substantial work in analytical area was carried out until 1960s. And most EM problems were solved using the classical methods of separation of variables and IE solutions. By means of them, only a narrow range of practical problems could be investigated due to complex geometries and medium parameters defining the problem. For example, separation of variables method was useful only for a small class of simple structures such as spheres, circular cylinders etc. By 1960s, emerging computer technology made numerical methods feasible. Since then considerable effort has been expended on solving practical, complex EM problems for which closed form analytical solutions are either intractable or do not exist.

Secondly, methods of solutions may also be categorized according to their ability to provide specific time domain or frequency domain data as in Table 3-3.

Table 3-3: Time domain and frequency domain methods

<b>Time Domain Methods</b>	<b>Frequency Domain Methods</b>
<ul style="list-style-type: none"> <li>▪ Separation of Variables</li> <li>▪ FDTD</li> <li>▪ FETD</li> <li>▪ FVTD</li> <li>▪ TLM</li> <li>▪ MoM</li> </ul>	<ul style="list-style-type: none"> <li>▪ Separation of Variables</li> <li>▪ Variational Method</li> <li>▪ MoM</li> <li>▪ FDFD</li> <li>▪ FEFD</li> <li>▪ TLM</li> <li>▪ HF/Asymptotic Methods</li> </ul>

Note that in Table 3-3, some methods lie under both categories. Direct TD methods have been used to model both sinusoidal and pulse excitation. Equivalent FD data is obtained either by marching the solution to sinusoidal steady state or by performing a Fourier transform of the response. Direct FD methods employ time harmonic excitation ( $e^{j\omega t}$ ). Equivalent TD data is obtained by computing the magnitude/phase of a complete spectrum and then using inverse Fourier transform and convolution technique for a pulse excitation.

TD methods rely on IE (TDIE) or DE (TDDE) formulation. TDIE uses retarded potential integral approach and has the advantage that computational space is usually limited to structure surface. However, back-storage in time is required to perform retarded integrals. TDDE is adapted for example in FDTD and FETD. FD or FE analog of curl equations is marched in time in space grid consistently. A numerical wave radiation condition is employed to truncate computational domain. No-back storage is required for time marching.

Similar to TD methods, FD methods also rely on IE formulation (FDIE) or DE formulation FDDE or both. The broad category of FDIE methods treats the EM phenomena as a boundary value problem and then deriving and solving integral or integro-differential equation for unknown fields at the surface of scatterer. But these equations are not general and have to be rederived based on the geometry and material characteristics. As stated earlier, the most widely used approach has been MoM augmented with iterative technique based on preconditioned conjugate gradient methods. HF Methods fall into this category. For electrically large objects, they can yield much information about the far field scattering response, especially for conducting structures. Ray-tracing based on GTD, or its variants has been applied for scattering, radiation properties of aircraft, antennas etc. Today TLM, finite element (FEFD) and finite difference (FDFD) in frequency domain are also commonly used.

Combinations of above methods, called Hybrid Methods, are also possible. For example, various hybrid approaches involving MoM and HF methods have been explored to permit a self consistent composition of scattering effects of large as well as small features and conducting as well as dielectric material composition. Additional work has been done in attempting to apply HF methods to multi-ray regions using either hybrid ray/modal approaches or pure ray tracing within the cavities. Taflove and Umashankar [33] reported a hybrid MoM/FDTD method. Yee [34] proposed a hybrid FVTD/FDTD method utilizing classic leap-frog time marching. Another hybrid FDTD/Ray tracing method for indoor propagation has also been reported by Wang et al. recently [35].

Table 3-4: Some Hybrid Methods

<b>Hybrid Methods</b>
<ul style="list-style-type: none"> <li>▪ MoM/HF Method</li> <li>▪ FDTD/MoM</li> <li>▪ FDTD/HF Method</li> <li>▪ FVTD/FDTD</li> </ul>

### 3.5 Capabilities of Methods of Solution

In applying any of the above methods to an EM problem, one has to check the suitability of the method because each method has its own advantages and disadvantages. Following tables represent an assessment of capabilities of some methods with respect to range of structure size, geometric features and material composition by the mid 1990s, [31]. Extensive research is still underway to improve them.

Table 3-5: Modeling Approaches vs. Range of Structure Size (in  $\lambda$ )

	$< \lambda/10$	$\lambda$	$10\lambda$	$100\lambda$	$> 100\lambda$
HF Methods	NA	NA	✓	✓	✓
MoM/iterative	✓	✓	✓	?	NA
FDTD or FETD	?	✓	✓	✓	?

Table 3-6: Modeling Approaches vs. Geometric Features

	close spherical	with edges	with corners	with corner reflectors	with arbitrary unloaded cavities	with arbitrary loaded cavities
HF Methods	✓	✓	✓	?	NA	NA
MoM/iterative	✓	✓	✓	✓	?	?
FDTD or FETD	✓	✓	✓	✓	✓	✓

Table 3-7: Modeling Approaches vs. Material Composition

	PEC	PMC	Homo. dielectric	Inhomo. dielectric	Lossy media	Anisotropic media	
						Diag.	Gen.
HF Methods	✓	✓	?	NA	NA	NA	NA
MoM/iterative	✓	✓	✓	✓	?	?	NA
FDTD-FETD	✓	✓	✓	✓	✓	✓	?

✓ : Applicable    NA: Not Applicable    ? : Not sure if applicable

### 3.6 Features of Time Domain Finite Methods

We will discuss basic features of time domain finite methods such as grid structure (discretization), numerical dispersion and numerical stability based on [29], [30], [36]

#### 3.6.1 Grid Structure

Time domain finite methods were originally formulated in orthogonal coordinate systems dictating *orthogonal gridding*. For example Yee algorithm (FDTD) was formulated in

Cartesian coordinates and numerical computations are performed on these grids. Smoothly varying surfaces has been modeled by staircasing. This led to significant errors in certain problems which were analyzed rigorously by Cangellaris and Holland [37], [38]. If the nature of the problem can be described in an orthogonal coordinate system other than Cartesian, it is rather simple to redevelop the formulation as was done by Merewether and Holland [39], [40]. Alternatively, a grid with varying spatial increments along different coordinate directions can be used (irregular mesh). Especially finer grids are useful in areas of rapid field fluctuations. Kunz and Lee [41] used this approach to calculate the external response of an aircraft to an electromagnetic pulse.

Another gridding method is *subgridding*. In that, subdomains are gridded more finely than the rest of the problem space. Yee, Kasher, Kim, Hoefer and Zivanovic [42], [43], [44], [45] put forward this method. Here the key issue is the coupling of the fine and coarse grids.

In 1980s, Holland, Simpson [46] and Holland, Gilbert [47] presented the implementation and analysis of FDTD thin-strut formalism and FDTD thin-slot formulation (TSF). They permitted the modeling of arbitrarily thin wires and narrow slots. Also Umashankar et al and Taflove et al derived field update equations for wires, slots, joints [48], [49]. These equations were obtained from the integral form of Faraday's law. This method of gridding is called *subcellular gridding*.

Maybe the most important method is *conformal gridding*. In 1983, Holland [50] published the first FDTD algorithm for generalized nonorthogonal coordinates based on the work of Stratton [51]. In this approach, fields are expressed in terms of covariant components (flow along coordinate direction) and contravariant components (flow through a constant coordinate surface). In orthogonal coordinates, covariant and contravariant components are collinear, however in nonorthogonal coordinates, they are not collinear and auxiliary equations must be obtained to express covariant components in terms of contravariant components or vice-versa. Holland's formulation has been revisited by Fusco [52], [53]. Lee [54] generalized this approach assuming local curvilinear system for each cell face. Celuch-Marcysak and Gwarek [55] also introduced a generalized TLM algorithm that permits curved boundaries. In order to take advantage of standard Cartesian grid and the benefit of conformal approach, Yee et al [56] developed an overlapping grid method for FDTD that uses conformal grid near the material and Cartesian grid elsewhere. Jurgens and Taflove [57] extended the method used previously for subcellular structures for PEC and dielectric curved surfaces. This so called Contour-Path (CP-FDTD) method used Cartesian grids

except the vicinity of boundary where a distorted grid is used to conform. Mittra and Dey [58] also reported another conformal modeling for PEC surfaces. Madsen [59] extended original Yee's approach to unstructured grids using discrete surface integral (DSI). Similar methods have been used by Gedney and Lansing [60] and referred to as Generalized Yee (GY) algorithm. FVTD also lies within the class of conformal gridding. It was originally for irregular, nonorthogonal structured grids, then generalized to unstructured grids [61].

Navaro et al. [62] and Ray [63] studied the fundamental aspects of numerical algorithms for conformal grids (nonorthogonal) such as *stability*, *numerical dispersion* and *divergence free nature* of Maxwell's equations in source free region. While the usefulness of nonorthogonal curvilinear FDTD, DSI/GY reduces the boundary discretization error, additional dispersive errors can be introduced due to irregularity of grids. In general, above conformal methods are posed as a coupled set of difference equations (DE), and standard stability condition may not be sufficient to ensure strict stability of coupled DEs. The formulation must be *well posed*. Otherwise, numerical algorithm can be unconditionally unstable.

### 3.6.2 Numerical Dispersion

In this section, we will introduce the concept of *numerical dispersion* inherent to FDTD by working on 1-D scalar wave equation. But formulas and comments will also be provided for higher dimensional vector wave equations. 1-D scalar wave equation is rewritten as:

$$\frac{\partial^2 u}{\partial x^2} = \frac{1}{c^2} \frac{\partial^2 u}{\partial t^2} \quad (3.1)$$

where  $u(x,t)$  is a scalar function and exact solution of PDE. Second derivatives may be approximated with 2<sup>nd</sup> order accurate central finite differences by using Taylor series expansion at point  $(x,t) = (i\Delta x, n\Delta t)$  as:

$$\begin{aligned} \left. \frac{\partial^2 u}{\partial x^2} \right|_{i,n} &= \frac{u(x + \Delta x, t) - 2u(x, t) + u(x - \Delta x, t)}{(\Delta x)^2} + O[(\Delta x)^2] \\ \left. \frac{\partial^2 u}{\partial t^2} \right|_{i,n} &= \frac{u(x, t + \Delta t) - 2u(x, t) + u(x, t - \Delta t)}{(\Delta t)^2} + O[(\Delta t)^2] \end{aligned} \quad (3.2)$$

Truncating the higher terms in the expansion, then 1-D scalar wave equation can be approximated by a difference equation of

$$U_i^n = (c\Delta t)^2 \frac{U_{i+1}^n - 2U_i^n + U_{i-1}^n}{(\Delta x)^2} + 2U_i^n - U_i^{n-1} \quad (3.3)$$

$U_i^n$  stands for exact solution of DE (numerical solution of PDE). To proceeding, let us consider the continuous sinusoidal traveling wave solution of Eqn(3.1) in phasor form as:

$$u(x,t) = e^{j(\omega t - kx)} \quad (3.4)$$

where  $k = \pm \omega/c$ . Then phase velocity and group velocity are found as

$$v = \omega/k = \pm c, \quad v_g = d\omega/dk = \pm c \quad (3.5)$$

Now consider sinusoidal numerical wave analog evaluated by difference equation.

$$U_i^n = e^{j(\omega n \Delta t - k i \Delta x)} \quad (3.6)$$

where  $k^*$  is numerical wave number in the grid. In general  $k^*$  differs from  $k$  of physical wave. This difference gives rise to numerical phase and group velocities that depart from actual values. This in turn causes numerical errors called numerical dispersion or anisotropy effect. Substituting numerical wave analog into DE yields the following dispersion relation which will be investigated next.

$$\cos(\omega \Delta t) = \left( \frac{c \Delta t}{\Delta x} \right)^2 [\cos(k^* \Delta x) - 1] + 1 \quad (3.7)$$

**Case 1:** Very fine mesh ( $\Delta t \rightarrow 0, \Delta x \rightarrow 0$ )

Applying one-term approximation to cosines for small arguments, we obtain

$$k^* = \pm \omega/c \Rightarrow v^* = \pm c, \quad v_g^* = \pm c \quad (3.8)$$

We see that  $k^*$  has exactly the same relation to  $\omega$  with  $k$  and phase and group velocities are equal to  $c$  regardless of  $\omega$  implying that numerical solution is dispersionless. This is *intuitive* result because in the limit as the space, time increments of DE go to zero, we expect the numerical solution to be exact.

**Case 2:** Magic time step ( $c \Delta t = \Delta x$ )

Substituting magic time relation into numerical dispersion relation yields

$$\cos(\omega \Delta t) = \cos(k^* \Delta x) \quad (3.9)$$

This implies that

$$k^* = \pm \omega \Delta t / \Delta x = \pm \omega/c \Rightarrow v^* = \omega/k^* = \pm c, \quad v_g^* = d\omega/dk^* = \pm c \quad (3.10)$$

Numerical dispersion relation again reduces to that of exact solution. However, unlike case 1, this is *nonintuitive* because it implies that numerical solution is exact regardless of the choice of space and time increments. No matters fine or coarse mesh. This is interesting.

**Case 3:** Dispersive wave propagation

General solution of dispersion relation Eqn(3.7), where numerical dispersion errors can exist, is found by manipulating Eqn(3.7) as:

$$k^* = \frac{1}{\Delta x} \cos^{-1} \left( 1 + \left( \frac{\Delta x}{c\Delta t} \right)^2 [\cos(\omega\Delta t) - 1] \right) \quad (3.11)$$

For example, consider a choice of space and time increments such that  $c\Delta t = \Delta x/2$  and  $\Delta x = \lambda_0/10$  where  $\lambda_0$  is the free-space wavelength of physical wave. Further noting that  $k = 2\pi/\lambda_0$  and with this choice of  $\Delta x$ , numerical wave number is found to be  $k^* = 0.6364/\Delta x$ . This leads to numerical phase velocity of  $v^* = 0.9873c$ . The numerical phase velocity is seen to be 1.27% less than free-space phase velocity,  $c$ . That means that if a physical wave propagates over a distance of  $100\Delta x$  space cells ( $10\lambda_0$ ), numerical wave would propagate  $98.73\Delta x$  distances. And there would be  $45.72^\circ$  phase errors at the leading edge of wave. If the  $\Delta x$  were chosen to be  $\lambda_0/20$ , then phase error would reduce to  $11.19^\circ$ . This is a reduction by a factor of about 4:1. Then one can conclude that numerical dispersion can be reduced by choosing finer mesh, but running time and storage requirements are influenced adversely. Phase errors due to numerical dispersion are cumulative. FDTD is inherently dispersive and has this basic limitation for modeling electrically large structures. The dispersion relation for Yee algorithm for 2-D and 3-D are given in a similar fashion as:

$$\left( \frac{1}{v\Delta t} \sin \left( \frac{\omega\Delta t}{2} \right) \right)^2 = \left( \frac{1}{\Delta x} \sin \left( \frac{k_x^* \Delta x}{2} \right) \right)^2 + \left( \frac{1}{\Delta y} \sin \left( \frac{k_y^* \Delta y}{2} \right) \right)^2 \quad (3.12)$$

$$\left( \frac{1}{v\Delta t} \sin \left( \frac{\omega\Delta t}{2} \right) \right)^2 = \left( \frac{1}{\Delta x} \sin \left( \frac{k_x^* \Delta x}{2} \right) \right)^2 + \left( \frac{1}{\Delta y} \sin \left( \frac{k_y^* \Delta y}{2} \right) \right)^2 + \left( \frac{1}{\Delta z} \sin \left( \frac{k_z^* \Delta z}{2} \right) \right)^2 \quad (3.13)$$

As seen from Eqns(3.12),(3.13), grid discretization ( $\Delta x, \Delta y, \Delta z$ ), frequency  $\omega$  and direction of propagation ( $\mathbf{k}^* = k_x^* \hat{\mathbf{x}} + k_y^* \hat{\mathbf{y}} + k_z^* \hat{\mathbf{z}}$ ) have effect on the numerical dispersion.  $\Delta t$  is chosen in accordance with stability condition. If we fix the grid discretization and frequency, we observe that finite difference grids exhibit different phase velocity errors for different direction of propagation, with minimum at diagonal propagation in the grid. For example if ( $\Delta x, \Delta y, \Delta z$ ) all are set equal (let  $\Delta$ ), then the choice of  $\Delta t = \Delta/c\sqrt{2}$  in 2-D or  $\Delta t = \Delta/c\sqrt{3}$  in 3-D produces minimum phase error for diagonal propagating wave. But this is not of practical importance for general set of wave directions. Also note that  $\Delta t$  for diagonal propagation is the limit set by stability condition (*magic time step*). If we fix the direction of propagation but vary cell sizes, finite difference grid exhibits a numerical LPF effect which is also inherent to FDTD. Phase velocity diminishes as the propagating wave is more coarsely resolved, eventually reaching a sharp cut-off frequency where the numerical phase velocity goes to zero and wave can no longer propagate in the grid. Thus pulses having finite

duration experience ringing and broadening of pulse since high frequencies propagate more slowly in the grid than the low frequencies. To keep this effect at minimum, principal spectral components must be resolved with at least 10 cells per wavelength.

Elimination and reduction of dispersion error of related time domain finite method is very active research area. In 1989, Fang [64] proposed higher order accurate methods, i.e., 2<sup>nd</sup> order accurate in time and 4<sup>th</sup> order accurate in space. Another higher order method has also been reported by Hadi and Picket-May [65]. Higher order methods reduce dispersion but degrade the stability. A new FDTD method for reducing numerical dispersion was proposed by Cole [66]. In this method, nonstandard finite difference operators are used to substantially reduce the numerical dispersion over that of the Yee algorithm at a single frequency. Another method called Pseudo-Spectral Time Domain (PSTD) was put forward by Liu [67]. PSTD has the appealing property that the numerical dispersion error is made arbitrarily small simply by reducing the CFL stability number. Also new techniques developed from the theory of wavelets applied to Maxwell's equations appear to be promising area. One such method is the Multi-Resolution Time Domain (MRTD) reported by Krumpholz and Katehi [68]. Wang and Teixeira [69] reported an angle optimized FDTD algorithm at preassigned frequencies.

### 3.6.3 Numerical Stability

In the previous section, we observed that space increments ( $\Delta x, \Delta y, \Delta z$ ) and time step  $\Delta t$  could affect the velocity of propagation of numerical wave in computational grid. Now another consideration enters into selection of time step  $\Delta t$ .  $\Delta t$  must be bounded in order to avoid numerical instability which is an undesirable feature of *explicit* numerical algorithms causing the computed result to increase spuriously without limit as time marching continues. For *explicit* algorithms spatially adjacent field and source samples do not interact within the same time step, hence unknowns can be solved algebraically, a matrix does not need to be solved. Explicit algorithms are easy to implement and but conditionally stable.

Stability analysis of a numerical algorithm is achieved in a classical way established in Mathematics several decades ago by Courant, Friedrich, and Lewy (CFL) and Von Neumann. This approach permits separate analysis of time and space derivative parts of wave equation. To do this, numerical wave modes (Fourier modes, Plane wave modes) are introduced into difference equations. Then numerical algorithm is decomposed into separate time and space eigenvalue problems. Temporal and spatial spectrums are obtained. To guarantee numerical stability for every mode propagating in the grid, the spatial spectrum

must be contained completely within the stable range of temporal spectrum. For 1-D scalar wave equation, this analysis result in

$$\Delta t \leq \Delta x/c \quad (3.14)$$

We see that  $\Delta t$  has an upper bound. If  $\Delta t$  is selected to be larger than this bound, it is certainty that numerical algorithm be unstable. Interestingly, the upper bound for stable operation of the numerical algorithm is the magic time step discussed earlier. CFL stability condition for Yee algorithm is given in 2-D and 3-D respectively as:

$$\Delta t \leq \frac{1}{v \sqrt{\frac{1}{(\Delta x)^2} + \frac{1}{(\Delta y)^2}}} \quad , \quad \Delta t \leq \frac{1}{v \sqrt{\frac{1}{(\Delta x)^2} + \frac{1}{(\Delta y)^2} + \frac{1}{(\Delta z)^2}}} \quad (3.15)$$

If space increments  $(\Delta x, \Delta y, \Delta z)$  all are set equal (let  $\Delta$ ), then the CFL stability condition reduces to  $\Delta t = \Delta/c \sqrt{2}$  in 2-D and  $\Delta t = \Delta/c \sqrt{3}$  in 3-D. Eqn(3.15) are valid for isotropic, homogeneous medium and for uniform, regular meshes, i.e. space increments are constant in computational grid. In inhomogeneous medium, no neat formulas are available. But to be on the safe side,  $v_{\max}$  of  $v$  in the medium and smallest space increments in the grid are selected for the determination of  $\Delta t$ .

One can relax, even remove the CFL stability condition and select  $\Delta t$  to be larger than upper bound of CFL condition by using *implicit* numerical algorithms. For *implicit* algorithms, interaction of unknowns within the same time step is allowed. The number of these interactions can be adjusted and limited so advancing solution from time step  $n$  to  $(n+1)$  requires the solution of a sparse rather than a full matrix. But the accuracy of implicit algorithms is inferior to that of explicit ones. Implicit methods maybe unconditionally stable. The primary time domain finite methods (FDTD, FETD, FVTD) used today are fully explicit, 2<sup>nd</sup> order accurate grid-based solvers employing highly vectorizable and concurrent schemes for time marching field components. Explicit nature of the solvers is maintained by either leap-frog or predictor-corrector time integration schemes.

Numerical stability of time domain finite methods over the entire problem, in fact depends upon more than the CFL condition. There is a generalized (absolute) stability requirement due to interactions of numerical algorithm with algorithms augmenting it such as:

- Boundary Conditions (ABCs)
- Variable, Non-Cartesian, unstructured meshes
- Lossy, dispersive, nonlinear and gain materials

Thus one has to deal with these issues to enforce, ensure absolute stability. By the way, it is proper to mention relations among *consistency*, *convergence* and *stability* of difference equations (numerical algorithm) approximating the PDE. According to Lax theorem [70], a numerical algorithm is said to be *convergent* if it is *consistent* and *stable*. To prove convergence is difficult task, hence people usually deal with consistency and stability which are easier to show. Consistency is related to truncation errors which result from truncated Taylor's series approximating derivatives. If truncation error goes to zero while space increments ( $\Delta x, \Delta y, \Delta z$ ) and time step  $\Delta t$  go zero so that

$$U_{i,k,j}^n \xrightarrow{\Delta x, \Delta y, \Delta z, \Delta t \rightarrow 0} u(i\Delta x, k\Delta y, j\Delta z, n\Delta t) \quad (3.16)$$

then numerical algorithm is said to be *consistent* with the PDE. In general most numerical algorithm is consistent, so to prove *stability* suffices to prove convergence.

### 3.6.4 Absorbing Boundary Conditions

In solving EM problems, many geometries of interest are defined in open regions where the spatial domain of computed field is unbounded in one or more coordinate directions. Obviously no computer can handle unlimited amount of data therefore computation domain must be limited in size in such a way that it must be large enough to enclose the structure of interest and a suitable boundary condition on the outer perimeter must be used to simulate its extension to infinity. In this process, the outer boundary condition must suppress spurious reflections of the outgoing numerical wave to an acceptable level, permitting the solution to remain valid in the interior for all time steps. These boundary conditions have been called either Radiation Boundary Conditions (RBCs) or Absorbing Boundary Conditions (ABCs). There are mainly two types of ABCs: differential operator type and material type.

Differential operators which are simple to implement represents one of the achievements of ABC theory in 1970s and 1980s. These operators constitute a class of ABCs based upon the expansion of outward propagating wave solutions of the wave equation in spherical, cylindrical, Cartesian coordinates. They systematically kill, annihilate an arbitrary outgoing wave, leaving a remainder representing the residual error of process. Bayliss and Turkel [71] presented the basic idea to construct a weighted sum of three partial derivatives of the field.

- spatial partial derivative in the direction of outgoing wave
- spatial partial derivative in the direction transverse to the outgoing wave
- time partial derivative.

A better approach than Bayliss-Turkel method is to define a local coordinate system at the outer boundary that follows the natural grid planes, rather than crossing them. This is the

Engquist-Majda method [72]. A PDE that permits wave propagation only in certain directions is called one-way equation. When applied at the outer boundary of an FDTD grid, one-way wave equation numerically absorbs impinging wave. Engquist and Majda derived a theory of one-way wave equations suitable for ABCs. Then in 1981, Mur [16] who adapted work of Engquist-Majda published the first numerically stable 2<sup>nd</sup> order accurate, successful finite difference scheme for ABC applied to Yee grid. In that paper Mur implemented the partial derivatives as numerical central differences expanded about an auxiliary grid point. Higdon [73], [74] and Liao et al. [75] improved these differential operator type ABCs and obtained generalized, higher order operators and extrapolations in mid 1980s.

Material based ABCs are realized by surrounding the computational domain with a lossy material that dampens the outgoing fields. Early material ABCs did not provide sufficient low level of boundary reflections because the characteristic impedance of the material boundary was matched to the impedance of free space only at normal incidence. But the use of material ABCs significantly advanced with the work of Berenger [76] who introduced the PML ABC. Then Katz et al. [77] extended Berenger PML to 3-D problems. Large amount of loss can be introduced with PML for all frequencies and for all angles of incidence without affecting the phase velocity. Berenger PML ABCs can be used to truncate 2-D, 3-D space grid with a very small local reflection coefficient with more than 40dB improvement relative to Mur ABC. This allows the possibility of achieving FDTD simulations having a wide dynamic range of 70dB or more which is very critical in some applications such as radar cross section (RCS) simulations. Computational requirements of PML ABC are expectedly higher than differential operator types.

### 3.7 Characteristic Based Methods for Solutions of Maxwell's Equations

#### 3.7.1 Method of Characteristic for Hyperbolic PDEs

Consider the 2<sup>nd</sup> order, linear PDE of

$$a \frac{\partial^2 u}{\partial x^2} + b \frac{\partial^2 u}{\partial x \partial t} + c \frac{\partial^2 u}{\partial t^2} + e = 0 \quad (3.17)$$

where  $u$  is dependent variable to be solved and  $a, b, c, e$  may be functions of independent variables  $(x, t)$ . Let us denote the first and second derivatives by

$$p = \frac{\partial u}{\partial x}, \quad q = \frac{\partial u}{\partial t}, \quad r = \frac{\partial^2 u}{\partial x^2}, \quad s = \frac{\partial^2 u}{\partial x \partial t}, \quad w = \frac{\partial^2 u}{\partial t^2} \quad (3.18)$$

Let  $\Gamma$  be boundary where ICs (upto the first derivatives) are defined and  $C$  be a curve in  $(x, t)$  on which  $u, p,$  and  $q$  satisfy Eqn(3.17) and  $r, s, w$  are derivable from them. Such a problem is called Cauchy problem and ICs on  $\Gamma$  as Cauchy data (

Figure 3-1).

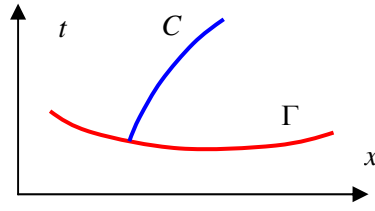


Figure 3-1: Cauchy problem and Method of Characteristic

Differentials of  $p, q$  in direction tangential to  $C$  satisfy the equations

$$\begin{aligned} dp &= \frac{\partial p}{\partial x} dx + \frac{\partial p}{\partial t} dt = r dx + s dt \\ dq &= \frac{\partial q}{\partial x} dx + \frac{\partial q}{\partial t} dt = s dx + w dt \end{aligned} \quad (3.19)$$

where  $ar+bs+cw+e = 0$  and  $dt/dx$  is the slope of the tangent to  $C$ . Eliminating  $r, w$  yields

$$s \left( a \left( \frac{dt}{dx} \right)^2 - b \left( \frac{dt}{dx} \right) + c \right) - \left( a \frac{dp}{dx} \frac{dt}{dx} + c \frac{dq}{dx} + e \frac{dt}{dx} \right) = 0 \quad (3.20)$$

Now choose  $C$  so that the slope of the tangent at every point on it is a root of the equation

$$a \left( \frac{dt}{dx} \right)^2 - b \left( \frac{dt}{dx} \right) + c = 0 \quad (3.21)$$

so that  $s$  is also eliminated in Eqn(3.20). Then it follows that in this direction

$$a \frac{dp}{dx} \frac{dt}{dx} + c \frac{dq}{dx} + e \frac{dt}{dx} = 0 \quad (3.22)$$

This shows that at every point  $(x, t)$  of solution domain there are two directions, given by the roots of Eqn(3.21), along which there is a relationship, given by Eqn(3.22), between the total differentials  $dp$  and  $dq$ . This relationship can be used to solve the original PDE by a series of step-by-step integration. If the PDE is hyperbolic these roots are real, distinct and gives us the characteristic curve directions ( $\alpha, \beta$  characteristics) as illustrated in Figure 3-2. ICs are propagated along  $\alpha, \beta$  characteristics and solution  $u(x, t)$  is formed numerically. This is called Method of Characteristics (MoC). In order to obtain the solution,  $\Gamma$  along which Cauchy data is defined must be a non-characteristic curve. When it is a characteristic curve, then PDE have no solution unless Cauchy data satisfy necessary, additional differential relationship on that characteristic.

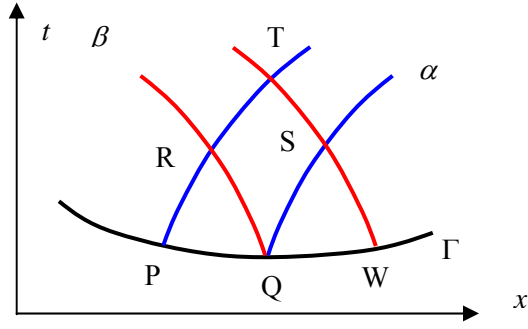


Figure 3-2: Characteristic curves

Scalar or vector hyperbolic PDEs (i.e., Maxwell's equations, wave equation) in  $(x,t)$ -space can be solved numerically by MoC. But as the number of independent variables and dependent variables increase, many characteristics generate from a point. Then the method can not be easily, efficiently implemented and has some limitations as will be discussed in the next section. Theoretically in higher dimensions, there exist characteristic surfaces and characteristic curves (bicharacteristics) of PDE. In 1-D, characteristic surfaces degenerate into characteristic curves, that is, characteristics and bicharacteristics are the same.

Elliptic and parabolic PDEs may have analytic solutions even when ICs/BCs are discontinuous. However, hyperbolic PDEs are not so. Discontinuities in the ICs are propagated into solution domain along bicharacteristics [70]. This interesting property will be utilized in Chapters 4 and 5 to establish the underlying theory of the novel method proposed in this thesis. In Figure 3-2, it is seen that solution at R is affected by ICs between P and Q then this region is called domain of dependence of R. Similarly Point Q affects the open region bounded by characteristics curves originating at Q. This open region is called domain of influence of Q. Hence as in the solution of scalar wave equation with finite differences, one must also pay attention to spatial and temporal increments to solve the PDE numerically by MoC. For example, let us consider again the solution of 1-D wave equation for  $t > 0$  with Cauchy data defined on  $x$ -axis. It is repeated here.

$$\frac{\partial^2 u}{\partial x^2} = \frac{\partial^2 u}{c^2 \partial t^2} \quad (3.23)$$

whose characteristic directions are  $dt/dx = \pm 1/c$ . Suppose that we have approximated Eqn(3.23) with the same difference equation of Eqn(3.3).

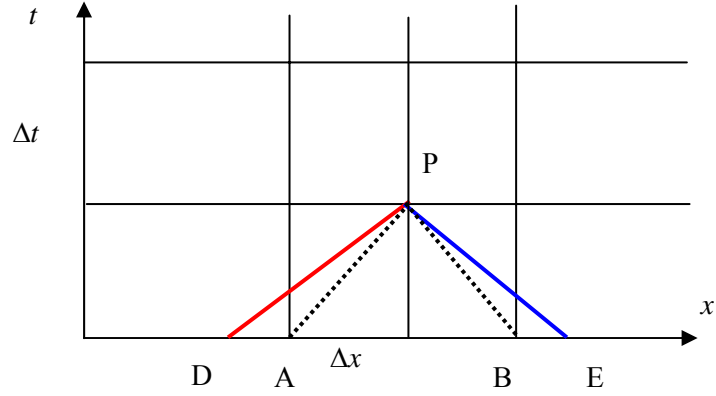


Figure 3-3: Domain of dependence and stability

Considering Figure 3-3, if the ICs along DE are altered, the solution at P by numerical algorithm will change. But these alterations will not affect the solution value of PDE at P due to ICs along DA and BE. Hence in this case an explicit numerical solution will not converge to analytic solution even as  $\Delta x, \Delta t$  go to zero and will not be stable. For convergence and stability, line DE (analytical domain of dependence) must be contained in line AB (numerical domain of dependence) implying that slope  $\Delta t \leq \Delta x/c$ . This is, in fact, the CFL condition.

Also recall that the solution of 1-D scalar wave equation at point P can be found by d'Alembert's solution.

$$u(x_p, t_p) = \frac{1}{2} \left( f(x_p + ct_p) + f(x_p - ct_p) + \frac{1}{c} \int_{x_p - ct_p}^{x_p + ct_p} g(\zeta) d\zeta \right) \quad (3.24)$$

where  $f, g$  are ICs. In 2-D, 3-D, finding the solution of wave equation with ICs

$$\nabla^2 u + \frac{1}{c^2} \frac{\partial^2 u}{\partial t^2} = 0, \quad u(\mathbf{R}', 0) = f(\mathbf{R}'), \quad \frac{\partial u(\mathbf{R}', 0)}{\partial t} = g(\mathbf{R}') \quad (3.25)$$

is provided by

$$u(\mathbf{R}, t) = \frac{1}{4\pi} \int_{S'} \left( \frac{f(\mathbf{R}')}{\lambda^2} + \frac{1}{\lambda} \frac{\partial f(\mathbf{R}')}{\partial \lambda} \right) d\mathbf{S}' + \frac{1}{4\pi c} \int_{S'} \frac{g(\mathbf{R}')}{\lambda} d\mathbf{S}' \quad (3.26)$$

which is called Method of Spherical Means in 3-D (Poincare's solution) and Method of Descent (Hadamard solution) in 2-D where  $\lambda = |\mathbf{R}' - \mathbf{R}| = ct$ . All these expressions rely on the domain of dependence concept [78].

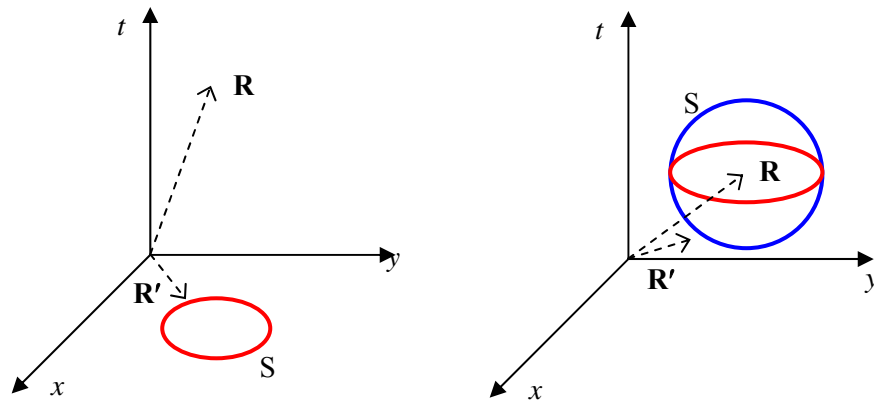


Figure 3-4: Method of Descent and Method of Spherical Means

In 2-D, domain of dependence is a circle and domain of influence is interior of a cone. In 3-D they become surface of sphere and forward light cone respectively.

### 3.7.2 Application to Maxwell's Equations

Characteristic based methods are well known in Computational Fluid Dynamics (CFD) and have been widely used in the solution of Euler and Navier-Stoke PDEs. But this approach has been introduced to EM community by the 1990s for the solution of time dependent Maxwell's equations although it has a long history of development and application in CFD. Considering the discussions of previous section, one can infer the following appealing properties of characteristic based methods for applications.

- A *well-posed* initial value problem is easily established meaning that
  - Solution exists and is unique
  - Solution is stable
  - Solution continuously depends on initial data
- They honor directional signal propagation along characteristic curves. This is a very important property enabling us access to eliminate the numerical dispersion because behavior of signal is expressed by ODEs rather than PDEs along characteristics.
- Due to directional propagation, ABCs can be implemented easily and almost perfectly at outer boundary of computational domain.
- Since they rely on physical domain of dependence and influence, they contribute to numerical stability and accuracy.
- Mathematically they best suit physical nature of wave phenomena.

Efforts to take advantage of proven methods of CFD have led to the formulation of a very comprehensive numerical approach for solving electromagnetic scattering, and radiation problems involving complex objects. FVTD is essentially a characteristic based method and is known as *dissipative* despite dispersive nature of FDTD [79]. This approach is based on Riemann integration method and recent advances in numerical solution of PDEs in CFD. It has been successfully applied to diverse range of problems, involving electrically large scatterers, inhomogeneous and layered dielectrics, cavities, frequency dependent materials, impedance surfaces, canonical antennas etc. It collocates  $\mathbf{E}$  and  $\mathbf{H}$  in both space and time rather than interleaving them. These are volume averages in the lattice. This has the advantage of reducing the complexity of gridding in material region and in extracting the near field data for transformation to far field. FVTD employs body fitted meshes to represent target geometry, hence fall into the conformal category. These properties reduce the limitations for storage and modeling of large bodies for RCS simulations. To apply characteristic based methods, Maxwell's curl equations are first recast into conservation form, for example in source-free, nonconducting, isotropic medium as:

$$\frac{\partial \mathbf{U}}{\partial t} + \mathbf{A} \frac{\partial \mathbf{F}_1}{\partial x} + \mathbf{B} \frac{\partial \mathbf{F}_2}{\partial y} + \mathbf{C} \frac{\partial \mathbf{F}_3}{\partial z} = 0 \quad (3.27)$$

$\mathbf{U}$  is the quantity to be conserved in the centroid of lattice and  $\mathbf{F}_1$ ,  $\mathbf{F}_2$  and  $\mathbf{F}_3$  are the fluxes at the lattice faces defined as:

$$\begin{aligned} \mathbf{U} &= [B_x \ B_y \ B_z \ D_x \ D_y \ D_z]^T, \quad \mathbf{F}_1 = [0 \ -E_z \ E_y \ 0 \ H_z \ -H_y]^T \\ \mathbf{F}_2 &= [E_z \ 0 \ -E_x \ -H_z \ 0 \ H_x]^T, \quad \mathbf{F}_3 = [-E_y \ E_x \ 0 \ H_y \ H_z \ 0]^T \end{aligned} \quad (3.28)$$

Under coordinate transformation for conformal grids, governing equations become

$$\frac{\partial \bar{\mathbf{U}}}{\partial t} + \frac{\partial \bar{\mathbf{F}}_1}{\partial \xi} + \frac{\partial \bar{\mathbf{F}}_2}{\partial \eta} + \frac{\partial \bar{\mathbf{F}}_3}{\partial \gamma} = 0 \quad (3.29)$$

$$\begin{aligned} \bar{\mathbf{F}}_1 &= \left( \frac{\partial \xi}{\partial x} \mathbf{F}_1 + \frac{\partial \xi}{\partial y} \mathbf{F}_2 + \frac{\partial \xi}{\partial z} \mathbf{F}_3 \right) V, \quad \bar{\mathbf{F}}_2 = \left( \frac{\partial \eta}{\partial x} \mathbf{F}_1 + \frac{\partial \eta}{\partial y} \mathbf{F}_2 + \frac{\partial \eta}{\partial z} \mathbf{F}_3 \right) V \\ \bar{\mathbf{F}}_3 &= \left( \frac{\partial \gamma}{\partial x} \mathbf{F}_1 + \frac{\partial \gamma}{\partial y} \mathbf{F}_2 + \frac{\partial \gamma}{\partial z} \mathbf{F}_3 \right) V, \quad \bar{\mathbf{U}} = \mathbf{U} V \end{aligned} \quad (3.30)$$

$V$  is the Jacobian of transformation (cell volume). In transformed system of equations, coefficient matrices can not be taken out of differential operator globally as in Eqn(3.27) If it were, decoupled equations would be obtained after diagonalization. Otherwise one treats the equations locally. Characteristic-based methods have basic limitation that coefficient matrices in Eqns(3.27),(3.29) can be diagonalised in 1-D at a time. Hence all 2-D, 3-D problems must be split into multiple 1-D sub-problems and solved by numerical sweeps.

Each 1-D subproblem is called Riemann problem for example the one in (Eqn(3.31)) with coefficient matrix  $\mathbf{A}$  given by Eqn(3.32).

$$\frac{\partial \bar{\mathbf{U}}}{\partial t} + \mathbf{A} \frac{\partial \bar{\mathbf{U}}}{\partial \xi} = 0 \quad (3.31)$$

$$\mathbf{A} = \frac{\partial \bar{\mathbf{F}}_1}{\partial \bar{\mathbf{U}}} = \begin{bmatrix} 0 & 0 & 0 & 0 & 0 & 0 \\ 0 & 0 & 0 & 0 & 0 & -1/\varepsilon \\ 0 & 0 & 0 & 0 & 1/\varepsilon & 0 \\ 0 & 0 & 0 & 0 & 0 & 0 \\ 0 & 0 & 0 & 1/\mu & 0 & 0 \\ 0 & 0 & -1/\mu & 0 & 0 & 0 \end{bmatrix} \quad (3.32)$$

From matrix  $\mathbf{A}$ , one can find the eigenvalues by  $\det(\mathbf{A}-\Lambda\mathbf{I}) = 0$ . They give us the speed and direction of propagation [80]. They are real and contain multiplicities.

$$\Lambda = (-1/\sqrt{\varepsilon\mu}, -1/\sqrt{\varepsilon\mu}, 1/\sqrt{\varepsilon\mu}, 1/\sqrt{\varepsilon\mu}, 0, 0) \quad (3.33)$$

Despite multiplicities, linearly independent eigenvectors can still be found and similarity matrices of diagonalization  $\mathbf{S}$ ,  $\mathbf{S}^{-1}$  are obtained from them. Then fluxes can be split into negative and positive components with respect to positive and negative eigenvalues or characteristic variables (Riemann invariants) can be defined which propagate along characteristics. In this spatial part of the Riemann problem, implementation of several finite difference and finite volume explicit/implicit (Lax-Wendroff, Crank-Nicholson, Alternating Direction Implicit (ADI)) numerical algorithms have been reported [81], [82], [83], [84], [85], [86], [87], [88]. Time integration part of conserved quantity is handled by predictor-corrector, leap-frog, or Runge-Kutta methods. Recently Beggs [90], [91] published first 1-D and then 2-D bicharacteristic FDTD methods. Novel method proposed in this thesis also relies on characteristic theory but as will be discussed in Chapters 4, and 5, it is totally different than above methods.

Courant, Friedrich and Lewy in their classical paper [89] demonstrated necessary and sufficient condition for convergence and stability of a numerical algorithm. Based on their work, it has been shown that 2-step Lax-Wendroff upwind algorithm [83] for the solution of Maxwell's equations is stable if and only if

$$|\Lambda|_{\max} \frac{\Delta t}{\Delta \xi} \leq 2 \quad (3.34)$$

where  $|\Lambda|_{\max}$  is the largest eigenvalue of matrix  $\mathbf{A}$  at any point in the grid. In higher dimensions, the value of  $|\Lambda|_{\max}$  is taken to be

$$|\Lambda|_{\max} = \mathbf{max}(|\Lambda_{\xi}| + |\Lambda_{\eta}| + |\Lambda_{\gamma}|) \quad (3.35)$$

## CHAPTER 4

### ELECTROMAGNETIC APPROACH TO GEOMETRICAL OPTICS

#### 4.1 Introduction

EM community uses plane waves to explain the governing laws and tools of GO such as Fermat's principle, Snell's law of reflection and refraction, wave fronts and rays. Moreover the first term of HF asymptotic expansion (Luneburg-Kline series) of an EM field, say for  $\mathbf{E}$ ,

$$\mathbf{E}(\mathbf{R}_0, \omega) = e^{-jk\Psi(\mathbf{R}_0)} \sum_{m=0}^{\infty} \frac{\mathbf{E}_m(\mathbf{R}_0)}{(j\omega)^m} \quad (4.1)$$

is called GO field of EM field and obeys laws of GO. This asymptotic series is accurate as  $k$  (or  $\omega$ ) goes to infinity. Higher order terms ( $m > 0$ ) are understood as improvements over GO field. In this chapter we present a different approach for GO on the basis of EM foundation laid in Chapter 2. When a source begins to act, EM fields  $\mathbf{E}$ ,  $\mathbf{H}$  spread out into space. Due to finite velocity of propagation, there will be a domain of  $(x,y,z,t)$ -space in which the field vectors are not zero, and a domain in which the fields do not penetrate [80]. Separating these two domains is a *hypersurface*. The field vectors are discontinuous on this hypersurface. And GO fields are defined in terms of these *discontinuities*. This approach can be called as *Time Domain Geometrical Optics (TDGO)*.

For this purpose, we first present IE forms of Maxwell's equations. These IEs are not usual Amphere's and Faraday's laws of Chapter 2. Instead they involve integrals over hypersurfaces in  $(x,y,z,t)$ -space. The use of them is that they admit discontinuous solutions (weak) of Maxwell's equations where DEs have no meaning. Based on them, *discontinuity conditions* are derived and types of discontinuity hypersurfaces are discussed. *Transport equations* which govern the variation of GO fields are also studied. By means of them, we furnish the theory of TDGO. The scope of this chapter totally depends on the work of Kline [92]. Instead of CGS, we present all derivation and formulation in MKS here.

#### 4.2 Maxwell's Equations and Discontinuous Solutions

Time-dependent Maxwell's curl equations in isotropic, nonconducting medium are

$$\nabla \times \mathbf{E} = -\mu \frac{\partial \mathbf{H}}{\partial t}, \quad \nabla \times \mathbf{H} = \varepsilon \frac{\partial \mathbf{E}}{\partial t} + \mathbf{J}_f \quad (4.2)$$

An auxiliary function  $\mathbf{F}$  related with the behavior of source charges is defined as:

$$\mathbf{J}_f = \frac{\partial \mathbf{F}}{\partial t} \quad (4.3)$$

$\varepsilon$ ,  $\mu$  and  $\mathbf{F}$  are assumed to be smooth (continuous and differentiable). Discontinuities in  $\mathbf{F}$  is *finite* and  $\varepsilon$ ,  $\mu$  may have *finite* discontinuities at a boundary between two media. Source  $\mathbf{J}_f$  (or  $\mathbf{F}$ ) begins to act at  $t=0$  so that  $\mathbf{E}$ ,  $\mathbf{H}$  be zero for  $t < 0$  and nonzero for  $t \geq 0$  due to causality. We will consider solutions that exist in the  $(x,y,z,t > 0)$  half-space. Let  $\Omega(x,y,z,t)$  be class of real, scalar testing functions with continuous and continuous derivatives of all orders in  $(x,y,z,t)$ -space. Moreover each  $\Omega$  is to be zero on the boundary  $\Gamma$  and outside of a compact domain in the half-space. Then multiplying Eqn(4.2) with  $\Omega$  and integrating over  $(x,y,z,t)$ -space, it is found that

$$\begin{aligned} \int_{\Gamma} (\Omega \nabla \times \mathbf{H} - \Omega (\varepsilon \frac{\partial \mathbf{E}}{\partial t} + \frac{\partial \mathbf{F}}{\partial t})) dw &= 0 \\ \int_{\Gamma} (\Omega \nabla \times \mathbf{E} + \Omega (\mu \frac{\partial \mathbf{H}}{\partial t})) dw &= 0 \end{aligned} \quad (4.4)$$

where  $dw = dx dy dz dt$  is a volume element of  $\Gamma$ . Taking above integrals using integration by parts, it can be shown that Eqns(4.4) is equivalent to

$$\begin{aligned} \int_{\Gamma} (\nabla \Omega \times \mathbf{H} - \frac{\partial \Omega}{\partial t} (\varepsilon \mathbf{E} + \mathbf{F})) dw &= 0 \\ \int_{\Gamma} (\nabla \Omega \times \mathbf{E} + \frac{\partial \Omega}{\partial t} (\mu \mathbf{H})) dw &= 0 \end{aligned} \quad (4.5)$$

Then differential forms of Maxwell's equations Eqn(4.2) and IEs Eqn(4.5) are equivalent in the sense that they have the same solutions. We will deal with discontinuous  $\mathbf{E}$ ,  $\mathbf{H}$  solutions of Maxwell's equations, and above IEs fit to the purpose.

### 4.3 Discontinuity Conditions

The objective in this section is to derive conditions that the discontinuities in  $\mathbf{E}$ ,  $\mathbf{H}$  must satisfy on any discontinuity hypersurface. Let  $G$  be a subdomain of  $\Gamma$  and a discontinuity hypersurface  $\phi = 0$  passes through it as in Figure 4-1. Then the solutions  $\mathbf{E}$ ,  $\mathbf{H}$  of Eqn(4.5) must satisfy the same IEs taken over the subdomain  $G$ . The hypersurface  $\phi = 0$  divides  $G$  into two domains  $G_1$  and  $G_2$ .  $\mathbf{E}$ ,  $\mathbf{H}$  is assumed to be analytic in these subdomains and discontinuities in themselves have *finite limits* as  $\phi = 0$  is approached through  $G_1$  or through  $G_2$ . These facts are assured by the existence theorem of Lewis [93].

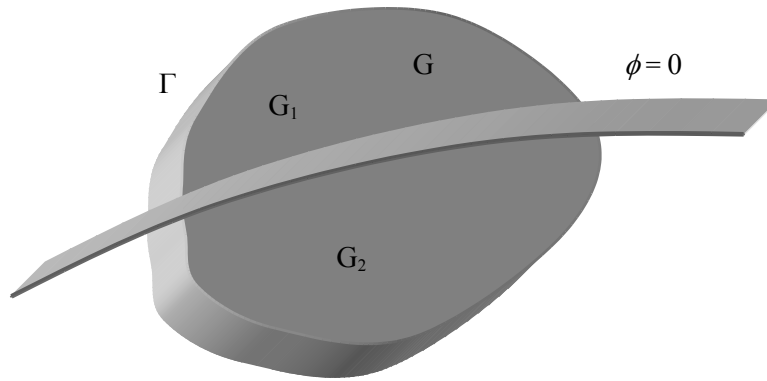


Figure 4-1: Discontinuity hypersurface crossing  $\Gamma$

Then discontinuity conditions are found as:

$$\begin{aligned} \nabla \phi \times [\mathbf{E}] + \frac{\partial \phi}{\partial t} [\mu \mathbf{H}] &= 0 \\ \nabla \phi \times [\mathbf{H}] - \frac{\partial \phi}{\partial t} [\epsilon \mathbf{E} + \mathbf{F}] &= 0 \end{aligned} \quad (4.6)$$

where  $[\mathbf{E}] = \mathbf{E}_1 - \mathbf{E}_2$ . These conditions must hold on any hypersurface  $\phi = 0$ . In fact Eqn(4.6) is counter part of Maxwell's curl equations. Since field vectors are discontinuous on  $\phi = 0$ , the values of the field vectors are denoted such that  $\mathbf{E}_1$  is the value of  $\mathbf{E}(x,y,z,t)$  on  $\phi = 0$  when  $(x,y,z,t)$  is approached through  $G_1$  and  $\mathbf{E}_2$  the corresponding value at  $(x,y,z,t)$  for an approach through  $G_2$ . These values  $\mathbf{E}_1$  and  $\mathbf{E}_2$  will in general be *finite limits* of continuous values of  $\mathbf{E}$  in  $G_1$  and  $G_2$  respectively. For example, hypothetically consider the following time waveform for  $\mathbf{E}$  and its derivative (Figure 4-2).

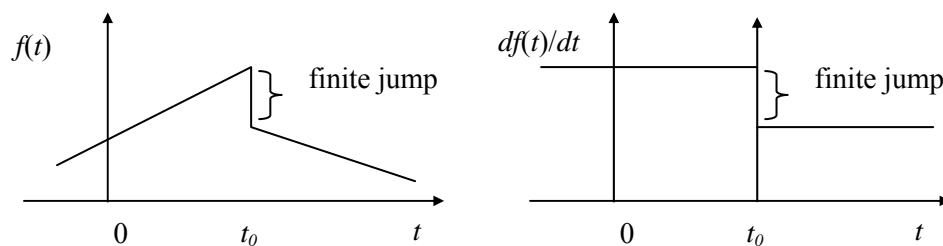


Figure 4-2: Interpretation of finite jump discontinuities

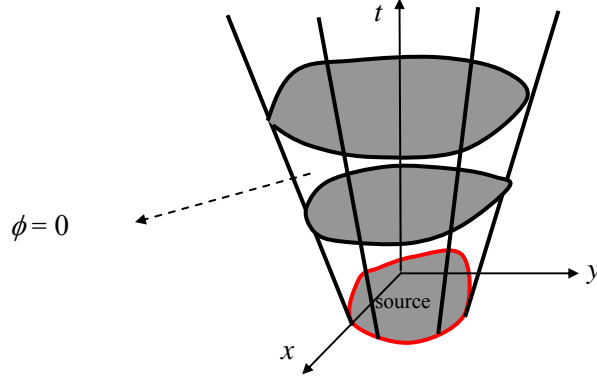


Figure 4-3: A hypercone in  $(x,y,t)$ -space

#### 4.4 Types of Discontinuity Hypersurfaces

There are mainly three types of discontinuity hypersurfaces represented by geometrical equation  $\phi(x,y,z,t) = 0$ . In order to help us in our thinking about them, consider the related situation in  $(x,y,t)$ -space as in Figure 4-3. First kind of hypersurface is the hyperplane  $t = 0$ . If the spatial distribution of sources is some bounded domain of this hyperplane, field vectors will be nonzero there for  $t \geq 0$  but zero for  $t < 0$  since sources are turned on at  $t = 0$ . Hence this hyperplane  $t = 0$  is a discontinuity hypersurface and can be represented as:

$$\phi(x,y,z,t) \equiv t = 0 \quad (4.7)$$

Then  $\nabla\phi = 0$ ,  $\partial\phi/\partial t = 1$  and discontinuity conditions on this hypersurface become

$$[\varepsilon \mathbf{E} + \mathbf{F}] = 0, \quad [\mu \mathbf{H}] = 0 \quad (4.8)$$

Since  $\mathbf{E}$ ,  $\mathbf{H}$  are 0 for  $t < 0$  then we have

$$\mathbf{E}(x,y,z,0^+) = -\frac{1}{\varepsilon} \mathbf{F}(x,y,z,0^+), \quad \mathbf{H}(x,y,z,0^+) = 0 \quad (4.9)$$

Eqn(4.9) shows that ICs for Maxwell's equations can be obtained from the source condition  $\mathbf{F}$ . Moreover if a source continues to act after  $t = 0$ , the ICs do alone suffice to determine the solution of Maxwell's equations in pure initial value problem.

Second and maybe the most familiar type of hypersurface on which field vectors are discontinuous is a stationary boundary between two media such as

$$\phi(x,y,z,t) \equiv \Psi_0(x,y,z) = 0 \quad (4.10)$$

This is a surface in  $(x,y,z)$ -space and a cylindrical hypersurface whose elements are parallel to  $t$ -axis in  $(x,y,z,t)$ -space. In this case  $\partial\phi/\partial t = 0$  and  $\nabla\phi = \nabla\Psi_0$ , then discontinuity conditions in source-free region become

$$\nabla\Psi_0 \times \mathbf{E} = 0, \quad \nabla\Psi_0 \times \mathbf{H} = 0 \quad (4.11)$$

The vector  $\nabla\Psi_0$  is normal to the surface  $\Psi_0=0$ . These equations state that tangential components of  $\mathbf{E}$ ,  $\mathbf{H}$  and normal components of  $\mathbf{D}$ ,  $\mathbf{B}$  are continuous across any surface fixed in  $(x,y,z)$ -space. This statement contains the familiar boundary conditions of Chapter 2.

Thirdly, the field created by source will spread out into  $(x,y,z,t)$ -space. Since the fields move through space with a finite velocity, they will reach any point  $(x,y,z,t)$  only after some time  $t_0$ . Hence there is a region of  $(x,y,z,t)$ -space in which the fields are nonzero and outside of this, a region in which the fields are zero. Separating these two regions is also a discontinuity hypersurface. Inside the cone (Figure 4-3) fields are nonzero and outside they are zero. At any point on the cone and above  $t = 0$  plane, source  $\mathbf{F} = 0$ . And since we assume smooth media in this region, then discontinuity conditions for this case become

$$\begin{aligned}\nabla\phi\times[\mathbf{E}]+\frac{\partial\phi}{\partial t}\mu[\mathbf{H}]&=0 \\ \nabla\phi\times[\mathbf{H}]-\frac{\partial\phi}{\partial t}\varepsilon[\mathbf{E}]&=0\end{aligned}\quad (4.12)$$

These two vector equations form a *homogeneous* system of six scalar equations in the components of  $[\mathbf{E}]$  and  $[\mathbf{H}]$ . Solving for  $\mathbf{H}$ , one can obtain

$$(\nabla\phi)^2[\mathbf{H}]-\varepsilon\mu\left(\frac{\partial\phi}{\partial t}\right)^2[\mathbf{H}]=0\quad (4.13)$$

For nonzero solutions, determinant of coefficient matrix of Eqn(4.13) must be zero on  $\phi=0$ .

$$(\nabla\phi)^2-\varepsilon\mu\left(\frac{\partial\phi}{\partial t}\right)^2=0\quad (4.14)$$

This equation is known in the theory of PDEs as the characteristic condition for the characteristics of Maxwell's equations, and the solutions  $\phi=0$  are the characteristics. Note that this equation is not a true PDE because it holds only on  $\phi=0$  where  $x,y,z$ , and  $t$  are not independent. These  $\phi$ s, characteristics (hypersurfaces), consist of several branches such as:

$$\phi(x,y,z,t)\equiv\Psi(x,y,z)-ct=0\quad (4.15)$$

If Eqn(4.15) is substituted into Eqn(4.14), one can obtain a true PDE for  $\Psi(x,y,z)$ .

$$|\nabla\Psi|^2=\varepsilon\mu c^2=\varepsilon_r\mu_r=n^2\quad (4.16)$$

This is the *Eiconal equation* of GO and its solutions are the wave fronts  $\Psi(x,y,z)$ . Note that conductivity  $\sigma$  of the medium does not appear, this is not because our assumption of nonconducting medium. The shape of the wave fronts is influenced only by  $\varepsilon$ ,  $\mu$  even in metals.

## 4.5 Geometrical Optics

### 4.5.1 Definition of Geometrical Optics

As we pointed out earlier, the field vectors  $\mathbf{E}$ ,  $\mathbf{H}$  are discontinuous on  $\phi = 0$ . And we define them as GO fields. In other words, GO field is a special set of values of full time dependent field, namely discontinuities of  $\mathbf{E}$ ,  $\mathbf{H}$ .

### 4.5.2 Wave Fronts and Rays

The location of GO field can also be visualized in  $(x,y,z)$ -space in Figure 4-4. We are interested in the values of  $\mathbf{E}$ ,  $\mathbf{H}$  on  $\phi(x,y,z,t) = 0$ . If we cut the hypersurface  $\phi = 0$  by any hyperplane in the form of  $t = t_0$ , we get a surface and we may project it parallel to  $t$ -axis onto  $(x,y,z)$ -space. Then as  $t_0$  varies we get a family of surfaces. Each of these surfaces is the boundary of the 3-D spatial region reached by the field at the corresponding time  $t_0$ . These surfaces are wave fronts of GO. They are one-parameter family of wave fronts and can explicitly be written for  $t$  as discussed in the previous section.

$$\Psi(x,y,z) = ct \quad (4.17)$$

Study of GO fields can be performed in terms of field vectors on the wave fronts. We will concentrate on the values of field vectors on wave fronts as they propagate into  $(x,y,z)$ -space as  $t$  increases. These values are GO field so they must obey the laws of GO. We shall find later that the behavior of the GO fields can be studied independently of the values inside the hypersurface  $\phi = 0$  (local phenomena nature of GO). The values of  $\mathbf{E}(x,y,z,t)$ ,  $\mathbf{H}(x,y,z,t)$  on the wave front  $\Psi = ct$  can be represented by Eqn(4.18).

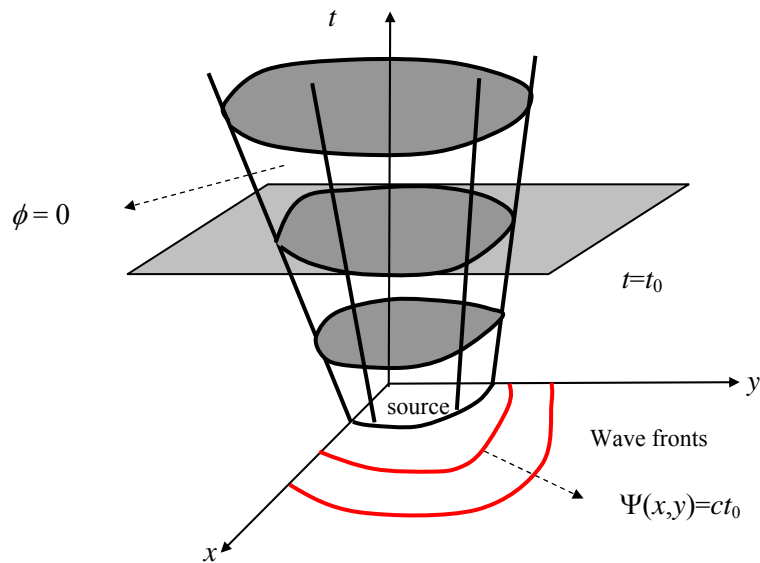


Figure 4-4: Wave fronts

$$\begin{aligned}\mathbf{E}^*(x,y,z) &= [\mathbf{E}] = \mathbf{E}(x,y,z,\Psi/c) \\ \mathbf{H}^*(x,y,z) &= [\mathbf{H}] = \mathbf{H}(x,y,z,\Psi/c)\end{aligned}\tag{4.18}$$

Thus  $\mathbf{E}^*$ ,  $\mathbf{H}^*$  give the values of GO field which is observed at  $(x,y,z)$  at time  $t = \Psi(x,y,z)/c$ . Recall that the values of  $\mathbf{E}$ ,  $\mathbf{H}$  on  $\phi = 0$  are the discontinuities and hence they must obey the discontinuity conditions of Eqn(4.12). But instead of it, since  $\phi = \Psi - ct = 0$  and  $\partial\phi/\partial t = -c$  and  $\nabla\phi = \nabla\Psi$ , we may write

$$\begin{aligned}\nabla\Psi \times \mathbf{E}^* - c\mu\mathbf{H}^* &= 0 \\ \nabla\Psi \times \mathbf{H}^* + c\varepsilon\mathbf{E}^* &= 0\end{aligned}\tag{4.19}$$

If we form the scalar product of each of these equations with  $\nabla\Psi$  and then form the scalar product of the first with  $\mathbf{H}^*$  and the second with  $\mathbf{E}^*$ , we see that

$$\mathbf{E}^* \cdot \mathbf{H}^* = 0, \quad \nabla\Psi \cdot \mathbf{E}^* = 0, \quad \nabla\Psi \cdot \mathbf{H}^* = 0\tag{4.20}$$

Thus the vectors  $\mathbf{E}^*$ ,  $\mathbf{H}^*$  are tangential to the wave front (normal to the  $\nabla\Psi$ ) and also perpendicular to each other. Hence the vectors  $\nabla\Psi$ ,  $[\mathbf{E}]$ ,  $[\mathbf{H}]$  are mutually orthogonal at any point on a discontinuity surface  $\phi = 0$  or on wave fronts  $\Psi = ct$ .  $\nabla\Psi$  is called as wave normal (normal to wave fronts) and denoted by vector  $\mathbf{p}$ .

$$\mathbf{p} = \nabla\Psi\tag{4.21}$$

$\mathbf{p}$  is not a unit vector but  $|\mathbf{p}| = n$ , index of refraction of medium. We consider next how the wave fronts  $\Psi(x,y,z) = ct$  move out into space. For a family of wave fronts  $\Psi = ct$ , there exists 2-parameter family of rays (orthogonal trajectories) to them. Each curve of the family of rays will then have the direction of  $\nabla\Psi$  at its intersection with the surface  $\Psi(x,y,z) = ct$ .

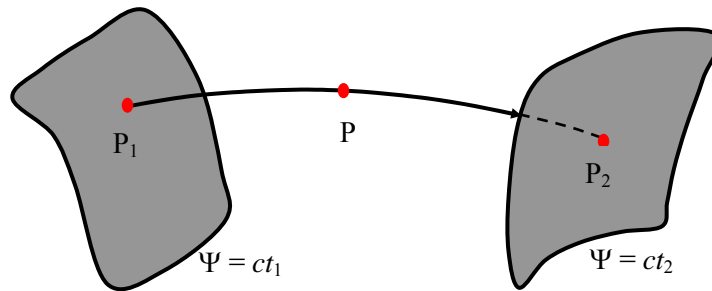


Figure 4-5: Propagation of a wave front

The velocity  $v$  of a wave front (phase velocity) or of  $\mathbf{E}^*$ ,  $\mathbf{H}^*$  which propagates with the wave front is the velocity with which a point  $P$  moves along rays normal to the family of wave fronts as  $t$  increases (Figure 4-5). Rays can be written in parametric form as:

$$x = x(t), \quad y = y(t), \quad z = z(t) \quad (4.22)$$

Then the velocity  $v$  along ray is

$$v = \left| \frac{dx}{dt} \hat{\mathbf{x}} + \frac{dy}{dt} \hat{\mathbf{y}} + \frac{dz}{dt} \hat{\mathbf{z}} \right| \quad (4.23)$$

Noting that wave front  $\Psi$  can also be written as  $\Psi((x(t),y(t),z(t)) = ct$  and since

$$\frac{\partial \Psi}{\partial t} = \frac{\partial \Psi}{\partial x} \frac{\partial x}{\partial t} + \frac{\partial \Psi}{\partial y} \frac{\partial y}{\partial t} + \frac{\partial \Psi}{\partial z} \frac{\partial z}{\partial t} = c \quad (4.24)$$

$v$  is determined as

$$v = \frac{c}{|\nabla \Psi|} = \frac{c}{n} \quad (4.25)$$

We have introduced the rays as the orthogonal trajectories of wave fronts  $\Psi = ct$ . However one can get rid of  $\Psi$  to specify rays. In this case totality of rays in a given medium is a 4-parameter family of curves in  $(x,y,z)$ -space and can be characterized independently of the wave front function  $\Psi$ . The following system of equations describe all the rays in a medium.

$$\frac{d^2 x}{d\tau^2} = \frac{\partial}{\partial x} \left( \frac{n^2}{2} \right), \quad \frac{d^2 y}{d\tau^2} = \frac{\partial}{\partial y} \left( \frac{n^2}{2} \right), \quad \frac{d^2 z}{d\tau^2} = \frac{\partial}{\partial z} \left( \frac{n^2}{2} \right) \quad (4.26)$$

$$\left( \frac{dx}{d\tau} \right)^2 + \left( \frac{dy}{d\tau} \right)^2 + \left( \frac{dz}{d\tau} \right)^2 = n^2 \quad (4.27)$$

$\tau$  is a parameter along ray and related to arc length  $s$  by  $ds = n d\tau$  and to time  $t$  by  $t = n^2 \tau / c$ . These ODEs are called characteristic DEs of Eiconal equation. However, since Eiconal is itself the characteristic DE of Maxwell's equations. The system of ODEs is called bicharacteristic DEs of Maxwell's equations and its solutions are called bicharacteristics. Discontinuities exist on  $\phi(x,y,z,t) = 0$  characteristics and propagate along bicharacteristics. Wave fronts and rays of GO are projections of characteristics and bicharacteristics onto  $(x,y,z)$ -space respectively (Figure 4-6). If one knows the equation of rays, he can also know the equations of wave fronts which belong to the problem and vice-versa.

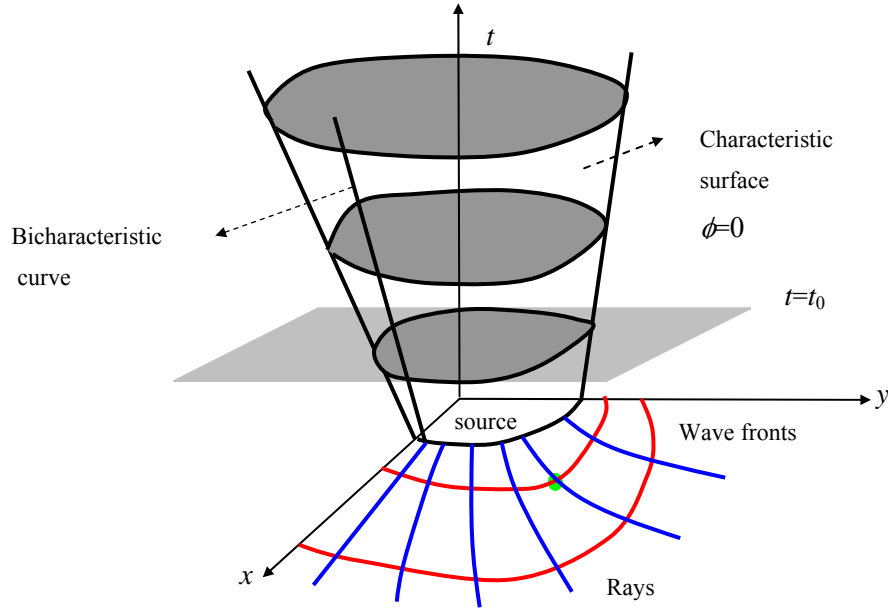


Figure 4-6: Characteristics, bicharacteristics, wave fronts and rays

### 4.5.3 Fermat's Principle

Eqn(4.24) in fact is the rate of change of distance with respect to time of a point P which moves with the front but along the ray normal to  $\Psi = ct$ . If we denote the arc length along the ray between two neighboring wave fronts by  $ds$ , then what have been found is  $v = ds/dt$ . Then the optical path length  $L$  from  $P_1$  to  $P_2$  along ray is

$$L = \Psi(P_1) - \Psi(P_2) = c(t_2 - t_1) = \int_{P_1}^{P_2} n v dt = \int_{P_1}^{P_2} n ds \quad (4.28)$$

Fermat's principle states that the actual path between two points taken by a signal is the one which renders the time of travel stationary. Rays described above satisfy Fermat's principle.

### 4.5.4 Power and Energy

We next consider the energy that exists on a wave front. GO electric and magnetic energy densities are equal on a wave front and are given by

$$W^* = (1/2)(\mathbf{E}^* \cdot \mathbf{D}^* + \mathbf{H}^* \cdot \mathbf{B}^*) = \mathbf{E}^* \cdot \mathbf{D}^* = \mathbf{H}^* \cdot \mathbf{B}^* \quad (4.29)$$

where  $W^*$  denotes the total GO energy density on a wave front. The energy of GO fields moves along the rays. Poynting vector (GO power density) on a wave front is defined by

$$\mathbf{S}^* = \mathbf{E}^* \times \mathbf{H}^* \quad (4.30)$$

$\mathbf{S}^*$  has the direction of  $\mathbf{p}$  and energy flows in ray direction. Associated with  $\mathbf{S}^*$ , we can define a vector  $\mathbf{s}$  such that

$$\mathbf{S}^* = W^* \mathbf{s} \quad (4.31)$$

Also note that  $\mathbf{s} \cdot \mathbf{p} = 1$ . In isotropic medium which is the scope of this thesis, since  $\varepsilon, \mu$  are scalars,  $\mathbf{p}$  and  $\mathbf{s}$  have the same direction. In anisotropic medium, they are not parallel, that is, energy flow is in the ray direction but this time rays are not normal to the wave fronts.

#### 4.5.5 Propagation of Geometrical Optics Fields

Next step is to examine the variation of GO field and GO energy along rays. This variation of GO fields will be described by linear, 1<sup>st</sup> order homogeneous ODEs called *transport equations*. Since  $\mathbf{E}^*, \mathbf{H}^*$  are the discontinuities in the solution  $\mathbf{E}(x,y,z,t), \mathbf{H}(x,y,z,t)$  of Maxwell's equations, the transport equations tell us how discontinuities propagate. The transport equations are valid in regions in which  $\varepsilon, \mu, \sigma$  are smooth. Then we shall discuss the solution of vector transport equations. The propagation of  $\mathbf{E}^*, \mathbf{H}^*$  across a discontinuity in the medium will also be treated. We start with discontinuity conditions again.

$$\mathbf{p} \times \mathbf{E}^* - c\mu \mathbf{H}^* = 0 \quad (4.32)$$

$$\mathbf{p} \times \mathbf{H}^* + c\varepsilon \mathbf{E}^* = 0 \quad (4.33)$$

However these equations do not suffice to determine  $\mathbf{E}^*, \mathbf{H}^*$  because the determinant of the coefficient matrix, i.e., Eiconal equation  $|\nabla\Psi|^2 - n^2 = 0$ . Therefore we must seek additional conditions on  $\mathbf{E}^*$  and  $\mathbf{H}^*$ . We have by straightforward differentiation,

$$\begin{aligned} \nabla \times \mathbf{E}^* &= (\nabla \times \mathbf{E})^* + \frac{1}{c} \mathbf{p} \times \left( \frac{\partial \mathbf{E}}{\partial t} \right)^* \\ \nabla \times \mathbf{H}^* &= (\nabla \times \mathbf{H})^* + \frac{1}{c} \mathbf{p} \times \left( \frac{\partial \mathbf{H}}{\partial t} \right)^* \end{aligned} \quad (4.34)$$

And from Maxwell's equations we have

$$\begin{aligned} \nabla \times \mathbf{E} &= -\mu \frac{\partial \mathbf{H}}{\partial t} \\ \nabla \times \mathbf{H} &= \varepsilon \frac{\partial \mathbf{E}}{\partial t} \end{aligned} \quad (4.35)$$

Using Eqns(4.34),(4.35) we arrive at the following additional (consistency) condition,

$$\begin{aligned} -\mathbf{p} \times \left( \frac{\partial \mathbf{E}}{\partial t} \right)^* + c\mu \left( \frac{\partial \mathbf{H}}{\partial t} \right)^* &= -c\nabla \times \mathbf{E}^* \\ c\varepsilon \left( \frac{\partial \mathbf{E}}{\partial t} \right)^* + \mathbf{p} \times \left( \frac{\partial \mathbf{H}}{\partial t} \right)^* &= c\nabla \times \mathbf{H}^* \end{aligned} \quad (4.36)$$

After some vector algebra [92], transport equation for  $\mathbf{E}^*$  can be found as:

$$\frac{d\mathbf{E}^*}{d\tau} + \frac{1}{2} \mu \nabla \cdot \left( \frac{\mathbf{p}}{\mu} \right) \mathbf{E}^* + \frac{\nabla \mathbf{n} \cdot \mathbf{E}^*}{n} \mathbf{p} = 0 \quad (4.37)$$

Noting that

$$\mu \nabla \cdot \left( \frac{\mathbf{p}}{\mu} \right) = \mu \frac{\partial}{\partial x} \left( \frac{\partial \Psi}{\mu \partial x} \right) + \mu \frac{\partial}{\partial y} \left( \frac{\partial \Psi}{\mu \partial y} \right) + \mu \frac{\partial}{\partial z} \left( \frac{\partial \Psi}{\mu \partial z} \right) = \Delta_{\mu} \Psi \quad (4.38)$$

Eqn(4.37) becomes

$$\frac{d \mathbf{E}^*}{d\tau} + \frac{1}{2} (\Delta_{\mu} \Psi) \mathbf{E}^* + \frac{\nabla \mathbf{n} \cdot \mathbf{E}^*}{\mathbf{n}} \nabla \Psi = 0 \quad (4.39)$$

which is a vector ODE for GO field  $\mathbf{E}^*$  and holds along any ray  $(x(\tau), y(\tau), z(\tau))$ . Similar formula can be written for  $\mathbf{H}^*$  with  $\Delta_{\mu}$  replaced by  $\Delta_{\epsilon}$ . Further,  $\Delta_{\mu}$  can be expressed as

$$\Delta_{\mu} \Psi = \mathbf{n}^2 \nabla \cdot \mathbf{s} + \frac{1}{\epsilon} \frac{d\epsilon}{d\tau} \quad (4.40)$$

Substituting this into Eqn(4.39), we end up with

$$\frac{d(\sqrt{\epsilon} \mathbf{E}^*)}{d\tau} + \frac{1}{2} (\mathbf{n}^2 \nabla \cdot \mathbf{s}) (\sqrt{\epsilon} \mathbf{E}^*) + \frac{\nabla \mathbf{n} \cdot (\sqrt{\epsilon} \mathbf{E}^*)}{\mathbf{n}} \mathbf{p} = 0 \quad (4.41)$$

Thus the vector  $\sqrt{\epsilon} \mathbf{E}^*$  satisfies the same ODE. Transport equations are coupled system of scalar ODEs. Each equation involves,  $E_x^*$ ,  $E_y^*$ ,  $E_z^*$ . For special values of  $\mathbf{n}$ , e.g., in homogeneous medium where  $\nabla \mathbf{n} = 0$ , these equations may be uncoupled.

#### 4.5.6 Solution of Transport Equations

We shall now work directly with the vector ODE and integrate them to obtain solution. We will observe some results concerning the energy density  $W^*$  which yields physical facts about GO field. First we will introduce vectors  $\mathbf{P}$  (for  $\mathbf{E}^*$ ) and  $\mathbf{Q}$  (for  $\mathbf{H}^*$ ) such that

$$\sqrt{\epsilon} \mathbf{E}^* = \sqrt{W^*} \mathbf{P}, \quad \sqrt{\epsilon} \mathbf{H}^* = \sqrt{W^*} \mathbf{Q} \quad (4.42)$$

Substitution of this  $\mathbf{P}$  into Eqn(4.41) yields a simpler form than Eqn(4.41).

$$\frac{d \mathbf{P}}{d\tau} + \frac{\mathbf{P} \cdot \nabla \mathbf{n}}{\mathbf{n}} \nabla \Psi = 0 \quad (4.43)$$

In order to utilize this equation for the purpose finding  $\mathbf{E}^*$  we must know  $W^*$ .  $W^*$  holds the following relation in nonconducting medium.

$$\frac{W^*(\tau)}{\mathbf{n}(\tau)K(\tau)} = \frac{W^*(\tau_0)}{\mathbf{n}(\tau_0)K(\tau_0)} \quad (4.44)$$

Here  $\tau_0$  characterizes an initial point along a ray, and  $\tau$  an arbitrary point.  $K(\tau)$  measures the expansion of the wave front along a ray. First we find  $\mathbf{P}$  by Eqn(4.43), then  $W^*(\tau)$  by Eqn(4.44). Finally  $\mathbf{E}^*$  is determined. ICs for  $\mathbf{P}$  is determined by ICs of  $\mathbf{E}^*$  and  $W^*$ . Note that  $|\mathbf{P}|$  is constant for all  $\tau$ , i.e., along a ray and it is unitary vector. Eqns(4.41),(4.43) are themselves interesting because they show that the behavior of  $\mathbf{E}^*$ ,  $\mathbf{P}$  along a ray depend only

on the ray. But the same ray may belong to many different sets of wave fronts. For example a straight line can be orthogonal to both spherical wave fronts and plane wave fronts. Although transport equations exhibit no dependence on wave fronts, wave fronts do determine the ICs for  $\mathbf{E}^*$ ,  $\mathbf{H}^*$  and therefore of  $W^*$  as well as the growth of  $W^*$  along a ray.

#### 4.5.7 Reflection/Refraction Across Discontinuity in the Medium

In our treatment upto now, we assumed the functions  $\varepsilon$ ,  $\mu$ ,  $\sigma$  are continuous. Then the wave fronts progress smoothly in the medium and transport equations hold. By solving these equations we obtain the behavior of  $\mathbf{E}^*$ ,  $\mathbf{H}^*$ . However when the medium possesses a discontinuity in any or all of the  $\varepsilon$ ,  $\mu$ ,  $\sigma$ , then not only do the transport equations not apply across the discontinuity but also the wave front does not propagate smoothly across the discontinuity because wave front is subject to a PDE involving  $\varepsilon$ ,  $\mu$ .

Now we start by defining an isotropic medium whose parameters  $\varepsilon$ ,  $\mu$ ,  $\sigma$  are piecewise smooth, i.e., they are continuous except on a finite number of surfaces. When a wave front strikes a discontinuity in a medium, it gives rise to a reflected and a refracted wave front. These two new families of wave fronts propagate out from the discontinuity. If several discontinuities are present in the same medium, then multiple families of wave fronts are generated overlapping in  $(x,y,z)$ -space as shown in Figure 4-7.

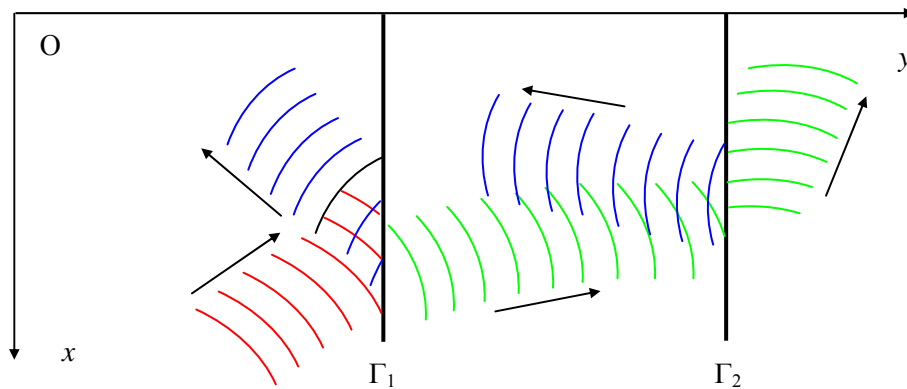


Figure 4-7: Reflection and refraction in  $(x,y)$ -space

We must also think in terms of what happens in  $(x,y,z,t)$ -space. Figure 4-8 illustrates schematically the discontinuity hypersurfaces generated by an incident surface from left on discontinuity surface  $\Gamma_1$  and then on  $\Gamma_2$ . A discontinuity in the medium may be pictured as a

hypercylinder in  $(x,y,z,t)$ -space parallel to  $t$ -axis. Each family of wave fronts is a discontinuity hypersurface. Incident hypersurface  $\Psi^i-ct=0$  generates a reflected and a refracted hypersurface  $\Psi^r-ct=0$ ,  $\Psi^t-ct=0$  at  $\Gamma_1$ .

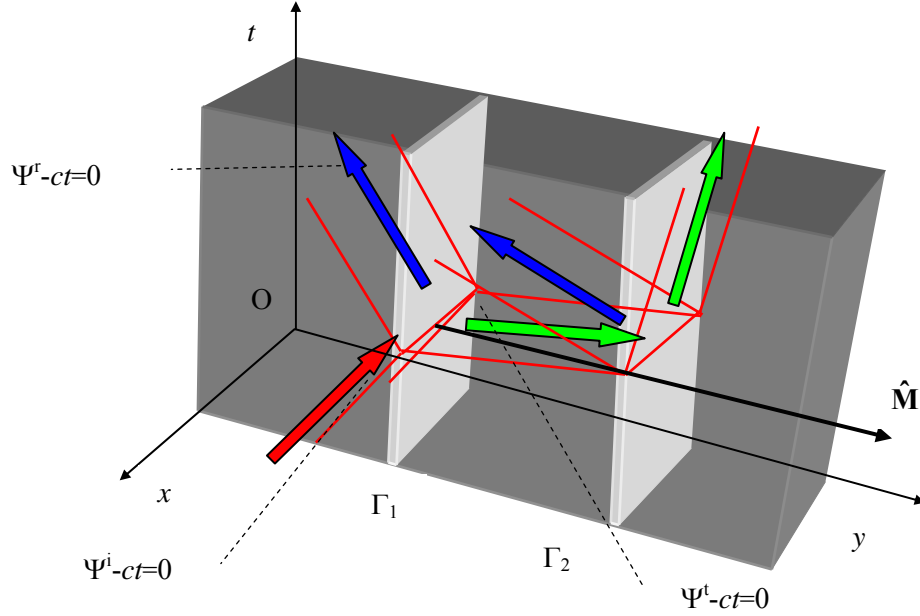


Figure 4-8: Incident, reflected and refracted hypersurfaces in  $(x,y,t)$ -space

Hypersurfaces meet on  $\Gamma_1$ . Since  $\Gamma_1$  is independent of  $t$ , it can be represented by

$$x = f(\xi, \eta), \quad y = g(\xi, \eta), \quad z = h(\xi, \eta) \quad (4.45)$$

They also meet at any point  $(x,y,z)$  on  $\Gamma_1$  at the same time  $t$ . Hence we must have

$$\Psi^i(f(\xi, \eta), g(\xi, \eta), h(\xi, \eta)) = \Psi^r(f(\xi, \eta), g(\xi, \eta), h(\xi, \eta)) = \Psi^t(f(\xi, \eta), g(\xi, \eta), h(\xi, \eta)) \quad (4.46)$$

for those  $\xi, \eta$  which lie in the domain of intersection of  $\Gamma_1$ . The vector  $\hat{\mathbf{M}}$  is the unit normal to surface  $\Gamma_1$ . At any  $(x,y,z)$  it is the same for all  $t$  because  $\Gamma_1$  is a hypercylinder. Normals to each family of wave fronts are also introduced as:

$$\begin{aligned} \mathbf{p}^i &= \frac{\partial \Psi^i}{\partial x} \hat{\mathbf{x}} + \frac{\partial \Psi^i}{\partial y} \hat{\mathbf{y}} + \frac{\partial \Psi^i}{\partial z} \hat{\mathbf{z}}, & \mathbf{p}^r &= \frac{\partial \Psi^r}{\partial x} \hat{\mathbf{x}} + \frac{\partial \Psi^r}{\partial y} \hat{\mathbf{y}} + \frac{\partial \Psi^r}{\partial z} \hat{\mathbf{z}} \\ \mathbf{p}^t &= \frac{\partial \Psi^t}{\partial x} \hat{\mathbf{x}} + \frac{\partial \Psi^t}{\partial y} \hat{\mathbf{y}} + \frac{\partial \Psi^t}{\partial z} \hat{\mathbf{z}} \end{aligned} \quad (4.47)$$

$\mathbf{p}^i, \mathbf{p}^r, \mathbf{p}^t$  are vectors along the incident, reflected and refracted rays. All four vectors lie in the plane of  $\mathbf{p}^i$  and  $\hat{\mathbf{M}}$ , i.e., plane of incidence (Figure 4-9). It can be inferred that

$$\mathbf{p}^r \times \hat{\mathbf{M}} = \mathbf{p}^i \times \hat{\mathbf{M}}, \quad \mathbf{p}^t \times \hat{\mathbf{M}} = \mathbf{p}^i \times \hat{\mathbf{M}} \quad (4.48)$$

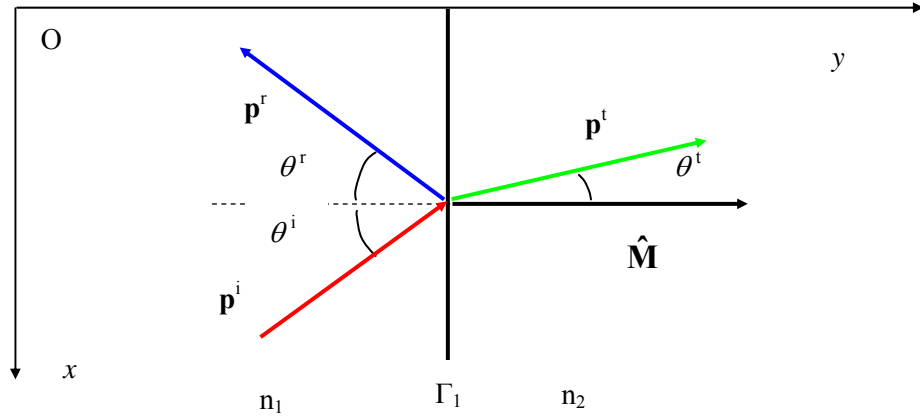


Figure 4-9: Snell's law of reflection and refraction

Using the fact that  $|\mathbf{p}^i| = |\mathbf{p}^r| = n_1$ , and  $|\mathbf{p}^t| = n_2$  are indices of two media, then we have well-known Snell's law of reflection and refraction

$$\sin \theta^r = \sin \theta^i, \quad n_2 \sin \theta^t = n_1 \sin \theta^i \quad (4.49)$$

Now we consider how GO fields  $\mathbf{E}^*$ ,  $\mathbf{H}^*$  (discontinuities) propagate across the discontinuity (Figure 4-10).  $\Psi^i - ct = 0$  is incident discontinuity hypersurface emanating from source, then  $\mathbf{E}_4$ ,  $\mathbf{H}_4$  are identically zero. In region 0, there exist only incident fields which are  $\mathbf{E}_0$ ,  $\mathbf{H}_0$ .  $\mathbf{E}_1$ ,  $\mathbf{H}_1$  are the sum of the field stemming from source and additional field generated by reflection from  $\Gamma$ .

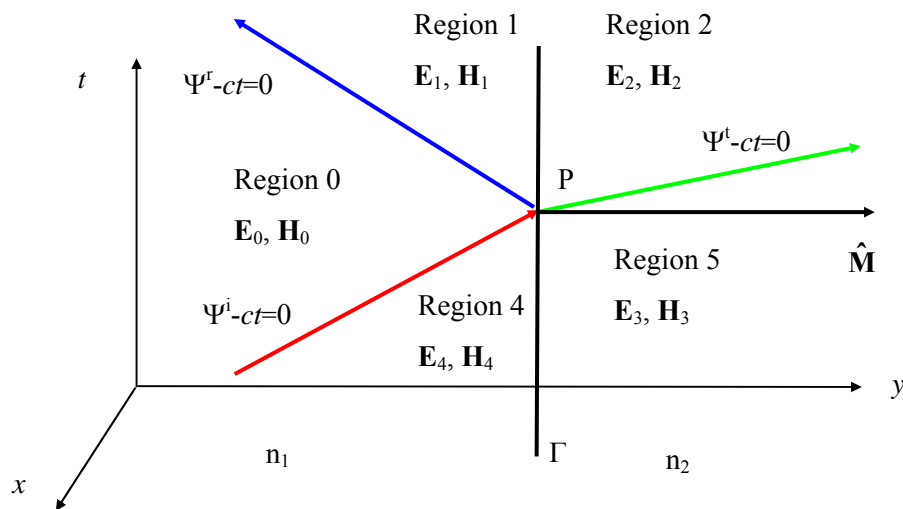


Figure 4-10: Reflection and refraction at discontinuity in time

This reflected field is present only above  $\Psi^r-ct=0$ .  $\mathbf{E}_2, \mathbf{H}_2$  are the refracted fields.  $\mathbf{E}_3, \mathbf{H}_3$  are identically zero because no field can exist to the right of  $\Gamma$  before the refracted field arises at P. Since  $\Gamma$  is a fixed discontinuity hypersurface ( $\phi = \Psi_0(x,y,z) \Rightarrow \partial\phi/\partial t = 0, \nabla\phi = \nabla\Psi_0$ ), upon applying discontinuity conditions in Eqn(4.12) at any point  $(x,y,z,t)$  on  $\Gamma$ , it is found that

$$\begin{aligned} (\mathbf{E}_1 - \mathbf{E}_2) \times \hat{\mathbf{M}} &= 0, & (\mathbf{E}_4 - \mathbf{E}_3) \times \hat{\mathbf{M}} &= 0 \\ (\mathbf{H}_1 - \mathbf{H}_2) \times \hat{\mathbf{M}} &= 0, & (\mathbf{H}_4 - \mathbf{H}_3) \times \hat{\mathbf{M}} &= 0 \end{aligned} \quad (4.50)$$

We consider next the discontinuities in  $\mathbf{E}(x,y,z,t), \mathbf{H}(x,y,z,t)$  on the hypersurfaces  $\Psi^i-ct=0, \Psi^r-ct=0, \Psi^t-ct=0$ . These discontinuities exist all along the hypersurfaces but we are interested in discontinuities at P on  $\Gamma$ . They can be written as:

$$\begin{aligned} \mathbf{E}^{i*}(x,y,z) &= \mathbf{E}^i(x,y,z,\Psi/c) = \mathbf{E}_0 - \mathbf{E}_4, & \mathbf{H}^{i*}(x,y,z) &= \mathbf{H}^i(x,y,z,\Psi/c) = \mathbf{H}_0 - \mathbf{H}_4 \\ \mathbf{E}^{r*}(x,y,z) &= \mathbf{E}^r(x,y,z,\Psi/c) = \mathbf{E}_1 - \mathbf{E}_0, & \mathbf{H}^{r*}(x,y,z) &= \mathbf{H}^r(x,y,z,\Psi/c) = \mathbf{H}_1 - \mathbf{H}_0 \\ \mathbf{E}^{t*}(x,y,z) &= \mathbf{E}^t(x,y,z,\Psi/c) = \mathbf{E}_2 - \mathbf{E}_3, & \mathbf{H}^{t*}(x,y,z) &= \mathbf{H}^t(x,y,z,\Psi/c) = \mathbf{H}_2 - \mathbf{H}_3 \end{aligned} \quad (4.51)$$

They represent jumps across the respective hypersurfaces  $\Psi^i-ct=0, \Psi^r-ct=0, \Psi^t-ct=0$  at P. From Eqns(4.50),(4.51) we can write

$$(\mathbf{E}^{i*} + \mathbf{E}^{r*}) \times \hat{\mathbf{M}} = \mathbf{E}^{i*} \times \hat{\mathbf{M}}, \quad (\mathbf{H}^{i*} + \mathbf{H}^{r*}) \times \hat{\mathbf{M}} = \mathbf{H}^{i*} \times \hat{\mathbf{M}} \quad (4.52)$$

But Eqn(4.52) is not sufficient to determine  $\mathbf{E}^{r*}, \mathbf{H}^{r*}, \mathbf{E}^{t*}, \mathbf{H}^{t*}$  from  $\mathbf{E}^{i*}, \mathbf{H}^{i*}$ . Hence additionally we can use the followings from discontinuity conditions.

$$\begin{aligned} \mathbf{p}^i \times \mathbf{H}^{i*} + c\varepsilon_1 \mathbf{E}^{i*} &= 0, & \mathbf{p}^r \times \mathbf{H}^{r*} + c\varepsilon_1 \mathbf{E}^{r*} &= 0, & \mathbf{p}^t \times \mathbf{H}^{t*} + c\varepsilon_2 \mathbf{E}^{t*} &= 0 \\ \mathbf{p}^i \times \mathbf{E}^{i*} - c\mu_1 \mathbf{H}^{i*} &= 0, & \mathbf{p}^r \times \mathbf{E}^{r*} - c\mu_1 \mathbf{H}^{r*} &= 0, & \mathbf{p}^t \times \mathbf{E}^{t*} - c\mu_2 \mathbf{H}^{t*} &= 0 \end{aligned} \quad (4.53)$$

Recall that  $\mathbf{p}^i, \mathbf{p}^r, \mathbf{p}^t$ , and  $\hat{\mathbf{M}}$  lie in the same plane. Now we can solve  $\mathbf{E}^{r*}, \mathbf{H}^{r*}, \mathbf{E}^{t*}, \mathbf{H}^{t*}$  from  $\mathbf{E}^{i*}, \mathbf{H}^{i*}$ . To do this, we introduce the unit vector  $\hat{\mathbf{S}}$  defined by

$$k \hat{\mathbf{S}} = \mathbf{p}^i \times \hat{\mathbf{M}} = \mathbf{p}^r \times \hat{\mathbf{M}} = \mathbf{p}^t \times \hat{\mathbf{M}} \quad (4.54)$$

where  $k = n_1 \sin\theta^i = n_1 \sin\theta^r = n_2 \sin\theta^t$ . We also introduce three other unit vectors, namely,

$$\hat{\mathbf{N}}^i = \hat{\mathbf{S}} \times (\mathbf{p}^i/n_1), \quad \hat{\mathbf{N}}^r = \hat{\mathbf{S}} \times (\mathbf{p}^r/n_1), \quad \hat{\mathbf{N}}^t = \hat{\mathbf{S}} \times (\mathbf{p}^t/n_1) \quad (4.55)$$

As a result we have three sets of orthogonal triples  $(\mathbf{p}^i, \hat{\mathbf{S}}, \hat{\mathbf{N}}^i), (\mathbf{p}^r, \hat{\mathbf{S}}, \hat{\mathbf{N}}^r), (\mathbf{p}^t, \hat{\mathbf{S}}, \hat{\mathbf{N}}^t)$ . Since  $\mathbf{E}^{i*}, \mathbf{H}^{i*}$  are orthogonal to  $\mathbf{p}^i$  and the same is true for reflected, refracted fields and wave fronts, we may express each field in terms of linear combination of parallel and perpendicular components to the plane of incidence such as

$$\begin{aligned} \sqrt{\varepsilon_1} \mathbf{E}^{i*} &= \alpha^i \hat{\mathbf{N}}^i + \beta^i \hat{\mathbf{S}}, & \sqrt{\varepsilon_1} \mathbf{E}^{r*} &= \alpha^r \hat{\mathbf{N}}^r + \beta^r \hat{\mathbf{S}}, & \sqrt{\varepsilon_2} \mathbf{E}^{t*} &= \alpha^t \hat{\mathbf{N}}^t + \beta^t \hat{\mathbf{S}} \\ \sqrt{\mu_1} \mathbf{H}^{i*} &= -\beta^i \hat{\mathbf{N}}^i + \alpha^i \hat{\mathbf{S}}, & \sqrt{\mu_1} \mathbf{H}^{r*} &= -\beta^r \hat{\mathbf{N}}^r + \alpha^r \hat{\mathbf{S}}, & \sqrt{\mu_2} \mathbf{H}^{t*} &= -\beta^t \hat{\mathbf{N}}^t + \alpha^t \hat{\mathbf{S}} \end{aligned} \quad (4.56)$$

We have four unknowns  $(\alpha^r, \beta^r, \alpha^t, \beta^t)$  and two knowns  $(\alpha^i, \beta^i)$ . Using Eqns(4.52), (4.55) and (4.56) we obtain four scalar equations for  $(\alpha^r, \beta^r, \alpha^t, \beta^t)$  which are

$$\begin{aligned}\alpha^r - \alpha^i &= -\sqrt{\varepsilon_1/\varepsilon_2} \frac{\cos \theta^t}{\cos \theta^i} \alpha^t, & \alpha^r + \alpha^i &= \sqrt{\mu_1/\mu_2} \alpha^t \\ \beta^r - \beta^i &= -\sqrt{\mu_1/\mu_2} \frac{\cos \theta^t}{\cos \theta^i} \beta^t, & \beta^r + \beta^i &= \sqrt{\varepsilon_1/\varepsilon_2} \beta^t\end{aligned}\quad (4.57)$$

By means of Eqn(4.57),  $(\alpha^r, \beta^r, \alpha^t, \beta^t)$  can be expressed in terms of  $(\alpha^i, \beta^i)$

$$\begin{aligned}\frac{\alpha^t}{\alpha^i} &= \frac{2}{\sqrt{\mu_1/\mu_2} + \sqrt{\varepsilon_1/\varepsilon_2} \frac{\cos \theta^t}{\cos \theta^i}}, & \frac{\alpha^r}{\alpha^i} &= \frac{\sqrt{\mu_1/\mu_2} - \sqrt{\varepsilon_1/\varepsilon_2} \frac{\cos \theta^t}{\cos \theta^i}}{\sqrt{\mu_1/\mu_2} + \sqrt{\varepsilon_1/\varepsilon_2} \frac{\cos \theta^t}{\cos \theta^i}} \\ \frac{\beta^t}{\beta^i} &= \frac{2}{\sqrt{\varepsilon_1/\varepsilon_2} + \sqrt{\mu_1/\mu_2} \frac{\cos \theta^t}{\cos \theta^i}}, & \frac{\beta^r}{\beta^i} &= \frac{\sqrt{\varepsilon_1/\varepsilon_2} - \sqrt{\mu_1/\mu_2} \frac{\cos \theta^t}{\cos \theta^i}}{\sqrt{\varepsilon_1/\varepsilon_2} + \sqrt{\mu_1/\mu_2} \frac{\cos \theta^t}{\cos \theta^i}}\end{aligned}\quad (4.58)$$

Note that normal and parallel components of  $\mathbf{E}^{i*}$  is  $\beta^i/\sqrt{\varepsilon_1}$  and  $\alpha^i/\sqrt{\varepsilon_1}$  respectively. Then for normal and parallel components, we end up with

$$\begin{aligned}E_{\perp}^t &= \frac{2\sqrt{\varepsilon_1/\varepsilon_2}}{\sqrt{\varepsilon_1/\varepsilon_2} + \sqrt{\mu_1/\mu_2} \frac{\cos \theta^t}{\cos \theta^i}} E_{\perp}^i, & E_{\parallel}^t &= \frac{2\sqrt{\varepsilon_1/\varepsilon_2}}{\sqrt{\mu_1/\mu_2} + \sqrt{\varepsilon_1/\varepsilon_2} \frac{\cos \theta^t}{\cos \theta^i}} E_{\parallel}^i \\ E_{\perp}^r &= \frac{\sqrt{\varepsilon_1/\varepsilon_2} - \sqrt{\mu_1/\mu_2} \frac{\cos \theta^t}{\cos \theta^i}}{\sqrt{\varepsilon_1/\varepsilon_2} + \sqrt{\mu_1/\mu_2} \frac{\cos \theta^t}{\cos \theta^i}} E_{\perp}^i, & E_{\parallel}^r &= \frac{\sqrt{\mu_1/\mu_2} - \sqrt{\varepsilon_1/\varepsilon_2} \frac{\cos \theta^t}{\cos \theta^i}}{\sqrt{\mu_1/\mu_2} + \sqrt{\varepsilon_1/\varepsilon_2} \frac{\cos \theta^t}{\cos \theta^i}} E_{\parallel}^i\end{aligned}\quad (4.59)$$

The same decomposition for reflected and refracted magnetic GO field  $\mathbf{H}^*$  can be written. In the case of normal incidence these formulas becomes much simpler. These formulas are supplement to transport equations because we can calculate GO field across discontinuity in the medium by means of them. They furnish ICs for reflected and refracted wave fronts. Note that Eqn(4.59) are identical with the Fresnel formulas, which are usually derived to show how a plane wave reflects and refracts on a plane interface between two media. Plane waves are often used to show how Maxwell's equations yield the GO field and the basic laws of GO. But this approach is not complete for our purpose because GO field follows rays and each ray is an independent part of that field. Our treatment shows what happens along any one ray. And also in our treatment, refracting surface  $\Gamma$  can be a curved space in  $(x,y,z)$ -space as well as a plane. Moreover incident wave front can be of any shape and the media on both sides of interface  $\Gamma$  can be inhomogeneous. Also note that although we permitted the two media to have conductivities  $(\sigma_1, \sigma_2)$ , they play no role in determining the

reflected and refracted fields at the interface. They do enter into transport equations and attenuate the refracted field as it proceeds into refracting medium and the reflected field as it travels back into the first medium.

## CHAPTER 5

### GEOMETRICAL OPTICS FOR TIME-DOMAIN ELECTROMAGNETICS

#### 5.1 Introduction

In Chapter 4, we have presented GO field  $\mathbf{E}^*$  and showed that the field  $\mathbf{E}(x,y,z,t)$ , evaluated at  $(x,y,z,t)$  which lie on discontinuity hypersurfaces  $\phi(x,y,z,t) = 0$ , consists of special values of solutions of Maxwell's equations. In other words, GO field is the finite discontinuities of  $\mathbf{E}$  on the wave fronts at the time any wave front is at a given  $(x,y,z)$ . Such field follows their own laws, that is, its behavior can be determined without knowing its behavior off the discontinuity hypersurface. And the determination of  $\mathbf{E}$  on the wave fronts can be made independently of what happens at a given  $(x,y,z)$  at a later time than the  $t$  which satisfies  $t = \Psi(x,y,z)/c_0$ . However, full solutions of Maxwell's equations hold for a larger range of  $(x,y,z,t)$  values. Therefore we can seek exact solution of  $\mathbf{E}(x,y,z,t)$  for a given problem. Our objective here is to obtain information about solutions of Maxwell's equations, which may have arbitrary time dependence, by improving the GO solution. A feasible approach is to obtain a series for  $\mathbf{E}(x,y,z,t)$  at a specified  $(x,y,z)$  in powers of  $(t - t_0)$  where  $t_0$  is the value of  $t$  at which  $\phi(x,y,z,t) = 0$ . Geometrically this approach has the following meaning.

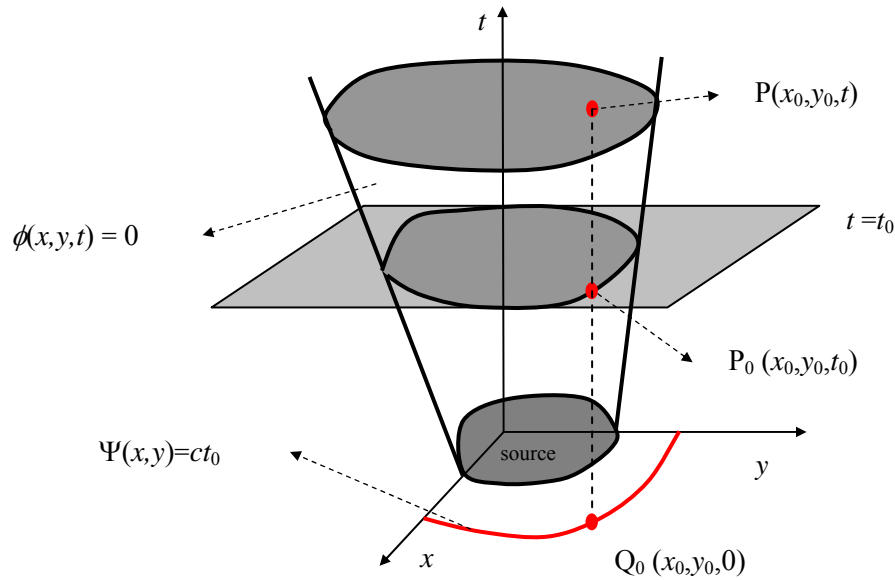


Figure 5-1: Improvement over GO for time dependent fields

Considering Figure 5-1, note that field is nonzero inside the hypercone and  $P_0$  lies on the cone. Point P is inside the cone with the same  $(x_0, y_0)$  as  $P_0$  but a value of  $t > t_0$ . We shall seek a representation of the field  $\mathbf{E}(x_0, y_0, t)$  at point P in terms of Taylor's series expansion around  $(x_0, y_0, t_0)$  in powers of  $(t - t_0)$ . Since  $(x_0, y_0)$  may be any point on  $\phi(x, y, t_0) = 0$  for a given  $t_0$ , the series will be valid for all such  $(x_0, y_0, t_0)$  and the corresponding  $(x_0, y_0, t)$ . Thus the series give the field at all points  $(x_0, y_0, t)$  in a region inside the hypercone in terms of the values on a section of the cone itself. This result has a helpful interpretation in  $(x, y, z)$ -space also. The wave front at time  $t_0$  is the projection of the section  $t = t_0$  of the hypercone onto  $(x, y, z)$ -space. Then Point  $P_0$  projects into the point  $Q_0$  on the wave front  $\Psi(x, y, z) = ct_0$ . But all the points on the line segment from  $P_0$  to P have the same  $(x, y, z)$  but differ only in  $t$  values. Hence our expansion gives the behavior of the field  $\mathbf{E}(x_0, y_0, z_0, t)$  at a point  $(x_0, y_0, z_0)$  at time  $t > t_0$ , at which the wave front  $\Psi(x, y, z) = ct_0$  passes through the point  $(x_0, y_0, z_0)$ . In other words, we remain at  $(x_0, y_0, z_0)$  on the wave front  $\Psi(x, y, z) = ct_0$  and then seek the subsequent behavior of  $\mathbf{E}(x_0, y_0, z_0, t)$  after  $t_0$ , at which the field first becomes nonzero. Then the power series for  $\mathbf{E}$  in  $(x, y, z, t)$ -space should have the form of

$$\begin{aligned} \mathbf{E}(x_0, y_0, z_0, t) = & [\mathbf{E}(x_0, y_0, z_0, t_0)] + [\partial \mathbf{E}(x_0, y_0, z_0, t_0) / \partial t](t - t_0) \\ & + \left[ \frac{\partial^2 \mathbf{E}(x_0, y_0, z_0, t_0)}{\partial t^2} \right] \frac{(t - t_0)^2}{2} + \dots \end{aligned} \quad (5.1)$$

for  $t > t_0$  and for any definite  $(x_0, y_0, z_0, t_0)$  satisfying  $\phi(x, y, z, t) = \Psi(x, y, z) - ct = 0$ . The coefficients in Eqn(5.1) are the values of pulse solution and its *successive time derivatives* on the discontinuity hypersurface  $\phi = 0$  or on the wave fronts  $\Psi = ct$ . Since these functions are discontinuous on  $\phi = 0$  or  $\Psi = ct$ , what we want are discontinuities in the solution and in its successive time derivatives. For example the first coefficient  $[\mathbf{E}(x_0, y_0, z_0, t_0)]$  is  $\mathbf{E}^*(x_0, y_0, z_0)$ , the GO field itself of Chapter 4. Hence the series Eqn(5.1) is an improvement on the GO field in the direction of an exact solution of Maxwell's equations.

In Chapter 4, we have examined how to determine GO fields. In order to obtain discontinuity conditions for the successive time derivatives, we will proceed as in Chapter 4 because we still deal with discontinuities of solutions of Maxwell's equations. Hence we must have similar IEs which accept these discontinuous solutions. Moreover just it has been found that GO fields satisfy ODE along the rays, so it will be found that discontinuities in the successive time derivatives also satisfy ODEs which express their variation along the rays. These differential equations are also linear, 1<sup>st</sup> order ODEs but now *nonhomogeneous*. They are called as the *higher transport equations*. Then we show how these vector transport equations can be solved.

The presentation in this chapter also applies to discontinuities on reflected and refracted hypersurfaces as well as to the discontinuities emanating from the source. Hence we will also consider series expansion in the neighborhood of those discontinuity hypersurfaces.

Luneburg in his lectures at NY University in 1947-48, pointed out that discontinuities in  $\mathbf{E}$  and its successive time-derivatives are coefficients in an asymptotic series representation of time-harmonic fields, Eqn(4.1). The study of discontinuities in  $\mathbf{E}$  themselves had already been carried out by Luneburg [1] for the purpose of GO. Kline [92] undertook the study of higher discontinuities by basing the entire theory on the IEs and obtained the derivation of the *higher discontinuity conditions* and of the *higher transport equations*. The method of solving the vector higher transport equations is due to Kline [92]. The entire theory for Maxwell's equations discussed here is also applicable to general 2<sup>nd</sup> order linear hyperbolic PDE such as scalar/vector wave equation, or to linearized acoustic problems [94], [95].

## 5.2 Discontinuity Conditions for Higher Discontinuities

Maxwell's equations in isotropic, nonconducting medium are repeated here for convenience.

$$\begin{aligned}\nabla \times \mathbf{E} &= -\mu \frac{\partial \mathbf{H}}{\partial t} \\ \nabla \times \mathbf{H} &= \varepsilon \frac{\partial \mathbf{E}}{\partial t} + \frac{\partial \mathbf{F}}{\partial t}\end{aligned}\tag{5.2}$$

$\varepsilon$ ,  $\mu$ , and  $\mathbf{F}$  are assumed to be sectionally analytic that the discontinuities in  $\mathbf{F}$  and its successive derivatives are *finite*. The source  $\mathbf{F}$  and hence fields  $\mathbf{E}$ ,  $\mathbf{H}$  are zero for  $t < 0$  because of causality.  $\mathbf{E}$ ,  $\mathbf{H}$  are assumed to be smooth functions in subdomains and the discontinuities in  $\mathbf{E}$ ,  $\mathbf{H}$  and their successive time derivatives are also finite (*finite jumps*) on  $\phi = 0$  as approached through  $G_1$  or  $G_2$  as discussed in Chapter 4.

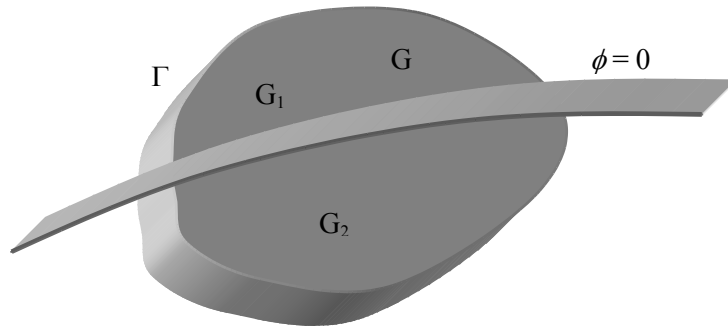


Figure 5-2: Discontinuity hypersurface crossing  $\Gamma$

Then using the same reasoning, IEs for higher discontinuities of  $\mathbf{E}$ ,  $\mathbf{H}$  can be written as:

$$\begin{aligned}
\int_{\Gamma} (\nabla \frac{\partial \Omega}{\partial t} \times \mathbf{E} + \frac{\partial^2 \Omega}{\partial t^2} \mu \mathbf{H}) dw &= 0 \\
\int_{\Gamma} (\nabla \frac{\partial \Omega}{\partial t} \times \mathbf{H} - \frac{\partial^2 \Omega}{\partial t^2} \varepsilon \mathbf{E} - \frac{\partial^2 \Omega}{\partial t^2} \mathbf{F}) dw &= 0 \\
\int_{\Gamma} (\nabla \frac{\partial^2 \Omega}{\partial t^2} \times \mathbf{E} + \frac{\partial^3 \Omega}{\partial t^3} \mu \mathbf{H}) dw &= 0 \\
\int_{\Gamma} (\nabla \frac{\partial^2 \Omega}{\partial t^2} \times \mathbf{H} - \frac{\partial^3 \Omega}{\partial t^3} \varepsilon \mathbf{E} - \frac{\partial^3 \Omega}{\partial t^3} \mathbf{F}) dw &= 0 \\
&\vdots
\end{aligned} \tag{5.3}$$

where volume element of  $\Gamma$  is  $dw = dx dy dz dt$ . These IEs are precisely the ones used to establish existence, uniqueness, and other properties of the discontinuous (weak) solutions of Maxwell's equations by Lewis [93], [96] as in Chapter 4. Higher discontinuities must satisfy these IEs for all testing functions  $\Omega$ . The discontinuity hypersurface may again be of any of the three types, that is, it may be the initial hyperplane  $t = 0$  when the source begin to act, or reflected/refracted hypersurface at a discontinuity in the medium, or a hypersurface arising from the source and separating zero/nonzero field region. Then discontinuity conditions for higher discontinuities become

$$\begin{aligned}
\nabla \phi \times \left[ \frac{\partial \mathbf{E}}{\partial t} \right] + \frac{\partial \phi}{\partial t} \mu \left[ \frac{\partial \mathbf{H}}{\partial t} \right] &= -\frac{\partial \phi}{\partial t} \nabla \times [\mathbf{E}]_{t=\psi/c} \\
\nabla \phi \times \left[ \frac{\partial \mathbf{H}}{\partial t} \right] - \frac{\partial \phi}{\partial t} \left( \varepsilon \left[ \frac{\partial \mathbf{E}}{\partial t} \right] + \left[ \frac{\partial \mathbf{F}}{\partial t} \right] \right) &= -\frac{\partial \phi}{\partial t} \nabla \times [\mathbf{H}]_{t=\psi/c} \\
\nabla \phi \times \left[ \frac{\partial^2 \mathbf{E}}{\partial t^2} \right] + \frac{\partial \phi}{\partial t} \mu \left[ \frac{\partial^2 \mathbf{H}}{\partial t^2} \right] &= -\frac{\partial \phi}{\partial t} \nabla \times \left[ \frac{\partial \mathbf{E}}{\partial t} \right]_{t=\psi/c} \\
\nabla \phi \times \left[ \frac{\partial^2 \mathbf{H}}{\partial t^2} \right] - \frac{\partial \phi}{\partial t} \left( \varepsilon \left[ \frac{\partial^2 \mathbf{E}}{\partial t^2} \right] + \left[ \frac{\partial^2 \mathbf{F}}{\partial t^2} \right] \right) &= -\frac{\partial \phi}{\partial t} \nabla \times \left[ \frac{\partial \mathbf{H}}{\partial t} \right]_{t=\psi/c} \\
&\vdots
\end{aligned} \tag{5.4}$$

Note that discontinuity conditions for higher order time derivatives are *nonhomogeneous* where as those for  $[\mathbf{E}]$ ,  $[\mathbf{H}]$  were homogeneous in Chapter 4. The fact seems surprising because  $\partial \mathbf{E}/\partial t$  and  $\partial \mathbf{H}/\partial t$  satisfy Maxwell's equations as do  $\mathbf{E}$ ,  $\mathbf{H}$ . The difference results from the behavior of the source. Our assumption rests on  $\mathbf{F}$  to be sectionally analytic with finite discontinuities.  $\partial \mathbf{E}/\partial t$  and  $\partial \mathbf{H}/\partial t$  satisfy Maxwell's equations with  $\partial \mathbf{F}/\partial t$  replaced by  $\partial^2 \mathbf{F}/\partial t^2$ . The discontinuities in  $\partial^2 \mathbf{F}/\partial t^2$  are of a higher order, and it is these discontinuities which propagate out along  $\phi = 0$ . For example, if  $\mathbf{F}$  is a step function  $u(t)$  (Heaviside) in the time behavior, then  $\partial \mathbf{F}/\partial t$  is an impulse  $\delta(t)$ , and  $\partial^2 \mathbf{F}/\partial t^2$  is a doublet  $\delta'(t)$ . These functions represent quite different physical sources in the sense of distributions. We must also repeat that the bracket symbol for a discontinuity means that the difference in the limits approached

by the enclosed quantity from either side of the discontinuity hypersurface. Then if  $\mathbf{F}$  is  $u(t)$  then  $[\mathbf{F}] = 1$  and  $[\partial\mathbf{F}/\partial t] = 0$ . Moreover this source function  $\mathbf{F}$  is discontinuous in  $(x,y,z)$ -space since the sources are confined to a bounded region. This implies discontinuous ICs. There are cases in which  $[\mathbf{E}]$ ,  $[\mathbf{H}]$  are zero on  $\phi=0$ , that is continuous, but some higher derivatives of  $\mathbf{E}$ ,  $\mathbf{H}$  may be discontinuous. Then the wave fronts are discontinuity hypersurfaces for these derivatives.  $\phi=0$  must still satisfy the characteristic condition and  $\Psi = ct$  must be wave fronts, and must satisfy Eiconal equation. As a result our approach is not altered even in these cases. Anyway proposed Taylor series is the expansion in the neighborhood of wave front in time but not in space. Another remark on Eqn(5.4) is that gradient operator applies only  $(x,y,z)$  before  $t$  is replaced by  $\Psi/c$ , but the curl operator applies to all  $(x,y,z)$  including  $t = \Psi(x,y,z)/c$ . The results up to here can be summarized by defining new vectors to be used in the rest of this chapter.

$$\begin{aligned}\mathbf{A}_\nu(x,y,z,t) &= \left[ \frac{\partial^\nu \mathbf{E}(x,y,z,t)}{\partial t^\nu} \right], \quad \mathbf{A}_{-1} = 0 \\ \mathbf{B}_\nu(x,y,z,t) &= \left[ \frac{\partial^\nu \mathbf{B}(x,y,z,t)}{\partial t^\nu} \right], \quad \mathbf{B}_{-1} = 0 \\ \mathbf{F}_\nu(x,y,z,t) &= \left[ \frac{\partial^\nu \mathbf{F}(x,y,z,t)}{\partial t^\nu} \right]\end{aligned}\tag{5.5}$$

Then at any point  $(x,y,z,t)$  on any hypersurface  $\phi=0$  where any one or more of the vectors  $\mathbf{A}_\nu$ ,  $\mathbf{B}_\nu$ ,  $\mathbf{F}_\nu$  may be discontinuous, they must satisfy the discontinuity conditions in Eqn(5.6) for  $\nu \geq 0$ . Recall that since  $\phi = \Psi - ct = 0$ , the  $t$  value in  $\mathbf{A}_{\nu-1}$  and  $\mathbf{B}_{\nu-1}$  must be replaced by  $\Psi/c$ .

$$\begin{aligned}\nabla\phi \times \mathbf{A}_\nu + \frac{\partial\phi}{\partial t} \mu \mathbf{B}_\nu &= -\frac{\partial\phi}{\partial t} \nabla \times \mathbf{A}_{\nu-1} \\ \nabla\phi \times \mathbf{B}_\nu - \frac{\partial\phi}{\partial t} (\varepsilon \mathbf{A}_\nu + \mathbf{F}_\nu) &= -\frac{\partial\phi}{\partial t} \nabla \times \mathbf{B}_{\nu-1}\end{aligned}\tag{5.6}$$

### 5.3 Propagation of Higher Discontinuities

In this section we will present 1<sup>st</sup> order ODEs for  $\mathbf{A}_\nu$ ,  $\mathbf{B}_\nu$  which express their variation along rays of  $(x,y,z)$ -space. Since we are interested in the case where  $\phi = \Psi - ct$ , discontinuity conditions, Eqn(5.6), become

$$\begin{aligned}\nabla\Psi \times \mathbf{A}_\nu(x,y,z,\Psi/c) - c\mu \mathbf{B}_\nu(x,y,z,\Psi/c) &= c\nabla \times \mathbf{A}_{\nu-1}(x,y,z,\Psi/c) \\ \nabla\Psi \times \mathbf{B}_\nu(x,y,z,\Psi/c) + c\varepsilon \mathbf{A}_\nu(x,y,z,\Psi/c) &= c\nabla \times \mathbf{B}_{\nu-1}(x,y,z,\Psi/c)\end{aligned}\tag{5.7}$$

Eqn(5.7) furnish six linear equations in the components of  $\mathbf{A}_\nu$ ,  $\mathbf{B}_\nu$ . However determinant of the coefficient matrix is zero because  $\Psi$  satisfies the Eiconal equation, and they do not determine  $\mathbf{A}_\nu$ ,  $\mathbf{B}_\nu$  uniquely. However we have assumed that we are dealing with a solution  $\mathbf{E}(x,y,z,t)$ ,  $\mathbf{H}(x,y,z,t)$  of Maxwell's equations whose discontinuities and the discontinuities of

the successive time derivatives of  $\mathbf{E}$ ,  $\mathbf{H}$  on a hypersurface  $\phi(x,y,z,t) = 0$  are finite jumps. Hence for any given  $v \geq 0$ , solutions  $\mathbf{A}_v$ ,  $\mathbf{B}_v$  of Eqn(5.7) do exist. Therefore Eqn(5.7) are consistent. Then the right hand terms of Eqn(5.7) must satisfy a consistency condition [92].

$$\begin{aligned}\mathbf{A}_0 \cdot \nabla \times \mathbf{B}_v - \mathbf{B}_0 \cdot \nabla \times \mathbf{A}_v &= 0 \\ \mu \mathbf{B}_0 \cdot \nabla \times \mathbf{B}_v + \varepsilon \mathbf{A}_0 \cdot \nabla \times \mathbf{A}_v &= 0\end{aligned}\quad (5.8)$$

These equations furnish the necessary conditions for the *nonhomogeneous* terms of Eqn(5.7) that must be satisfied. If we form the scalar product of Eqn(5.7) with  $\mathbf{p}$ , we have

$$\varepsilon \mathbf{p} \cdot \mathbf{A}_v = \mathbf{p} \cdot \nabla \times \mathbf{B}_{v-1} \quad , \quad \mu \mathbf{p} \cdot \mathbf{B}_v = -\mathbf{p} \cdot \nabla \times \mathbf{A}_{v-1} \quad (5.9)$$

From Eqn(5.7) and Eqn(5.9), one can conclude that

$$\mathbf{p} \cdot \mathbf{A}_v = \frac{c}{\varepsilon} \nabla \cdot (\varepsilon \mathbf{A}_{v-1}) \quad , \quad \mathbf{p} \cdot \mathbf{B}_v = \frac{c}{\mu} \nabla \cdot (\mu \mathbf{B}_{v-1}) \quad (5.10)$$

As a consequence of homogeneous algebraic equation for  $\mathbf{A}_0$ ,  $\mathbf{B}_0$ , they satisfy

$$\mathbf{p} \cdot \mathbf{A}_0 = \mathbf{p} \cdot \mathbf{B}_0 = 0 \quad (5.11)$$

saying that GO field is transverse to ray direction (wave normal  $\mathbf{p} = \nabla \Psi$ ), that is tangential to the wave front as expected. Using above equations and some vector algebra [92], transport equations for  $\mathbf{A}_v$ ,  $\mathbf{B}_v$  are found as:

$$\begin{aligned}2 \frac{d \mathbf{A}_v}{d \tau} + \mathbf{A}_v \cdot \Delta_\mu \Psi + \frac{2}{n} (\mathbf{A}_v \cdot \nabla n) \nabla \Psi &= -\mathbf{C}_v \\ 2 \frac{d \mathbf{B}_v}{d \tau} + \mathbf{B}_v \cdot \Delta_\varepsilon \Psi + \frac{2}{n} (\mathbf{B}_v \cdot \nabla n) \nabla \Psi &= -\mathbf{D}_v\end{aligned}\quad (5.12)$$

with the right hand source term being

$$\begin{aligned}\mathbf{C}_v &= \mu \nabla \times \left( \frac{c}{\mu} \nabla \times \mathbf{A}_{v-1} \right) - \nabla \cdot \left( \frac{c}{\varepsilon} \nabla \cdot (\varepsilon \mathbf{A}_{v-1}) \right) \\ \mathbf{D}_v &= \varepsilon \nabla \times \left( \frac{c}{\varepsilon} \nabla \times \mathbf{B}_{v-1} \right) - \nabla \cdot \left( \frac{c}{\mu} \nabla \cdot (\mu \mathbf{B}_{v-1}) \right)\end{aligned}\quad (5.13)$$

In homogeneous medium ( $\nabla n = 0$ ), then transport equations becomes a rather simple form.

$$2 \frac{d \mathbf{A}_v}{d \tau} + \mathbf{A}_v \cdot \nabla^2 \Psi = c \nabla^2 \mathbf{A}_{v-1} \quad , \quad 2 \frac{d \mathbf{B}_v}{d \tau} + \mathbf{B}_v \cdot \nabla^2 \Psi = c \nabla^2 \mathbf{B}_{v-1} \quad (5.14)$$

These vector ODEs give us the variation of  $\mathbf{A}_v$ ,  $\mathbf{B}_v$  along the rays which have the direction of  $\mathbf{p} = \nabla \Psi$  at any point. Also note that Eqn(5.12) is *recursive* via  $\mathbf{C}_v$ ,  $\mathbf{D}_v$  in Eqn(5.13). That is, we must solve first  $\mathbf{A}_0$ ,  $\mathbf{B}_0$  and use them as non-homogeneous terms in the equations for  $\mathbf{A}_1$ ,  $\mathbf{B}_1$  and so on.  $\mathbf{A}_0$ ,  $\mathbf{B}_0$  are the very quantities  $\mathbf{E}^*$  and  $\mathbf{H}^*$  which are GO fields of Chapter 4. If the equations of rays,  $x(\tau)$ ,  $y(\tau)$ ,  $z(\tau)$  are substituted for  $x, y, z$  in transport equations then these equations are linear, nonhomogeneous, 1<sup>st</sup> order ODEs in the independent variable  $\tau$  (time  $t$ ).

## 5.4 Solutions of Higher Transport Equations

Higher transport equations, or simply transport equations of Eqn(5.12) constitute two vector equations, each consisting of three coupled equations. In homogeneous media they become uncoupled. They may also be uncoupled for some special values of index of medium,  $n$ . The transport equations give the variation of  $\mathbf{A}_\nu$ ,  $\mathbf{B}_\nu$  along the rays which belong to a particular source and along the rays which may result from reflection and refraction at a discontinuity in the medium. To proceed with the solution we make use of the equations

$$\Delta_\mu \Psi = n^2 \nabla \cdot \mathbf{s} + \frac{1}{\varepsilon} \frac{d\varepsilon}{d\tau}, \quad \Delta_\varepsilon \Psi = n^2 \nabla \cdot \mathbf{s} + \frac{1}{\mu} \frac{d\mu}{d\tau} \quad (5.15)$$

Recall that  $\mathbf{s} \cdot \mathbf{p} = 1$ . Just as in Chapter 4, transport equations get the form of

$$\begin{aligned} \frac{d(\sqrt{\varepsilon} \mathbf{A}_\nu)}{d\tau} + \frac{1}{2} n^2 \nabla \cdot \mathbf{s} (\sqrt{\varepsilon} \mathbf{A}_\nu) + \frac{\nabla n \cdot (\sqrt{\varepsilon} \mathbf{A}_\nu)}{n} \mathbf{p} &= -\frac{\sqrt{\varepsilon} \mathbf{C}_\nu}{2} \\ \frac{d(\sqrt{\mu} \mathbf{B}_\nu)}{d\tau} + \frac{1}{2} n^2 \nabla \cdot \mathbf{s} (\sqrt{\mu} \mathbf{B}_\nu) + \frac{\nabla n \cdot (\sqrt{\mu} \mathbf{B}_\nu)}{n} \mathbf{p} &= -\frac{\sqrt{\mu} \mathbf{D}_\nu}{2} \end{aligned} \quad (5.16)$$

We now set

$$\sqrt{\varepsilon} \mathbf{A}_\nu = \sqrt{W_\nu} \mathbf{P}_\nu, \quad \sqrt{\mu} \mathbf{B}_\nu = \sqrt{W_\nu} \mathbf{Q}_\nu \quad (5.17)$$

Scalar  $W_\nu$  and vectors  $\mathbf{P}_\nu$ ,  $\mathbf{Q}_\nu$  are to be determined. Previously we showed that  $\mathbf{P}_0$ ,  $\mathbf{Q}_0$  are unit vectors (they are  $\mathbf{P}$ ,  $\mathbf{Q}$  of Chapter 4) and energy  $W_\nu$  of  $\nu^{\text{th}}$  discontinuity satisfies

$$\frac{W_\nu(\tau)}{n(\tau)K(\tau)} = \frac{W_\nu(\tau_0)}{n(\tau_0)K(\tau_0)} \quad (5.18)$$

where the ratio of  $K(\tau_0)$  to  $K(\tau)$  gives the relative expansion of the cross sectional area of a tube of rays and  $n(\tau_0)$ ,  $K(\tau_0)$  values of  $n(\tau)$ ,  $K(\tau)$  at some initial point on the ray  $x(\tau)$ ,  $y(\tau)$ ,  $z(\tau)$ . Then Eqn(5.16) transforms into

$$\begin{aligned} \frac{d\mathbf{P}_\nu}{d\tau} + \frac{(\mathbf{P}_\nu \cdot \nabla n)}{n} \mathbf{p} &= -\frac{1}{2} \frac{\sqrt{\varepsilon}}{\sqrt{W_\nu}} \mathbf{C}_\nu \\ \frac{d\mathbf{Q}_\nu}{d\tau} + \frac{(\mathbf{Q}_\nu \cdot \nabla n)}{n} \mathbf{p} &= -\frac{1}{2} \frac{\sqrt{\varepsilon}}{\sqrt{W_\nu}} \mathbf{D}_\nu \end{aligned} \quad (5.19)$$

Since  $\mathbf{P}_0$ ,  $\mathbf{Q}_0$  are unit vectors and transverse to rays, we also make  $\mathbf{p} = \nabla \Psi$  a unit vector dividing it by  $n$  in order to have orthogonal unit triple vector set  $(\hat{\mathbf{P}}_0, \hat{\mathbf{Q}}_0, \hat{\mathbf{p}})$ . Then, as the solutions of Eqn(5.19), components of  $\mathbf{P}_\nu$ ,  $\mathbf{Q}_\nu$  are given by Eqn(5.20). Below formulas presuppose that  $\mathbf{P}_0$ ,  $\mathbf{Q}_0$  are known from Chapter 3 for  $\nu = 0$ .

$$\begin{aligned}
\mathbf{P}_\nu \cdot \hat{\mathbf{p}} &= -\frac{1}{2} \int_{\tau_0}^{\tau} \frac{\sqrt{\varepsilon}}{\sqrt{W_\nu}} (\hat{\mathbf{p}} \cdot \mathbf{C}_\nu) d\tau + (\mathbf{P}_\nu \cdot \hat{\mathbf{p}}) \Big|_{\tau_0} \\
\mathbf{P}_\nu \cdot \hat{\mathbf{P}}_0 &= -\int_{\tau_0}^{\tau} \hat{\mathbf{P}}_0 \cdot \left( \frac{1}{2} \frac{\sqrt{\varepsilon}}{\sqrt{W_\nu}} \mathbf{C}_\nu + (\mathbf{P}_\nu \cdot \hat{\mathbf{p}}) \nabla \mathbf{n} \right) d\tau + (\mathbf{P}_\nu \cdot \hat{\mathbf{P}}_0) \Big|_{\tau_0} \\
\mathbf{P}_\nu \cdot \hat{\mathbf{Q}}_0 &= -\int_{\tau_0}^{\tau} \hat{\mathbf{Q}}_0 \cdot \left( \frac{1}{2} \frac{\sqrt{\varepsilon}}{\sqrt{W_\nu}} \mathbf{C}_\nu + (\mathbf{P}_\nu \cdot \hat{\mathbf{p}}) \nabla \mathbf{n} \right) d\tau + (\mathbf{P}_\nu \cdot \hat{\mathbf{Q}}_0) \Big|_{\tau_0} \\
\mathbf{Q}_\nu \cdot \hat{\mathbf{p}} &= -\frac{1}{2} \int_{\tau_0}^{\tau} \frac{\sqrt{\varepsilon}}{\sqrt{W_\nu}} (\hat{\mathbf{p}} \cdot \mathbf{D}_\nu) d\tau + (\mathbf{Q}_\nu \cdot \hat{\mathbf{p}}) \Big|_{\tau_0} \\
\mathbf{Q}_\nu \cdot \hat{\mathbf{P}}_0 &= -\int_{\tau_0}^{\tau} \hat{\mathbf{P}}_0 \cdot \left( \frac{1}{2} \frac{\sqrt{\varepsilon}}{\sqrt{W_\nu}} \mathbf{D}_\nu + (\mathbf{Q}_\nu \cdot \hat{\mathbf{p}}) \nabla \mathbf{n} \right) d\tau + (\mathbf{Q}_\nu \cdot \hat{\mathbf{P}}_0) \Big|_{\tau_0} \\
\mathbf{Q}_\nu \cdot \hat{\mathbf{Q}}_0 &= -\int_{\tau_0}^{\tau} \hat{\mathbf{Q}}_0 \cdot \left( \frac{1}{2} \frac{\sqrt{\varepsilon}}{\sqrt{W_\nu}} \mathbf{D}_\nu + (\mathbf{Q}_\nu \cdot \hat{\mathbf{p}}) \nabla \mathbf{n} \right) d\tau + (\mathbf{Q}_\nu \cdot \hat{\mathbf{Q}}_0) \Big|_{\tau_0}
\end{aligned} \tag{5.20}$$

These solutions are valid along hypersurface  $\phi(x,y,z,t) = 0$  or the trajectories to  $\Psi = ct$  as long as  $\varepsilon, \mu, \sigma$  are smooth. Across a discontinuity in  $\varepsilon, \mu, \sigma$ , Fresnel formulas must be applied and variation of  $\mathbf{P}_\nu, \mathbf{Q}_\nu$  must be obtained along new rays which may arise from reflection or refraction. One other point should be noted in applying the series formulas that give  $\mathbf{P}_\nu, \mathbf{Q}_\nu$ . In each of these, the quantities  $\mathbf{C}_\nu, \mathbf{D}_\nu$  occurs. They in turn depend on  $\mathbf{A}_{\nu-1}, \mathbf{B}_{\nu-1}$ , that is, *recursive* nature of transport equations. However when  $\mathbf{A}_{\nu-1}, \mathbf{B}_{\nu-1}$  are determined from solutions for the case  $\nu-1$ ,  $\mathbf{C}_\nu, \mathbf{D}_\nu$  are determined as function of  $\tau$  or  $(x,y,z)$ .

### 5.5 Initial Values for Transport Equations

Transport equations hold along the rays provided that medium parameters are continuous. When a discontinuity in the medium occurs, a new family of wave fronts and rays arise. Therefore the transport equations must be solved along these new rays. Moreover, source begins to act at  $t = 0$  creating discontinuous ICs. Hence, we need ICs at source side and at medium discontinuity. ICs are the initial values of  $\mathbf{A}_\nu, \mathbf{B}_\nu$  for Eqn(5.12). From them, ICs for  $\mathbf{P}_\nu, \mathbf{Q}_\nu, W_\nu$  for Eqns(5.19),(5.20) can also be determined using Eqns(5.17),(5.18).

For this purposes, it is convenient to treat the ICs by considering relevant discontinuity hypersurfaces from which rays stem. The first one is the discontinuity hypersurface of the source. As we stated earlier, source charges are located in a bounded domain of  $(x,y,z)$ -space surrounding the origin where  $S$  is the source boundary as in Figure 5-3.

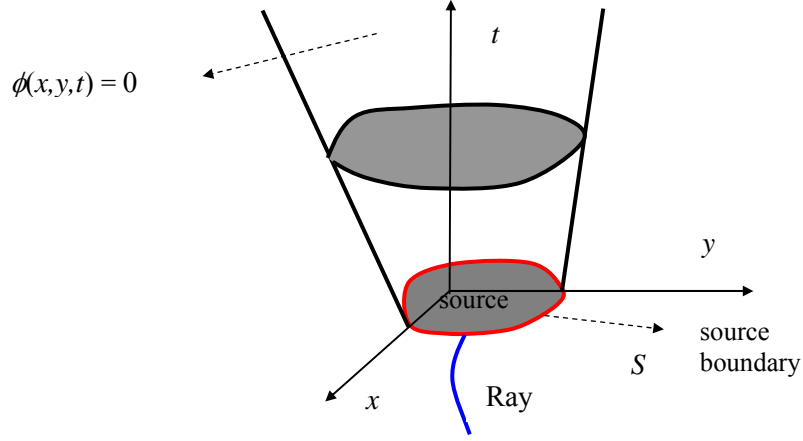


Figure 5-3: Determination of ICs at source boundary

The distribution of these charges is specified by  $\mathbf{F}(x,y,z,t)$  for  $t \geq 0$ . Recall that  $\mathbf{F}$  is smooth and discontinuities in  $\mathbf{F}$  and in all its successive derivatives are *finite*. So it is clear that discontinuity hypersurface in  $(x,y,z,t)$ -space at  $t = 0$  starts at the boundary  $S$  in  $(x,y,z)$ -space. ICs for  $\mathbf{A}_\nu$ ,  $\mathbf{B}_\nu$  are their values  $t = 0$  and at those points  $(x,y,z)$  which lie on  $S$ . These ICs for  $\nu = 0$  has been found to be in Chapter 4 as:

$$\begin{aligned} \mathbf{A}_0(x,y,z,0) &= \mathbf{E}^* = [\mathbf{E}(x,y,z,0)] = -[\mathbf{F}(x,y,z,0)]/\varepsilon \\ \mathbf{B}_0(x,y,z,0) &= \mathbf{H}^* = [\mathbf{H}(x,y,z,0)] = 0 \end{aligned} \quad (5.21)$$

These are the jumps in  $\mathbf{E}$ ,  $\mathbf{H}$  at initial points of discontinuity hypersurface and are the same as the initial points of rays stemming from  $S$ . Then  $S$  can be interpreted as generator of wave fronts  $\Psi = ct$  belonging to these rays. For  $\nu = 1$ , discontinuity conditions Eqn(5.6) become

$$\begin{aligned} \varepsilon \left[ \frac{\partial \mathbf{E}(x,y,z,0)}{\partial t} \right] + \left[ \frac{\partial \mathbf{F}(x,y,z,0)}{\partial t} \right] &= \nabla \times [\mathbf{H}(x,y,z,0)] \\ \mu \left[ \frac{\partial \mathbf{H}(x,y,z,0)}{\partial t} \right] &= -\nabla \times [\mathbf{E}(x,y,z,0)] \end{aligned} \quad (5.22)$$

Note that since we are dealing with  $\phi \equiv t = 0$  then  $\partial \phi / \partial t = 1$  and  $\nabla \times \phi = 0$ .  $\mathbf{E}$ ,  $\mathbf{H}$ ,  $\mathbf{F}$  are analytic within the discontinuity hypersurface, then using results of Eqn(5.21) in right hand terms of Eqn(5.22), ICs for  $\nu = 1$  are found to be

$$\begin{aligned} \mathbf{A}_1(x,y,z,0) &= \left[ \frac{\partial \mathbf{E}(x,y,z,0)}{\partial t} \right] = -\frac{1}{\varepsilon} \left[ \frac{\partial \mathbf{F}(x,y,z,0)}{\partial t} \right] \\ \mathbf{B}_1(x,y,z,0) &= \left[ \frac{\partial \mathbf{H}(x,y,z,0)}{\partial t} \right] = \frac{1}{\mu} \nabla \times ([\mathbf{F}(x,y,z,0)]/\varepsilon) \end{aligned} \quad (5.23)$$

In above expressions we can omit brackets because fields are zero for  $t < 0$ . This process to obtain the ICs can be continued so on. Rather than the sources, if we are given a pulse field

in the neighborhood of a discontinuity hypersurface, then we may use the field vectors and their successive time derivatives evaluated at the discontinuity surface to determine the ICs of the transport equations. We will adopt this way for simulations in Chapter 6.

The second case is the determination of ICs for the rays arising from reflection and refraction at a fixed discontinuity surface  $\phi = \Psi_0(x,y,z) = 0$ . ICs for transport equations along reflected and refracted rays can in principle be handled, though no neat formulas can be presented for  $\mathbf{A}_\nu, \mathbf{B}_\nu$  beyond  $\nu = 0$ . The case  $\nu = 0$  has actually been treated in Chapter 4 and Fresnel formulas obtained has shown the ICs of the reflected and refracted fields in terms of incident field impinging on the refracting surface. The ICs of  $\mathbf{A}_1, \mathbf{B}_1$  for the reflected and refracted fields can also be obtained by the same method, but the results can not be presented as compact as Fresnel formulas. The complexity comes from discontinuity condition for  $\nu = 1$  which has nonzero right hand terms. The values of the right-hand members for  $\nu = 1$  are known from the case  $\nu = 0$ . The condition Eqn(4.50) remain the same for time derivatives of  $\mathbf{E}, \mathbf{H}$  because our more general conditions Eqn(5.6) applied to a fixed discontinuity surface  $\phi = \Psi_0(x,y,z) = 0$  show that tangential components of  $\mathbf{A}_\nu, \mathbf{B}_\nu$  are zero. But the method of calculating the ICs of  $\mathbf{A}_1, \mathbf{B}_1$  would be as follows. We see from Eqn(5.9) that the components of  $\mathbf{A}_1, \mathbf{B}_1$  along  $\mathbf{p}$  are given in terms of  $\nabla \times \mathbf{A}_0, \nabla \times \mathbf{B}_0$  respectively. Anyway they have to be calculated in any case to solve the transport equations for  $\mathbf{A}_1, \mathbf{B}_1$ . Hence when we find the values  $\mathbf{A}_0, \mathbf{B}_0$  we can calculate  $\nabla \times \mathbf{A}_0, \nabla \times \mathbf{B}_0$ . This remark applies to both the reflected and refracted fields. Thus we know the components of  $\mathbf{A}_1, \mathbf{B}_1$  along the ray. We may therefore consider the components of  $\mathbf{A}_1, \mathbf{B}_1$  which are normal to  $\mathbf{p}$ . Whether incident, reflected, or refracted, we can write

$$\sqrt{\varepsilon} \mathbf{A}_{1n} = \alpha \hat{\mathbf{N}} + \beta \hat{\mathbf{S}} \quad (5.24)$$

$\hat{\mathbf{S}}$  and  $\hat{\mathbf{N}}$  have the same meanings in Chapter 4. Using Eqn(5.7) for  $\nu = 1$  we first write

$$\frac{\mathbf{p}}{n} \times \mathbf{B}_1 + \frac{c\varepsilon}{n} \mathbf{A}_{1n} + \left( \frac{c\varepsilon \mathbf{p} \cdot \mathbf{A}_1}{n^2} \right) \frac{\mathbf{p}}{n} = \frac{c}{n} \nabla \times \mathbf{B}_0 \quad (5.25)$$

Substituting Eqn(5.24) into Eqn(5.25) and using Eqn(5.9) we have

$$\frac{\mathbf{p}}{n} \times \mathbf{B}_1 + \frac{\alpha c \sqrt{\varepsilon}}{n} \hat{\mathbf{N}} + \frac{\beta c \sqrt{\varepsilon}}{n} \hat{\mathbf{S}} + \frac{c}{n} \left( \frac{\mathbf{p}}{n} \cdot \nabla \times \mathbf{B}_0 \right) \frac{\mathbf{p}}{n} = \frac{c}{n} \nabla \times \mathbf{B}_0 \quad (5.26)$$

Note that the first term in left-hand side of Eqn(5.26) is the component of  $\mathbf{B}_1$  normal to  $\mathbf{p}/n$ . As a result we have

$$\mathbf{B}_{1n} = -\frac{\alpha c \sqrt{\varepsilon}}{n} \hat{\mathbf{N}} - \frac{\beta c \sqrt{\varepsilon}}{n} \hat{\mathbf{S}} - \frac{c}{n} \left( \left( \frac{\mathbf{p}}{n} \cdot \nabla \times \mathbf{B}_0 \right) \frac{\mathbf{p}}{n} - \nabla \times \mathbf{B}_0 \right) \quad (5.27)$$

We see that  $\mathbf{B}_{1n}$  is similarly expressed in terms of two parameters  $\alpha, \beta$ . Other quantities are known. Following the same steps for obtaining Fresnel formulas, It can be found four scalar equations for  $\alpha^r, \beta^r, \alpha^t, \beta^t$  but more complicated equations than that of Chapter 4.

### 5.6 Reconstruction of Time-Dependent Electromagnetic Fields

Transport equations give the behavior of the finite discontinuities of  $\mathbf{E}, \mathbf{H}$  fields, i.e.,  $[\mathbf{E}], [\mathbf{H}], [\partial\mathbf{E}/\partial t], [\partial\mathbf{H}/\partial t]$ ...etc along rays. In terms of  $(x,y,z)$ -space, each family of curves is a family of rays associated with a family of wave fronts (arising from source, reflection and refraction) The solution to transport equations gives the discontinuity at any  $(x,y,z)$  but only at that  $t$ -value at which the wave front of the family of rays passes through  $(x,y,z)$ .  $[\mathbf{E}], [\mathbf{H}]$  themselves furnish GO field. Higher discontinuities have no immediate physical meaning. But they may be regarded as improvement over GO. Direct accomplishment of this Chapter is that approximate representation of pulse solutions of  $\mathbf{E}(x,y,z,t), \mathbf{H}(x,y,z,t)$  by means of Taylor's series is possible. The series must be distinguished on the basis of the nature of the discontinuity hypersurface in question at  $\mathbf{E}, \mathbf{H}$  are discontinuous.

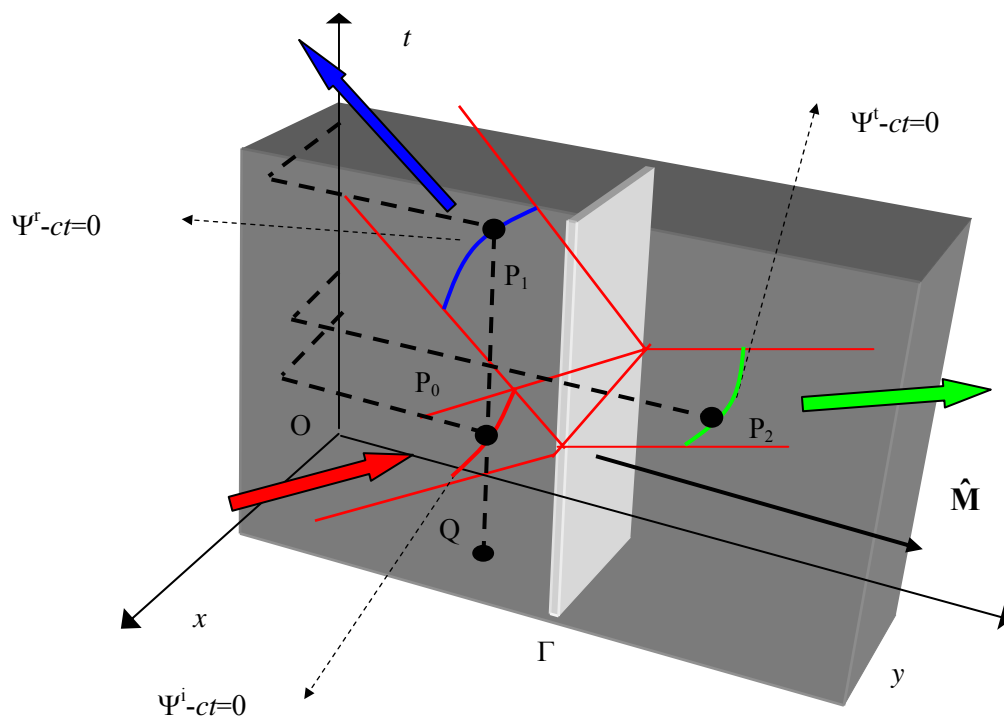


Figure 5-4: Construction of Taylor series.

Consider the point  $P_0$  or  $(x_0, y_0, z_0, t_0)$  in Figure 5-4 through which discontinuity hypersurface emanating from the source (e.g.,  $\Psi(x, y, z) - ct = 0$ ) passes. Since  $\mathbf{E}$ ,  $\mathbf{H}$  are zero for  $t < t_0$ , the values of  $\mathbf{E}$ ,  $\mathbf{H}$  and their successive time derivatives at  $t = t_{0+}$ , that is, the values obtained by approaching  $t_0$  from  $t > t_0$ , are the discontinuities at  $t = t_0$ . Hence in the neighborhood of  $t = t_0$  for  $t > t_0$  we have

$$\begin{aligned} \mathbf{E}^i(x_0, y_0, z_0, t) = & [\mathbf{E}(x_0, y_0, z_0, t_0)] + \left[ \frac{\partial \mathbf{E}(x_0, y_0, z_0, t_0)}{\partial t} \right] (t - t_0) \\ & + \left[ \frac{\partial^2 \mathbf{E}(x_0, y_0, z_0, t_0)}{\partial t^2} \right] \frac{(t - t_0)^2}{2} + \dots \end{aligned} \quad (5.28)$$

where  $t_0 = \Psi(x_0, y_0, z_0)/c$ . And the coefficients in this series are the discontinuities in  $\mathbf{E}$  and its successive time derivatives. They can be determined by the solutions of the transport equations for  $\mathbf{A}_0, \mathbf{A}_1, \mathbf{A}_2, \dots$ . The solutions are being fixed by the ICs furnished by the source.

However for the same  $(x_0, y_0, z_0)$  there may be a  $t_1$  such that  $\phi^r(x_0, y_0, z_0, t_1) = \Psi^r(x_0, y_0, z_0) - ct_1 = 0$  which is a reflected hypersurface. The expansion Eqn(5.28) for  $\mathbf{E}(x, y, z, t)$  in the neighborhood of  $t = t_0$  still holds for  $t > t_1$  but it represents incident field for  $t > t_1$ . However we may consider new expansions at  $(x_0, y_0, z_0)$  in the neighborhood of  $t = t_1$  (point  $P_1$ ). Two expansions are possible, one holding in the domain  $t < t_1$  and the other  $t > t_1$ . The coefficient in the first one will be the values of  $\mathbf{E}$  and its successive derivatives at  $(x_0, y_0, z_0, t_1)$  when this point is approached through  $t < t_1$ . This expansion may be valid for  $t > t_1$  also because the incident field alone may be analytic for these values of  $t$ . But this expansion represents only the incident field for  $t > t_1$ . The coefficients in the second one will be the values of  $\mathbf{E}$  and its successive time derivatives at  $(x_0, y_0, z_0, t_1)$  when  $P_1$  is approached through  $t > t_1$ . These values belong to the sum of the incident and reflected fields. However we do not have the values of  $\mathbf{E}$  in this neighborhood because these values should come from the knowledge of the exact solution of problem. But the exact  $\mathbf{E}$  are discontinuous on  $\phi^r(x_0, y_0, z_0, t_1) = 0$  and the discontinuities of  $\mathbf{E}$  and its successive time derivatives on  $\phi^r(x_0, y_0, z_0, t_1) = 0$  are the jumps in their values which result from the fact that a reflected field exist above  $\phi^r = 0$ , that is, for  $t > t_1$ . Hence for the reflected field only we have the following expansion.

$$\begin{aligned} \mathbf{E}^r(x_0, y_0, z_0, t) = & [\mathbf{E}(x_0, y_0, z_0, t_1)] + \left[ \frac{\partial \mathbf{E}(x_0, y_0, z_0, t_1)}{\partial t} \right] (t - t_1) \\ & + \left[ \frac{\partial^2 \mathbf{E}(x_0, y_0, z_0, t_1)}{\partial t^2} \right] \frac{(t - t_1)^2}{2} + \dots \end{aligned} \quad (5.29)$$

This expansion is significant in the neighborhood of  $\phi^r = 0$  because the first term is reflected GO field and coefficients in this expansion are the discontinuities of  $\mathbf{E}$  and its successive time derivatives on  $\phi^r = 0$  which propagate along the reflected rays and are determined by

the study of transport equations. They can be found by solving the transport equations along the  $\phi = 0$  or  $t = \Psi^i(x_0, y_0, z_0)/c$  and by fixing the solutions uniquely with the ICs for the reflected field obtained from Fresnel formulas and their extensions to higher discontinuities  $\mathbf{A}_1, \mathbf{A}_2, \dots$ . Then the total field  $\mathbf{E}(x, y, z, t)$  for  $t > t_1$  can be obtained by the sum of Eqns(5.28), (5.29) as long as Eqn(5.28) holds for  $t > t_1$ .

$$\mathbf{E}(x_0, y_0, z_0, t) = \mathbf{E}^i(x_0, y_0, z_0, t) + \mathbf{E}^r(x_0, y_0, z_0, t) \quad (5.30)$$

As for the series expansion in the neighborhood of the point  $P_2, (x_2, y_2, z_2, t_2)$ . There is no incident field below the refracted hypersurface  $\phi(x, y, z, t) = 0$ . Hence the values of  $\mathbf{E}$  and its successive time derivatives on  $\phi = 0$  (the values approached through  $t > t_2$ ). Then the expansion in the neighborhood of  $(x_2, y_2, z_2, t_2)$  will have these values as series coefficients. They can be found from Fresnel formulas and their extensions to higher discontinuities for refracted field. Then refracted field will be expressed as

$$\begin{aligned} \mathbf{E}^t(x_2, y_2, z_2, t) = & [\mathbf{E}(x_2, y_2, z_2, t_2)] + \left[ \frac{\partial \mathbf{E}(x_2, y_2, z_2, t_2)}{\partial t} \right] (t - t_2) \\ & + \left[ \frac{\partial^2 \mathbf{E}(x_2, y_2, z_2, t_2)}{\partial t^2} \right] \frac{(t - t_2)^2}{2} + \dots \end{aligned} \quad (5.31)$$

The preceding discussion can also be put in other words in  $(x, y, z)$ -space. At a point  $(x, y, z)$ , Eqn(5.28) gives the incident field from the instant  $t_0$  at which the incident wave front family  $\Psi^i(x, y, z) = ct$  passes  $(x, y, z)$ . Solutions of the transport equations along the rays belonging to this wave front family provide the coefficients of series expansion Eqn(5.28). At some later time  $t_1$ , reflected wave front family  $\Psi^r(x, y, z) = ct$  passes through  $(x, y, z)$ . The series expansion Eqn(5.29) gives the reflected field for  $t > t_1$ . The coefficients of this series are calculated by solving the transport equations along the rays of reflected wave front family. The total field at  $(x, y, z)$  for  $t > t_1 > t_0$  is the sum of these two series expansion if both series are still convergent for the value of  $t$ . Similar remarks apply to refracted field also.

The existence of Taylor's series in the neighborhood of points on the incident discontinuity hypersurface as well as on reflected and refracted discontinuity hypersurfaces presupposes, first of all, that the discontinuities in  $\mathbf{E}$  and its successive time derivatives are *finite*. Infinite discontinuities (coefficients of Taylor series) occur for caustics and diffracted fields, then series expansion break down and does not converge. Secondly we are supposing that Taylor's series (up to  $n$ -terms with remainder) can represent  $\mathbf{E}$  in some region of  $t$ -values, that is, we can build Taylor's expansion up to  $n$ -terms if  $\mathbf{E}$  is differentiable upto the  $(n+1)^{\text{th}}$  order. The existence and uniqueness of a solution of Maxwell's equations are also assumed for the given problem. We are using Taylor's series representing  $\mathbf{E}$  only on one side of the

point which the expansion is formed. The existence of the value of a function and its successive derivatives on one side only is sufficient to determine Taylor's series [97]. The resulting series will represent an analytic function on both sides of the point under investigation, but only the values on one side may represent the true solution in which we are interested.

In this chapter, we have mainly dealt with higher order discontinuities beyond the GO term to find or approximate full time dependent solutions of Maxwell's equations. Similar to TDGO, this method can be called as *Time Domain Ray Optics (TDRO)*. We can call TDGO and TDRO together as *Ray Based Time Domain (RBTDM)* method. In the next chapter, we will present applications of RBTDM method for several electromagnetic problems. Note that, different than time domain finite methods (FDTD, FETD, FVTD), RBTDM deals with only one of the field quantities, either **E** or **H**.

## CHAPTER 6

### NUMERICAL STUDIES

#### 6.1 Introduction

In Chapter 3, we have reviewed frequency and time-domain methods for CEM with emphasis on time domain finite methods, especially FDTD, FVTD and characteristic-based methods. Chapters 4 and 5 discussed the theoretical basis of Ray Based Time Domain method (RBTD) namely, hypersurfaces, discontinuities, wave fronts, rays, transport equations and Taylor series. RBTD is considered to replace FDTD and characteristic-based methods eliminating their deficiencies but not bringing new drawbacks. We must prove this statement. It is clear that diagonalisation of coefficient matrix of characteristic-based methods has been removed by RBTD since it has nothing to do with coefficient matrix and its diagonalisation. The method of RBTD is completely different than characteristic-based methods. However RBTD itself by nature is a characteristic method since it utilizes characteristics and bicharacteristics curves (wave fronts, rays) of Maxwell's PDE. Hence RBTD retains all the advantages of characteristic-based methods such as well-posedness, stability, dispersion, ABCs implementation and directional signal propagation. It is also claimed that RBTD eliminates numerical dispersion inherent to FDTD which depends on discretization of PDE (grid resolution, time step) and propagation direction. Making use of special grid structure (wave fronts and rays) and ODEs transport equations, RBTD gets rid of numerical dispersion too. We verify all these statements with several simulations of EM problems and comparing the results. Simulations have been adapted from [105].

#### 6.2 Sample Problem I: 1-D Propagating Plane Wave

##### 6.2.1 Computational Grid

For FDTD implementation in free space ( $\epsilon_0, \mu_0$ ),  $E_x$ ,  $H_y$  fields propagating in  $\pm z$  directions are oriented in the computational grid as in Figure 6-1. RBTD requires grid to be wave fronts and rays. In this problem, computational grid is same for both FDTD and RBTD due to homogeneous medium and source condition. Field is defined on the initial plane wave front as input. Wave fronts,  $\Psi$ , are  $\Psi(x,y,z) = z = j\Delta z = \text{constant}$  plane surfaces. They also satisfy our definition of  $\Psi = ct$ . Then rays are straight lines normal to these  $\Psi$ s.

Figure 6-1 illustrates wave fronts and rays. Note that every grid point along  $z$ -axis ( $z = j\Delta z$ ) has its associated time reference ( $t = t_j = \Psi(j\Delta z)/c$ ). Due to finite velocity of propagation, no wave can exist at that point for  $t < t_j$ . At  $t = t_j$ , only GO field can exist, and after  $t > t_j$ , total time-dependent field exists.

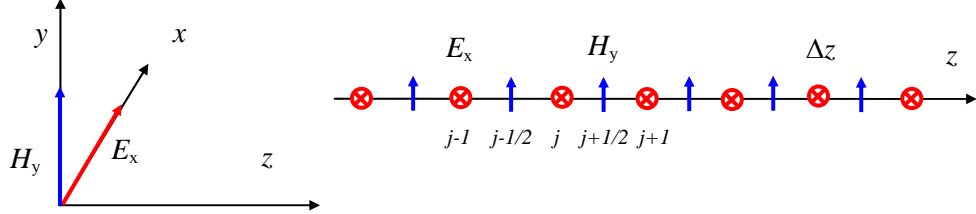


Figure 6-1: 1-D plane wave and computational grid

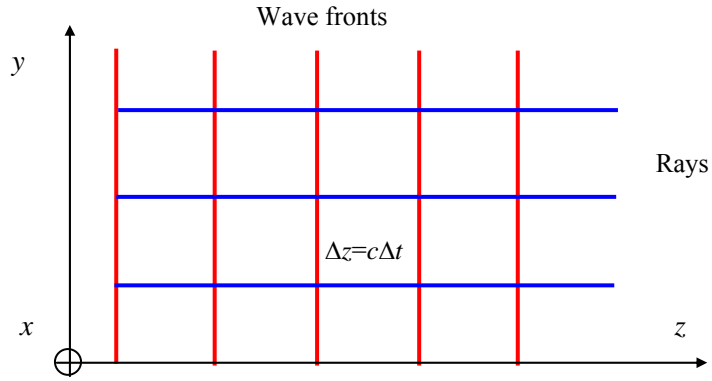


Figure 6-2: Wave fronts and rays for RBTD

### 6.2.2 FDTD Implementation

Consider a simple 1-D transverse electromagnetic (TEM) plane wave (PW) propagating in  $\pm z$  directions. For this case, Maxwell's equations, in source free region, reduce to:

$$\frac{\partial E_x}{\partial t} = -\frac{1}{\epsilon_0} \frac{\partial H_y}{\partial z}, \quad \frac{\partial H_y}{\partial t} = -\frac{1}{\mu_0} \frac{\partial E_x}{\partial z} \quad (6.1)$$

Eqn(6.1) also leads to 2<sup>nd</sup> order 1-D wave equation of

$$\frac{\partial^2 E_x}{\partial z^2} - \frac{1}{c^2} \frac{\partial^2 E_x}{\partial t^2} = 0 \quad (6.2)$$

whose solution is sum of right and left propagating waves as in Eqn(2.20). A hard source excitation on the initial wave front which is a plane surface ( $z = z_c = 0$ ) is enforced, that is,

$$E_x(z_c, t) = f(t) \quad (6.3)$$

$f(t)$  can be any function such as rectangular, Gaussian or sinusoidal excitation. With the understanding of  $z = j\Delta z$ ,  $t = n\Delta t$ , then discretization of Eqn(6.1) yields the following explicit time update equations for field quantities.

$$\begin{aligned} E_x^{n+1/2}(j) &= E_x^{n-1/2}(j) - \frac{\Delta t}{\epsilon_0 \Delta z} (H_y^n(j+1/2) - H_y^n(j-1/2)) \\ H_y^{n+1}(j+1/2) &= H_y^n(j+1/2) - \frac{\Delta t}{\mu_0 \Delta z} (E_x^{n+1/2}(j+1) - E_x^{n-1/2}(j)) \end{aligned} \quad (6.4)$$

Let the highest frequency of  $f(t)$  that would propagate in the grid be  $f_{\max} = 1\text{GHz}$ . Then the minimum wavelength to be observed in the medium is  $\lambda_{\min} = c/f_{\max} = 30\text{cm}$ . The grid spacing ( $\Delta z$ ) along  $z$  must be at least to satisfy Nyquist sampling, that is,  $\Delta z \geq \lambda_{\min}/2$ . And time step  $\Delta t$  is selected to satisfy stability of numerical algorithm in accordance with CFL stability condition, for 1-D case, which is  $\Delta t \leq \Delta z/c$ . CFL number is defined to be  $\text{CFL} = c\Delta t/\Delta z$ . Then according to the choice of CFL number, time step  $\Delta t$  becomes  $\Delta t = \text{CFL}(\Delta z/c)$ . Throughout the simulations for Sample Problem I and II, following grid structures are worked out for the analysis and interpretation of results (Table 6-1).

Table 6-1: Coarse and fine grid for Sample Problem I and II

	<b>Coarse grid</b>	<b>Fine Grid</b>
Grid spacing ( $\Delta z$ )	$\lambda_{\min}/5$	$\lambda_{\min}/10$

### 6.2.2.1 Rectangular Pulse

Let the excitation be  $f(t) = \text{rect}(t/T)$  whose pulse width is  $T = 10\text{nsec}$  (Figure 6-3). Fourier transform of  $f(t)$  has  $\text{sinc}(\omega T)$  behavior whose  $1/T$  main bandwidth is  $100\text{MHz}$ . Then our assumption of  $f_{\max} = 1\text{GHz}$  is good enough that it is  $40\text{dB}$  below the peak of power spectra.

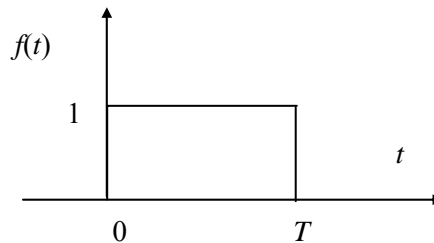


Figure 6-3: Rectangular pulse

**Coarse Grid** ( $\Delta z = \lambda_{\min}/5$ ): Presented results below are the values of  $E_x$  in the computational grid at the end of the observation time. The observation time is  $450\Delta t$  for CFL = 1,  $900\Delta t$  for CFL = 0.5 and  $445\Delta t$  for CFL = 0.99. In Chapter 3, we stated that numerical solution of FDTD for 1-D wave equation is exact analytical solution for the case of CFL = 1 (magic time step). Our simulation verifies that FDTD yields exact analytical solution for CFL = 1 no matter how long the numerical analogue of wave propagates. FDTD and analytic results overlap in Figure 6-4. As for the case of CFL = 0.5 and CFL = 0.99, Figure 6-5, Figure 6-6 show that FDTD computed wave is prone to numerical dispersion as expected and numerical dispersion error is more pronounced as it propagates longer distances. Changing CFL number from 0.5 to 0.99 causes increase in the oscillation frequency of ripples but peak distortion does not change (similar to Gibbs phenomena).

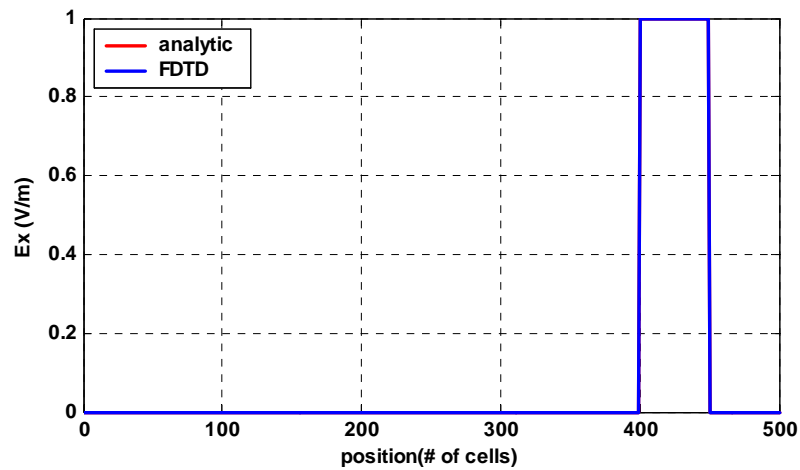


Figure 6-4: FDTD rectangular pulse propagation (CFL = 1)

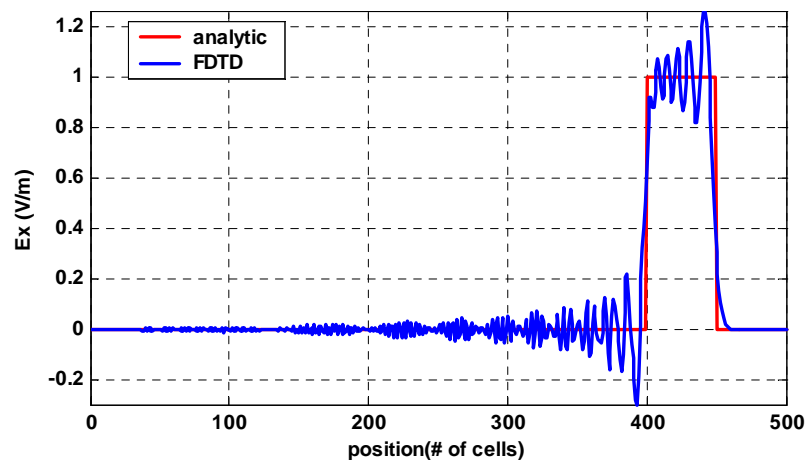


Figure 6-5: FDTD rectangular pulse propagation (CFL = 0.5)

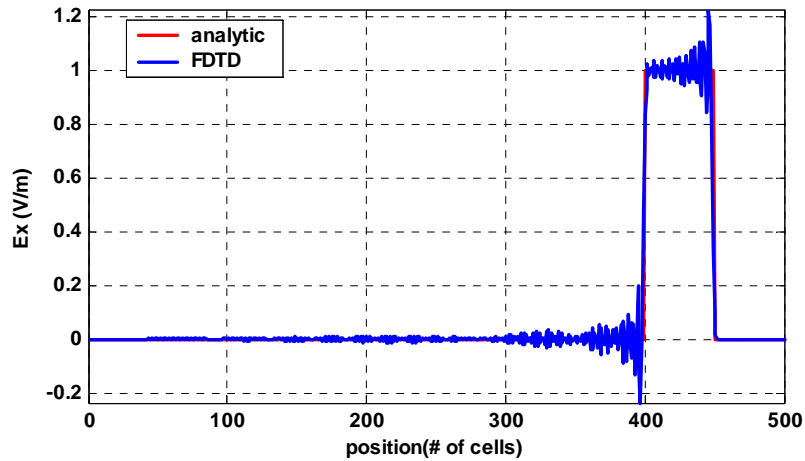


Figure 6-6: FDTD rectangular pulse propagation (CFL = 0.99)

**Fine Grid** ( $\Delta z = \lambda_{\min}/10$ ): Now let us increase our spatial resolution and do our computations in finer grid. Presented results below are the values of  $E_x$  in the computational grid at the end of the observation time. Since we have increased the grid resolution twice, the observation time for the chosen CFL number will be doubled in the same grid compared to coarse case. That is, the observation times are  $900\Delta t$  for CFL = 1,  $1800\Delta t$  for CFL = 0.5 and  $990\Delta t$  for CFL = 0.99.

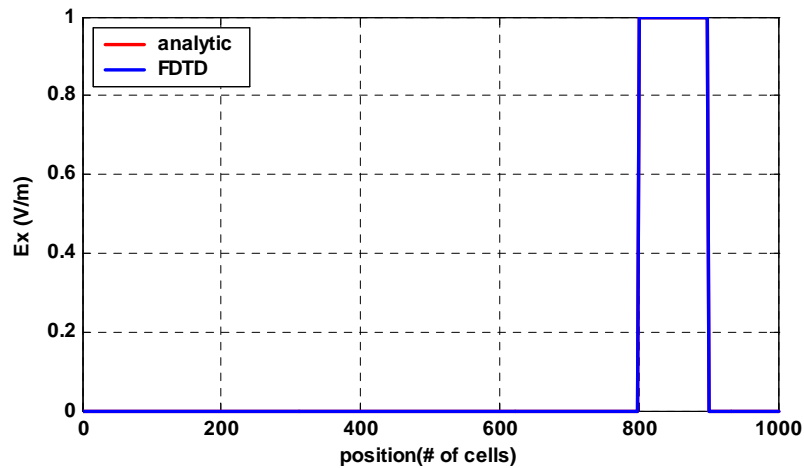


Figure 6-7: FDTD rectangular pulse propagation (CFL = 1)

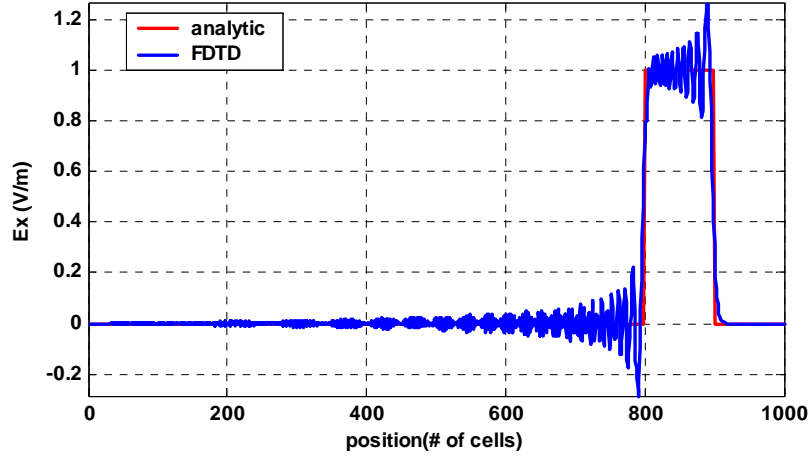


Figure 6-8: FDTD rectangular pulse propagation (CFL = 0.5)

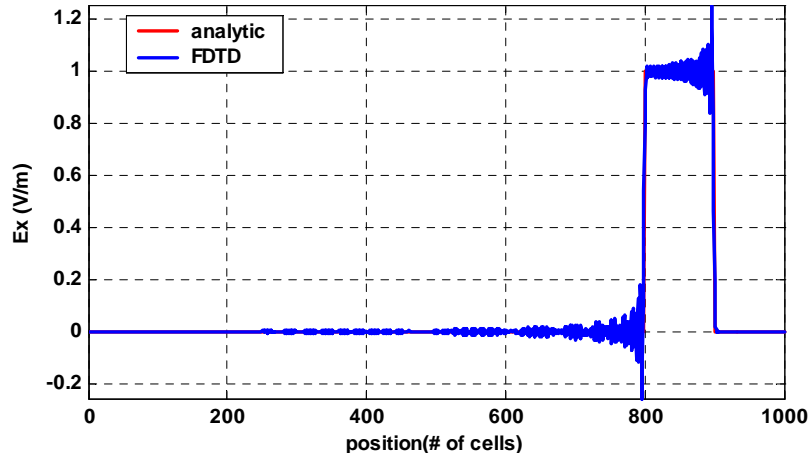


Figure 6-9: FDTD rectangular pulse propagation (CFL = 0.99)

Note that increasing spatial resolution has the same effect of increasing CFL number, causing increase in oscillation frequency of ripples but peak distortion still does not change. For this part, as a conclusion, we can state that only for CFL=1 can FDTD yield exact analytical result. FDTD can not track waveforms having discontinuities and needs smooth waveforms as is well known. Hence let us try Gaussian pulse.

### 6.2.2.2 Gaussian Pulse

Let excitation function  $f(t)$  be

$$f(t) = e^{-(t-t_0)^2/(\beta\Delta t)^2} \quad (6.5)$$

where  $t_0$  is the time at which the pulse reaches peak value (the mean) and  $\beta/\sqrt{2}$  is the variance of Gaussian pulse. We need to specify  $t_0$  and  $\beta$  so that the signal is turned on

smoothly and includes desired spectral content. [98] describes how to optimize a Gaussian pulse for FDTD simulation ensuring the turn-on value and  $f_{\max}$  are 140dB less than peak values of signal and frequency spectra respectively. Based on [98], they are determined as:

$$t_0 = 4\beta\Delta t, \quad \beta \geq 1.278/(f_{\max} \Delta t) \quad (6.6)$$

Time step  $\Delta t$  is again selected in accordance with CFL stability condition after choosing spatial grid spacings properly. Then discretized form of  $f(t)$  becomes

$$f(n) = e^{-(n-n_0)^2/(\beta)^2} \quad (6.7)$$

**Coarse Grid** ( $\Delta z = \lambda_{\min}/5$ ): Presented results below are the values of  $E_x$  in the computational grid at the end of the observation time. The observation times are  $450\Delta t$  for CFL = 1 and  $900\Delta t$  for CFL = 0.5.

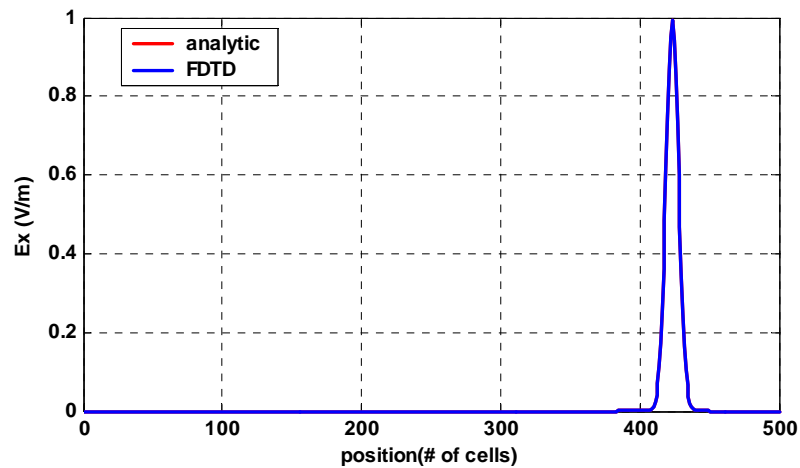


Figure 6-10: FDTD Gaussian pulse propagation (CFL = 1)

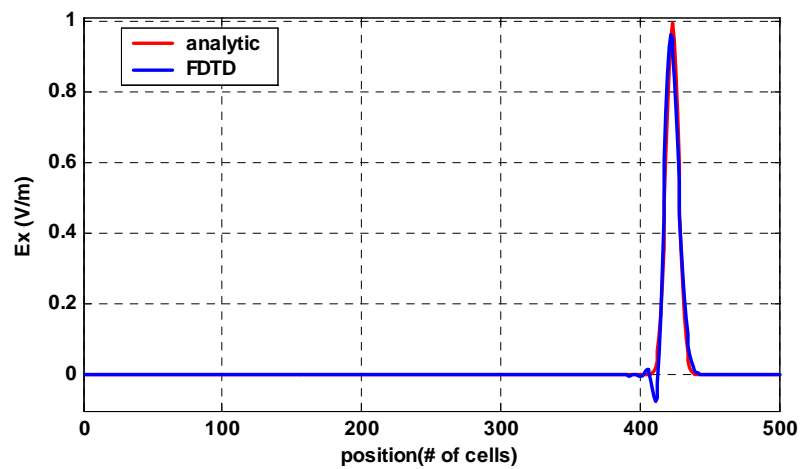


Figure 6-11: FDTD Gaussian pulse propagation (CFL = 0.5)

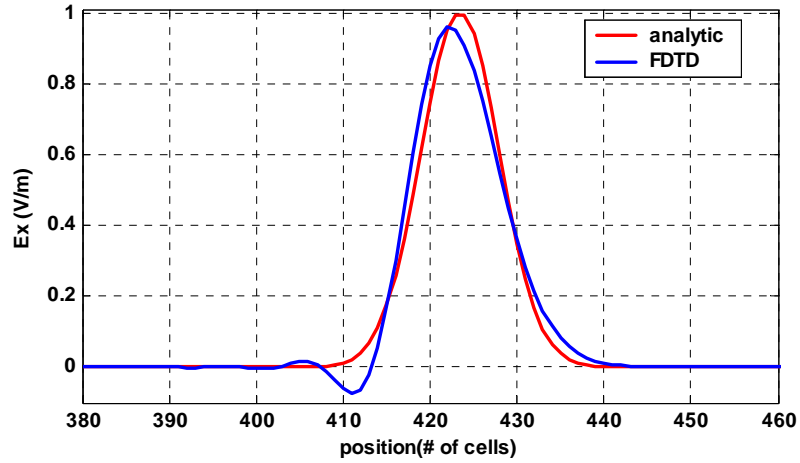


Figure 6-12: A closer look at the propagating pulse (CFL = 0.5)

Figure 6-10, Figure 6-11, Figure 6-12 show that, except CFL = 1, FDTD still induces numerical dispersion even for the propagating smooth Gaussian pulse. But that error is not as much dramatic as that of rectangular pulse. Again recall that numerical dispersion error would be worse at farther distances since it is cumulative.

**Fine Grid** ( $\Delta z = \lambda_{\min}/10$ ): For fine grid, the observation times are  $900\Delta t$  for CFL = 1 and  $1800\Delta t$  for CFL = 0.5.

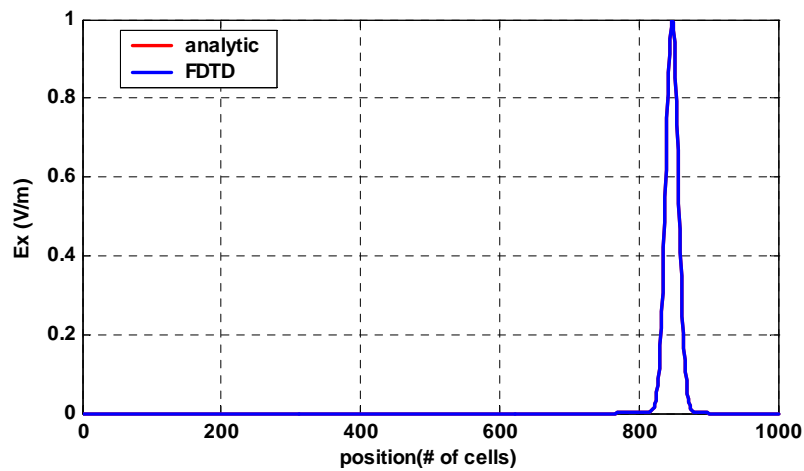


Figure 6-13: FDTD Gaussian pulse propagation (CFL = 1)

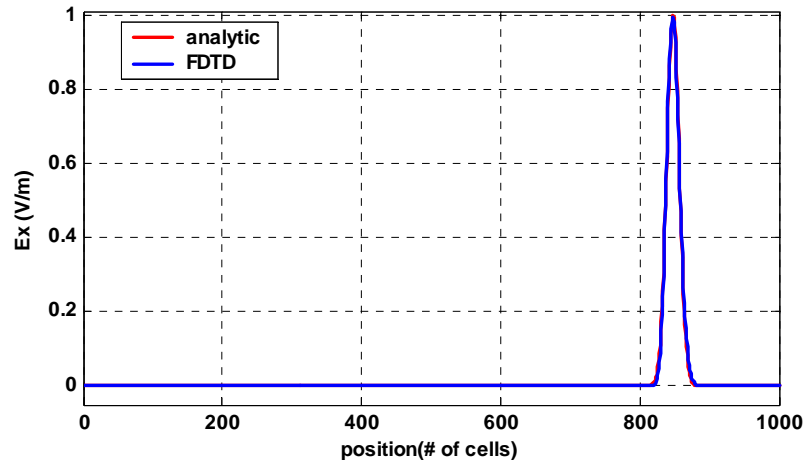


Figure 6-14: FDTD Gaussian pulse propagation (CFL = 0.5)

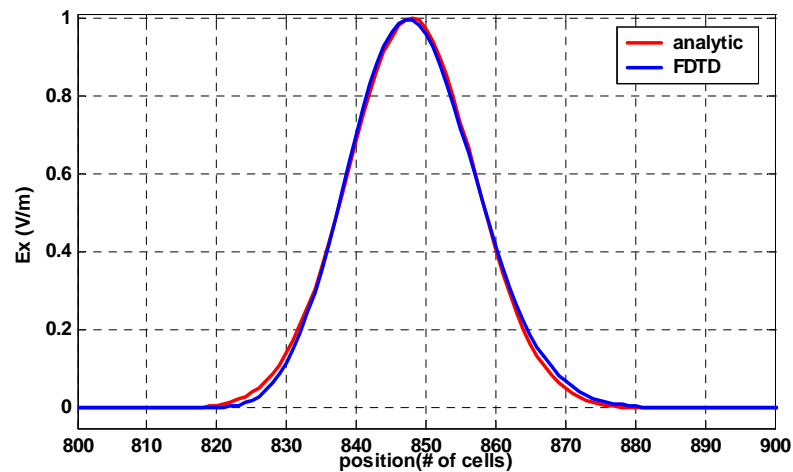


Figure 6-15: A closer look at the propagating pulse (CFL = 0.5)

As seen from Figure 6-14, Figure 6-15, increasing the grid resolution decreases the numerical dispersion and numerical results are more accurate but computational burden is heavier than coarse case due to increased resolution and reduced time step.

Another important observation on all the simulations upto now is the *superluminal effect* of FDTD. Note that, except CFL = 1, which yields exact analytical solution, FDTD computed pulse (both rectangular and Gaussian) somewhat leads the analytical pulse. As reported by Schneider [99], [100] some numerical modes propagate faster than velocity of light,  $c$ , in FDTD computational grid. It is also reported that these modes are attenuated rapidly and disappear as the wave propagates out [99], [100].

## 6.2.3 RBTD Implementation

### 6.2.3.1 Rectangular Pulse

**Determination of Discontinuities:** Considering rectangular pulse in Figure 6-3, we observe that there are only two 0<sup>th</sup> order discontinuities at the source (on the initial wave front where the excitation is defined). These are the initial values for  $\mathbf{A}_0$  occurring  $T$ sec apart.

$$\mathbf{A}_0(z_c) = [\mathbf{E}(z_c, t)] = \begin{cases} f(0^+) \hat{\mathbf{x}} - f(0^-) \hat{\mathbf{x}} = 1 \hat{\mathbf{x}}, & t = 0 \\ f(T^+) \hat{\mathbf{x}} - f(T^-) \hat{\mathbf{x}} = -1 \hat{\mathbf{x}}, & t = T \end{cases} \quad (6.8)$$

**Transport of Discontinuities:** The two 0<sup>th</sup> order discontinuities are propagated in computational grid in accordance with transport equations given by Eqn(5.12). In isotropic, homogeneous medium like this problem, they reduce to

$$\frac{d \mathbf{A}_0(s)}{ds} = \frac{d \mathbf{A}_0(z)}{dz} = 0 \quad (6.9)$$

$s$  is the arc length along ray. This implies that initial values of  $\mathbf{A}_0$  remain all constant.

**Construction of Time-Dependent Field:** At  $t = 0$ , the first one of the two 0<sup>th</sup> order  $\mathbf{A}_0$  discontinuities starts to propagate out into computational domain and then at  $t = T$  the second one appears at the source and starts to propagate out. Note that these are GO fields as described in Chapters 4 and 5. Then for construction of time-dependent field by Taylor series at a point, series expansion with only one term will consist of these GO field terms.

$$\mathbf{E}(z, t) = \begin{cases} \mathbf{A}_0(z) & t \geq z/c \\ 0 & t < z/c \end{cases} \quad (6.10)$$

Their individual responses at any point  $z = j\Delta z$  will be as the following.

$$\mathbf{E}_1 = E_{x1}(j\Delta z, n\Delta t) \hat{\mathbf{x}} = \begin{cases} 0 & j\Delta z/c > n\Delta t \\ 1 \hat{\mathbf{x}} & j\Delta z/c \leq n\Delta t \end{cases} \quad (6.11)$$

$$\mathbf{E}_2 = E_{x2}(j\Delta z, n\Delta t) \hat{\mathbf{x}} = \begin{cases} 0 & j\Delta z/c > n\Delta t - T \\ -1 \hat{\mathbf{x}} & j\Delta z/c \leq n\Delta t - T \end{cases}$$

Then total time-dependent field will be the sum.

$$\mathbf{E} = \mathbf{E}_1 + \mathbf{E}_2 \quad (6.12)$$

Due to the constant nature of discontinuities in this problem, there is no need to repeat the simulations for coarse and fine grids separately for RBTD. Therefore, we only present the coarse grid results at the end of the observation time,  $450\Delta t$ . Figure 6-16 shows the result. Recall that RBTD utilizes always  $CFL = 1$  on the ray.

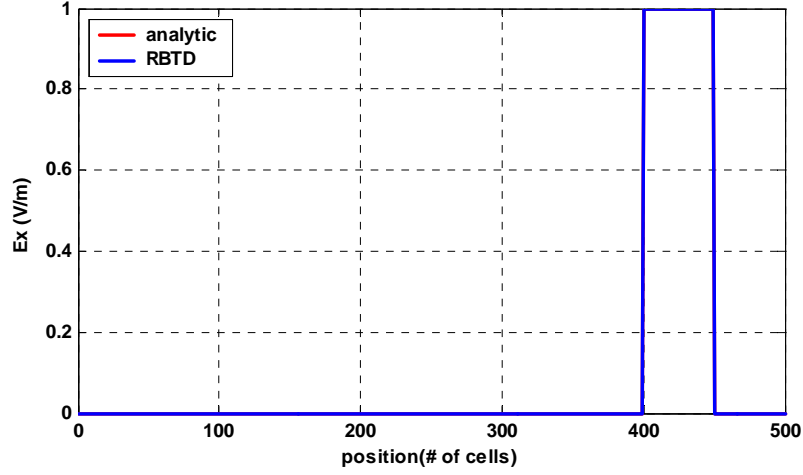


Figure 6-16: RBTD rectangular pulse propagation

### 6.2.3.2 Gaussian Pulse

Gaussian pulse can be expanded in power series around turn-on point ( $t=0$ ) or around the peak ( $t=t_0$ ) so that one can determine coefficients (discontinuities) of series expansion. However computational wise, that would be cumbersome to deal with many higher order discontinuity terms. Instead, we treat Gaussian pulse as consisting of sum of step functions shifted by  $\Delta t$  as if staircasing. Moreover we have already implemented the treatment of such *finite jump* discontinuities in rectangular pulse in the previous section. So we will follow the same reasoning. Considering the Gaussian pulse width as  $2n_0$  from Eqn(6.6), we assume that there is  $(2n_0+1)$   $0^{\text{th}}$  order discontinuities occurring at source shifted by  $\Delta t$  in time.

$$\mathbf{A}_0(z_c) = [\mathbf{E}(z_c, t)] = \begin{cases} f(0) \hat{\mathbf{x}}, & t = 0 \\ f(n\Delta t) \hat{\mathbf{x}} - f(n-1)\Delta t \hat{\mathbf{x}}, & 0 < t = n\Delta t \leq 2n_0\Delta t \end{cases} \quad (6.13)$$

They are subject to the same transport equation, and all remain constant throughout the computational domain. Individual time-dependent responses at any point  $z = j\Delta z$  will be found and then total time dependent field will be established by the summation of  $\Delta t$  shifted responses as in the previous section.

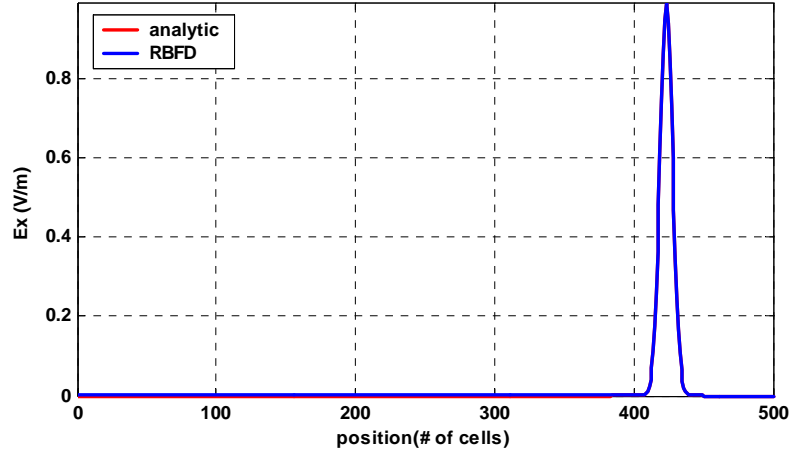


Figure 6-17: RBTD Gaussian pulse propagation

From RBTD plots, Figure 6-16 and Figure 6-17, one can observe that we propagate discontinuities exactly and construct time-dependent field exactly with no numerical dispersion no matter what the spatial resolution is or how long the wave propagates. For this problem, we can even go to equality case of Nyquist sampling condition in RBTD implementation. That would result in time step  $\Delta t$  which is the lower limit to reconstruct a given pulse signal in time. Under these conditions, FDTD results would certainly be worse and worse except CFL=1. Note that RBTD always uses  $\Delta z = c\Delta t$ , the equality case of CFL condition along ray, which is the magic time step. Moreover, *superluminal effect* of FDTD is also eliminated by RBTD due to the fact that each grid point has its time reference and no wave can exist at that point before its reference time. This is a physical fact used in RBTD.

### 6.3 Sample Problem II: 1-D Plane Wave with Dielectric Interface

#### 6.3.1 Computational Grid

PW simulations can be extended to incorporate reflection and refraction phenomena in addition to propagation. For this purpose, we put a dielectric medium ( $\epsilon_r = 4$ ) at distances  $z_d = 500\Delta z$  (for coarse grid) and  $z_d = 1000\Delta z$  (for fine grid). In real life,  $\epsilon_r$  exhibits frequency dependence. We ignore this point for simulations because it creates no problem to demonstrate applicability of methods. In both medium, grid spacing  $\Delta z$  is kept same. That means CFL number in medium 1 correspond a lower CFL value in medium 2. Computational grid for FDTD is shown in Figure 6-18. As for RBTD grid, wave fronts are  $\Psi = \sqrt{\epsilon_r} z = \text{constant}$  surfaces and rays are straight lines along  $z$ -axis as in Figure 6-19. Computational grid is still same and overlap for RBTD and FDTD grid.

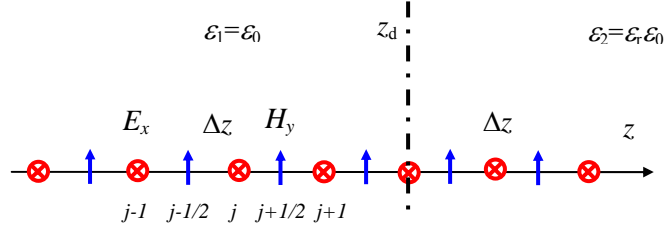


Figure 6-18: Computational grid

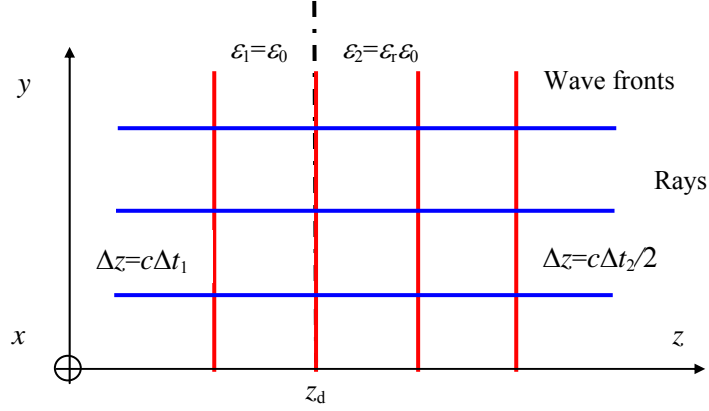


Figure 6-19: Wave fronts and rays for RBTD

Phase velocity is halved in medium 2 and hence wave needs  $2\Delta t$  time to traverse  $\Delta z$  distance. Otherwise, if we were to keep  $\Delta t$  constant for RBTD, then we would have to halve  $\Delta z$  in medium 2 because we have to implement  $\text{CFL} = 1$  ( $\Delta z = c\Delta t$ ) condition in both media as the requirement of RBTD.

### 6.3.2 FDTD Implementation

Accounting medium parameters, update equations Eqn(6.4) become

$$\begin{aligned}
 E_x^{n+1/2}(j) &= E_x^{n-1/2}(j) - \frac{\Delta t}{\varepsilon_0 \varepsilon(j) \Delta z} (H_y^n(j+1/2) - H_y^n(j-1/2)) \\
 H_y^{n+1}(j+1/2) &= H_y^n(j+1/2) - \frac{\Delta t}{\mu_0 \Delta z} (E_x^{n+1/2}(j+1) - E_x^{n-1/2}(j))
 \end{aligned} \tag{6.14}$$

Using reflected and refracted pulse amplitudes, one can calculate reflection, refraction coefficients and compare them with analytical ones.

$$\Gamma = \frac{E_x^r}{E_x^i} = \frac{Z_2 - Z_1}{Z_2 + Z_1}, \quad \tau = \frac{E_x^t}{E_x^i} = \frac{2Z_2}{Z_2 + Z_1} \tag{6.15}$$

where  $Z_1 = \sqrt{\mu_1/\varepsilon_1}$  and  $Z_2 = \sqrt{\mu_2/\varepsilon_2}$  are medium impedances. For simulations we specify CFL with respect to medium 1 as  $\text{CFL}_1 = 1$ .

### 6.3.2.1 Rectangular Pulse

Coarse grid ( $\Delta z = \lambda_{\min}/5$ ):

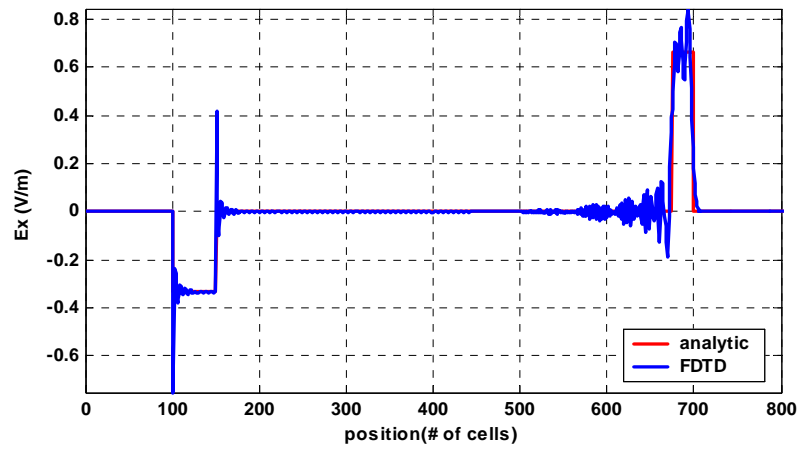


Figure 6-20: Reflection and refraction of FDTD rectangular pulse ( $CFL_1 = 1$ )

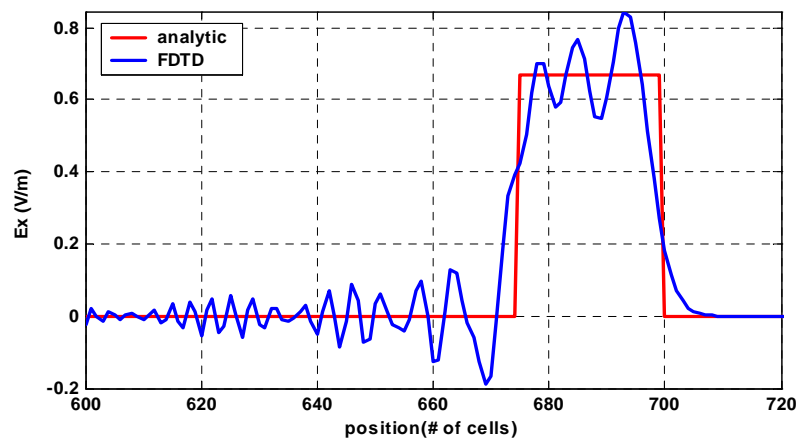


Figure 6-21: A closer look at the FDTD refracted pulse ( $CFL_1 = 1$ )

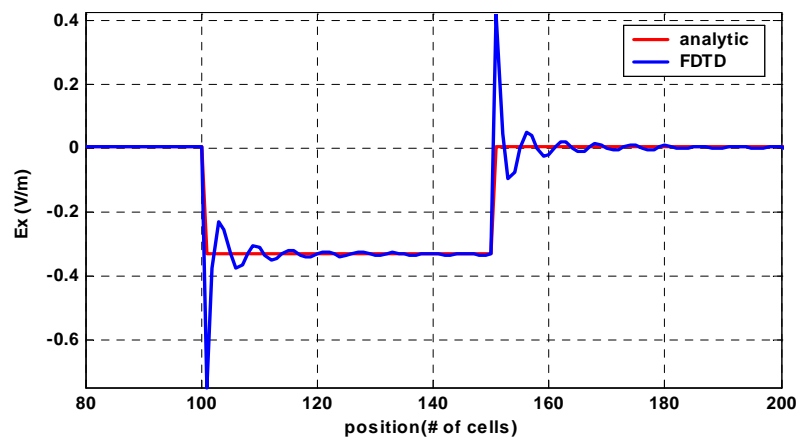


Figure 6-22: A closer look at the FDTD reflected pulse ( $CFL_1 = 1$ )

The observation times are  $900\Delta t$  for coarse grid and  $1800\Delta t$  for fine grid. Figure 6-20, Figure 6-21, and Figure 6-22 show us that both reflected and refracted pulses suffers from distortion. Distortion is more severe in medium 2 after refraction due to corresponding low CFL value in this medium ( $CFL_2 = 1$ ). However, reflected pulse also is distorted in medium 1 due to interactions at discontinuous boundary interface although  $CFL_1 = 1$  is maintained. One can also more easily observe superluminal effect on the pulses at the closer look plots.

**Fine Grid** ( $\Delta z = \lambda_{\min}/10$ ):

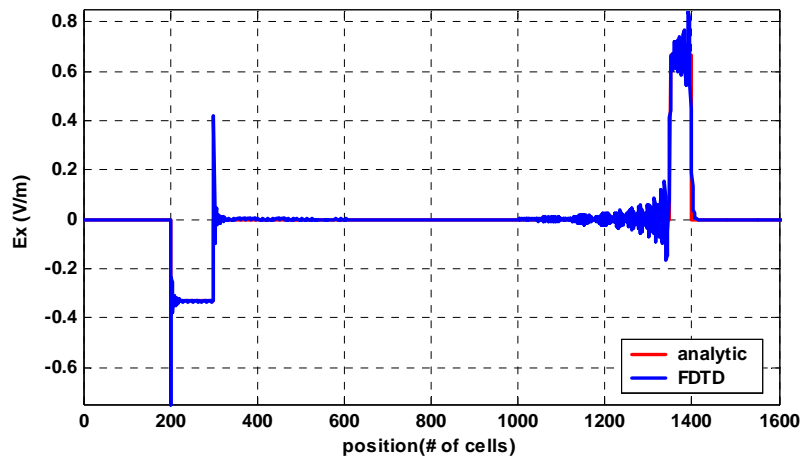


Figure 6-23: Reflection and refraction of FDTD rectangular pulse ( $CFL_1 = 1$ )

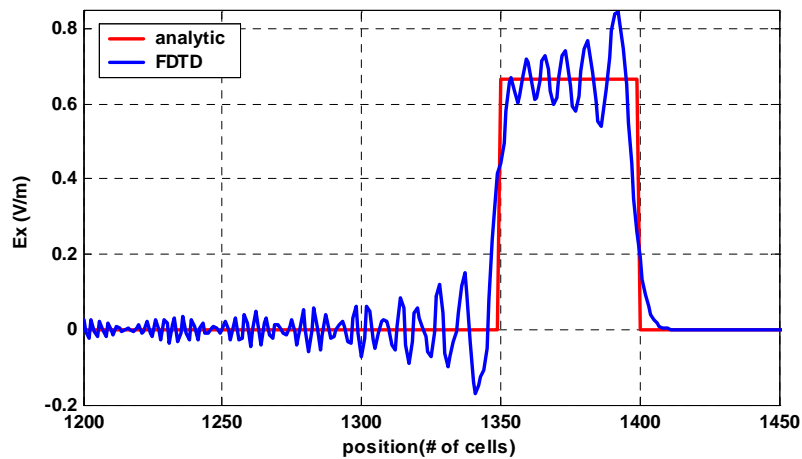


Figure 6-24: A closer look at the FDTD refracted pulse ( $CFL_1 = 1$ )

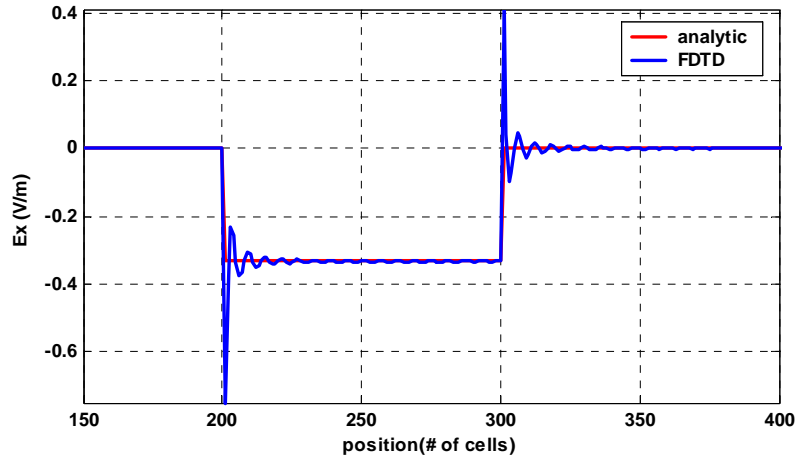


Figure 6-25: A closer look at the FDTD reflected pulse ( $CFL_1 = 1$ )

Finer grid produces results closer to analytical ones but the nature of error remains same for rectangular pulse. Next we will see what will happen for Gaussian pulse.

### 6.3.2.2 Gaussian Pulse

**Coarse Grid** ( $\Delta z = \lambda_{\min}/5$ ):

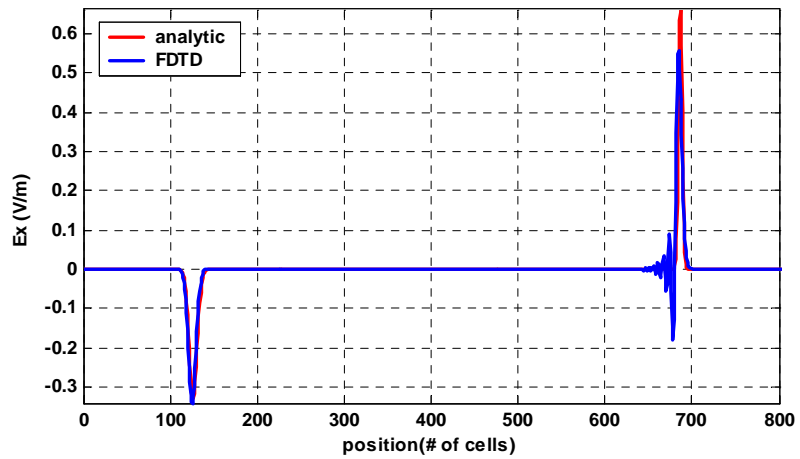


Figure 6-26: Reflection and refraction of FDTD Gaussian pulse ( $CFL_1 = 1$ )

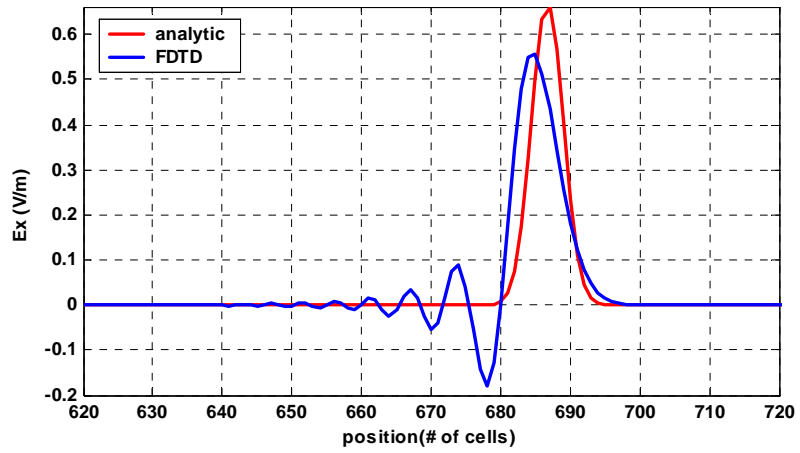


Figure 6-27: A closer look at the FDTD refracted pulse ( $CFL_1 = 1$ )

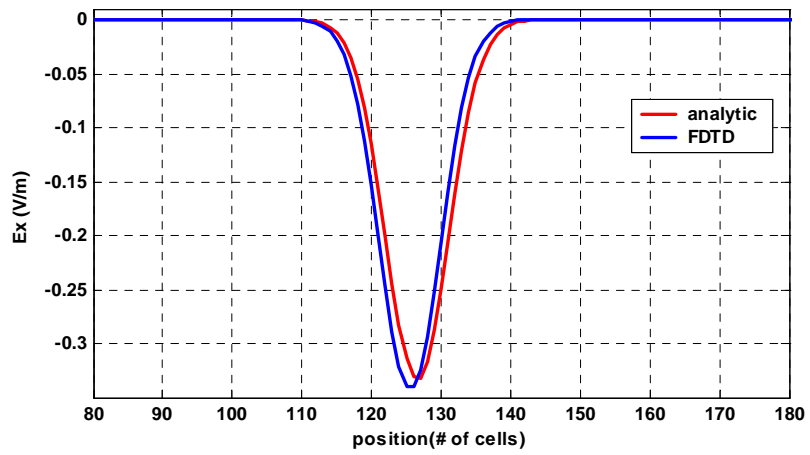


Figure 6-28: A closer look at the FDTD reflected pulse ( $CFL_1 = 1$ )

**Fine Grid** ( $\Delta z = \lambda_{\min}/10$ ):

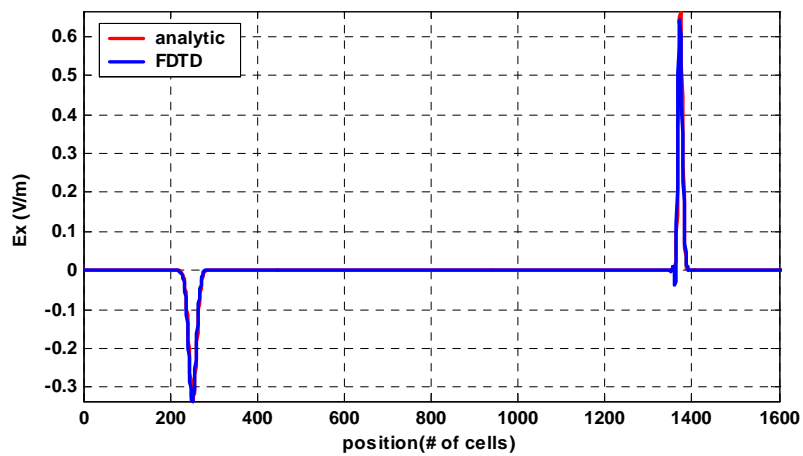


Figure 6-29: Reflection and refraction of FDTD Gaussian pulse ( $CFL_1 = 1$ )

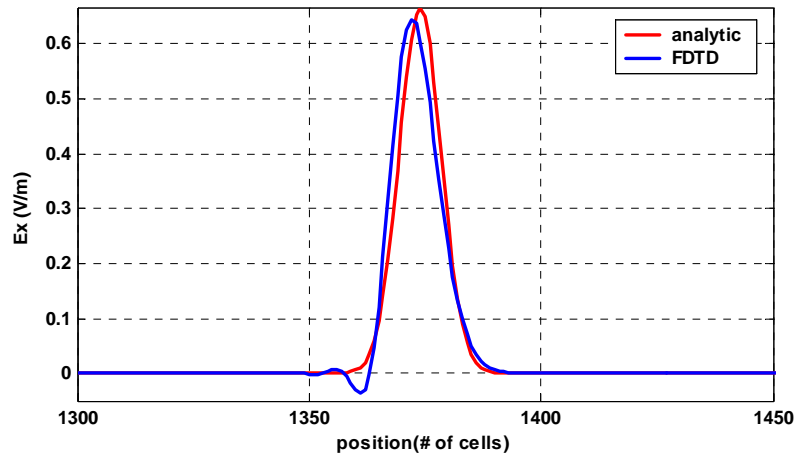


Figure 6-30: A closer look at the FDTD refracted pulse ( $CFL_1 = 1$ )

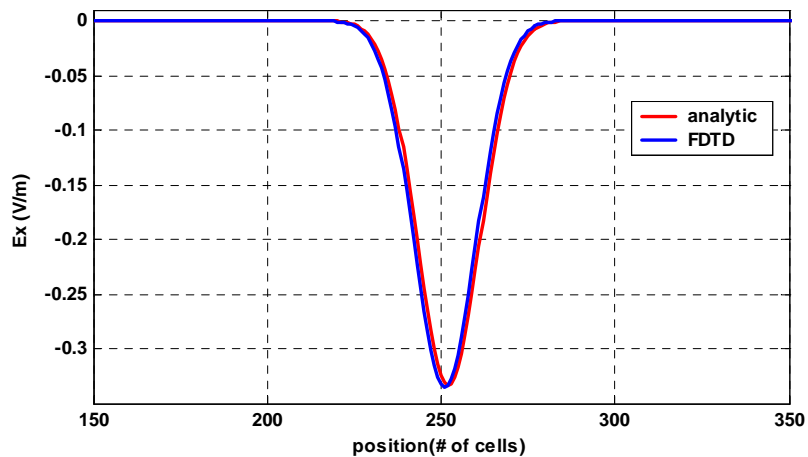


Figure 6-31: A closer look at the FDTD reflected pulse ( $CFL_1 = 1$ )

Similar comments as in rectangular pulse case applies to Gaussian pulse for coarse and fine grid. But as seen in the above figures, fine grid works much better, for Gaussian pulse since it is smooth function and has no jump discontinuities.

### 6.3.3 RBTD Implementation

**Determination of Discontinuities:** Discontinuities are the same as those of Sample Problem I, Eqn(6.8) for rectangular and Eqn(6.13) for Gaussian pulse. They all are 0<sup>th</sup> order discontinuities occurring at different time instants.

**Transport of Discontinuities:** Discontinuities are also transported in the same fashion as in Sample Problem I. Transport equation, Eqn(6.9), applies individually to both media. The peculiarity of current problem is the existence of stationary discontinuity hypersurface

$\Psi(x,y,z) = z_d$  between two media. As discussed in Section 3.5.7, discontinuities obey the Snell's law of reflection and refraction. Fresnel formulas of Eqn(4.59) are directly applicable to determine reflected and refracted 0<sup>th</sup> order discontinuities or we can immediately use Eqn(6.15). Remember that neat, compact formulas, similar to Fresnel formulas, for higher order discontinuities are not available for time being, and needs to be further elaboration. However, we have provided the way it is done for the 1<sup>st</sup> order discontinuities in section 4.5. Using Eqn(6.15), reflected and refracted discontinuities at the boundary are found as Eqn(6.16). We just need to implement this physical fact at the boundary.

$$\mathbf{A}_0^r = \Gamma \mathbf{A}_0^i, \quad \mathbf{A}_0^t = \tau \mathbf{A}_0^i \quad (6.16)$$

**Construction of Time-Dependent Field:** The same reasoning in Sections 5.2.3.1 and 5.2.3.2 to construct time-dependent field applies here too. After determining 0<sup>th</sup> order discontinuities in medium 1 as incident and reflected and in medium 2 as refracted on the rays with their associated time reference, time-dependent incident, reflected and refracted fields can be constructed by again Taylor series. Considering rectangular pulse and first one of the discontinuities, one can write

$$\begin{aligned} \mathbf{E}_1^i &= E_{x1}^i(j\Delta z, n\Delta t) \hat{\mathbf{x}} = \begin{cases} 0 & j\Delta z/c > n\Delta t \\ A_{01}^i \hat{\mathbf{x}} & j\Delta z/c \leq n\Delta t \end{cases} \\ \mathbf{E}_1^r &= E_{x1}^r(j\Delta z, n\Delta t) \hat{\mathbf{x}} = \begin{cases} 0 & |j\Delta z - z_d|/c > n\Delta t - T_d \\ \Gamma A_{01}^i \hat{\mathbf{x}} & |j\Delta z - z_d|/c \leq n\Delta t - T_d \end{cases} \\ \mathbf{E}_1^t &= E_{x1}^t(j\Delta z, n\Delta t) \hat{\mathbf{x}} = \begin{cases} 0 & |j\Delta z - z_d|/\nu > n\Delta t - T_d \\ \tau A_{01}^i \hat{\mathbf{x}} & |j\Delta z - z_d|/\nu \leq n\Delta t - T_d \end{cases} \end{aligned} \quad (6.17)$$

Note that  $\nu = c/2$  in medium 2.  $T_d$  is the time difference between source at  $z = z_c$  and dielectric interface at  $z = z_d$ . Incident, reflected and refracted fields due to the second 0<sup>th</sup> order discontinuity on the initial wave front occurring  $T$ (sec) later in rectangular pulse can also be written as:

$$\begin{aligned} \mathbf{E}_2^i &= E_{x2}^i(j\Delta z, n\Delta t) \hat{\mathbf{x}} = \begin{cases} 0 & j\Delta z/c > n\Delta t - T \\ A_{02}^i \hat{\mathbf{x}} & j\Delta z/c \leq n\Delta t - T \end{cases} \\ \mathbf{E}_2^r &= E_{x2}^r(j\Delta z, n\Delta t) \hat{\mathbf{x}} = \begin{cases} 0 & |j\Delta z - z_d|/c > n\Delta t - T_d - T \\ \Gamma A_{02}^i \hat{\mathbf{x}} & |j\Delta z - z_d|/c \leq n\Delta t - T_d - T \end{cases} \\ \mathbf{E}_2^t &= E_{x2}^t(j\Delta z, n\Delta t) \hat{\mathbf{x}} = \begin{cases} 0 & |j\Delta z - z_d|/\nu > n\Delta t - T_d - T \\ \tau A_{02}^i \hat{\mathbf{x}} & |j\Delta z - z_d|/\nu \leq n\Delta t - T_d - T \end{cases} \end{aligned} \quad (6.18)$$

Since incident and reflected wave front/ray grids in medium 1 overlaps onto each other, then total time-dependent field in medium 1 is

$$\mathbf{E} = \mathbf{E}_1^i + \mathbf{E}_2^i + \mathbf{E}_1^r + \mathbf{E}_2^r \quad (6.19)$$

And in medium 2, there is only refracted field

$$\mathbf{E} = \mathbf{E}_1^t + \mathbf{E}_2^t \quad (6.20)$$

### 6.3.3.1 Rectangular Pulse

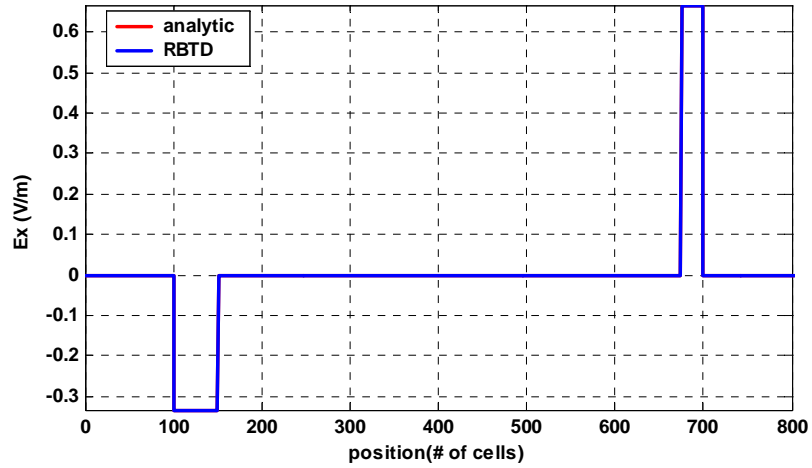


Figure 6-32: Reflection and Refraction of RBTB rectangular pulse

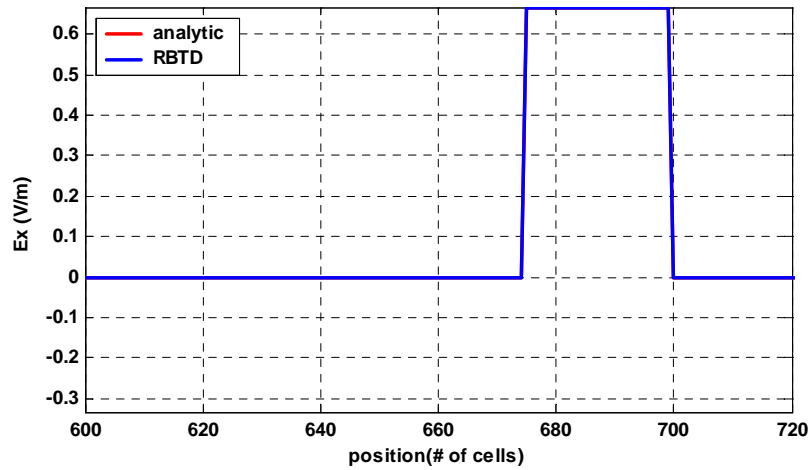


Figure 6-33: A closer look at the RBTB refracted pulse

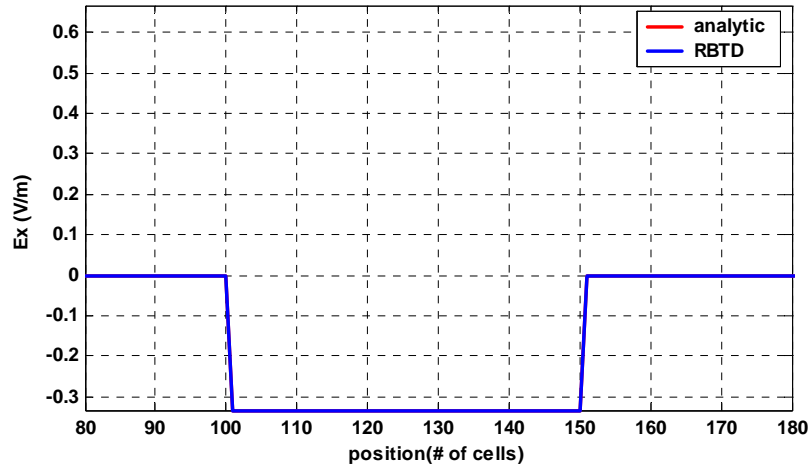


Figure 6-34: A closer look at the RBDT reflected pulse

### 6.3.3.2 Gaussian Pulse

Gaussian pulse is again treated as the weighted sum of shifted step functions and discontinuities are determined as in Eqn(6.13). Propagation of these discontinuities and construction of incident, reflected and refracted time-dependent fields are also same as previous section. The only difference is that now we deal with not only two 0<sup>th</sup> order discontinuity but at least  $(2n_0+1)$  0<sup>th</sup> order discontinuities occurring at source shifted by  $\Delta t$  in time due to staircase approximation of the Gaussian pulse.

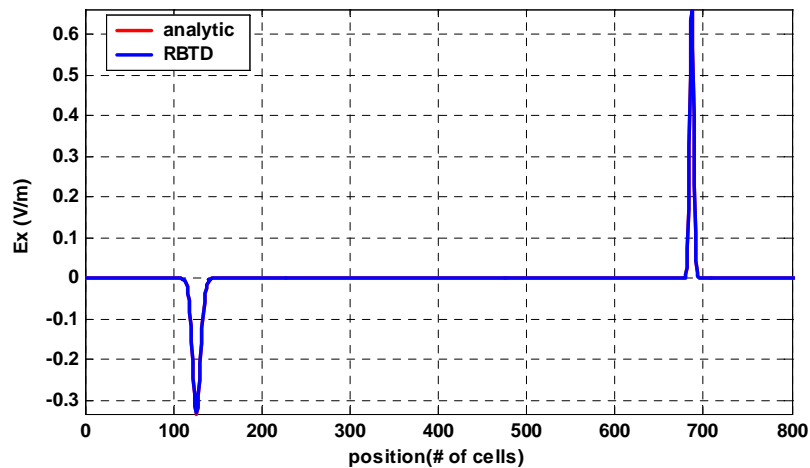


Figure 6-35: Reflection and refraction of RBDT Gaussian pulse

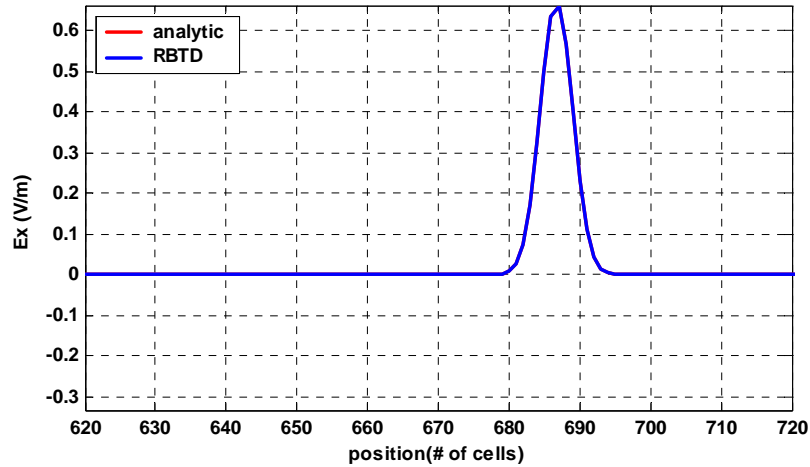


Figure 6-36: A closer look at the RBDT refracted pulse

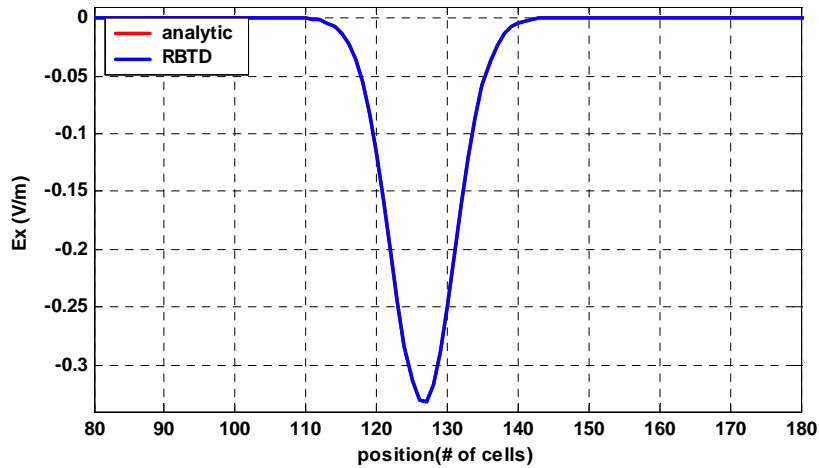


Figure 6-37: A closer look at the RBDT reflected pulse

It is understood from Figure 6-36 and Figure 6-37 that RBDT is able to construct incident, reflected and refracted pulses (either rectangular or Gaussian) perfectly. No numerical dispersion, no error! Hence as expected, reflection and transmission coefficient calculations, Eqn(6.15) in Section 6.3.2, will be much more reliable than FDTD for such problems, using pulse amplitudes. One final remark is that spatial pulse width in medium 2 is halved due to halved phase velocity in the medium ( $\epsilon_r = 4$ ). This is observed in all refracted pulses. Also note that we have provided RBDT results for coarse grid only because discontinuities remain same and constant in the computational domain for both coarse and fine grid. No need to repeat the simulation for fine grid.

#### 6.4 Sample Problem III: Electric Dipole in Homogeneous Medium

Next, Hertzian electric dipole radiating in isotropic, homogeneous medium, i.e.,  $(\epsilon_0, \mu_0)$ , is considered in spherical coordinates  $(R, \theta, \varphi)$ , Figure 6-38.

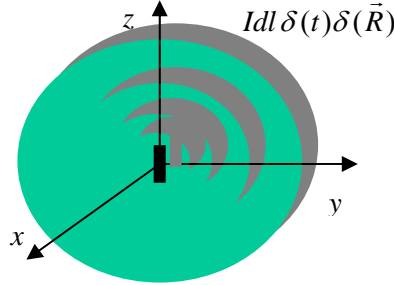


Figure 6-38: Radiating Hertzian electric dipole

The analytical impulse response is given by [103]:

$$\begin{aligned}
 E_R(\mathbf{R}, t) &= \frac{ZIdl}{4\pi} \cos \theta \left( \frac{2\delta(t - R/c)}{R^2} + \frac{2cu(t - R/c)}{R^3} \right) \\
 E_\theta(\mathbf{R}, t) &= \frac{ZIdl}{4\pi} \sin \theta \left( \frac{\delta'(t - R/c)}{cR} + \frac{\delta(t - R/c)}{R^2} + \frac{cu(t - R/c)}{R^3} \right) \\
 H_\varphi(\mathbf{R}, t) &= \frac{Idl}{4\pi} \sin \theta \left( \frac{\delta'(t - R/c)}{cR} + \frac{\delta(t - R/c)}{R^2} \right)
 \end{aligned} \tag{6.21}$$

where  $\mathbf{R} = x\hat{\mathbf{x}} + y\hat{\mathbf{y}} + z\hat{\mathbf{z}}$ , and  $Idl$ ,  $Z$  are dipole moment (strength of the dipole) and medium impedance respectively.  $\delta(t)$ ,  $\delta'(t)$  and  $u(t)$  stand for doublet, impulse and step functions respectively. For simulations we will consider ramp response for the ease of implementation. Ramp response of Hertzian dipole (for example  $E_\theta$ ) itself is already in power series form. Then discontinuities will be determined directly by inspection for RBTD. Different than standard Yee algorithm, spherical FDTD [40] will be used for simulation. We believe this example is very didactic to understand RBTD better and compare it with FDTD. When considered ramp input;  $\delta(t)$ ,  $\delta'(t)$  and  $u(t)$  in Eqn(6.21) will be replaced by  $u(t)$ ,  $r(t)$  and  $q(t)$  respectively where  $r(t) = tu(t)$  is ramp function and  $q(t) = (1/2)t^2u(t)$  is quadratic function. Eqn(6.21) then becomes

$$\begin{aligned}
E_R(\mathbf{R},t) &= \frac{Zidl}{4\pi} \cos\theta \left( \frac{2r(t-R/c)}{R^2} + \frac{2cq(t-R/c)}{R^3} \right) \\
E_\theta(\mathbf{R},t) &= \frac{Zidl}{4\pi} \sin\theta \left( \frac{u(t-R/c)}{cR} + \frac{r(t-R/c)}{R^2} + \frac{cq(t-R/c)}{R^3} \right) \\
H_\varphi(\mathbf{R},t) &= \frac{Idl}{4\pi} \sin\theta \left( \frac{u(t-R/c)}{cR} + \frac{r(t-R/c)}{R^2} \right)
\end{aligned} \tag{6.22}$$

Note that although this is a 3-D problem, there is  $\varphi$ -axis symmetry and it can be treated as 2-D problem at any  $\varphi = \text{constant}$  surface. To this end, we will do our computations on  $yz$ -plane where  $\varphi = 90^\circ$ .

#### 6.4.1 Computational Grid

Spherical coordinates have been used as natural grid for FDTD. Figure 6-39 depicts wave fronts, constant radius concentric spheres while Figure 6-40 depicts rays, straight radial lines, on  $yz$  plane. Since the medium is isotropic and homogeneous, RBTD and FDTD computational grids are same and overlap. They are easily generated exactly as will be discussed in Chapter 6. In these plots, we started to generate computational grid (same as wave fronts and rays) with initial spherical wave front of radius  $R_0 = 1\text{m}$ .

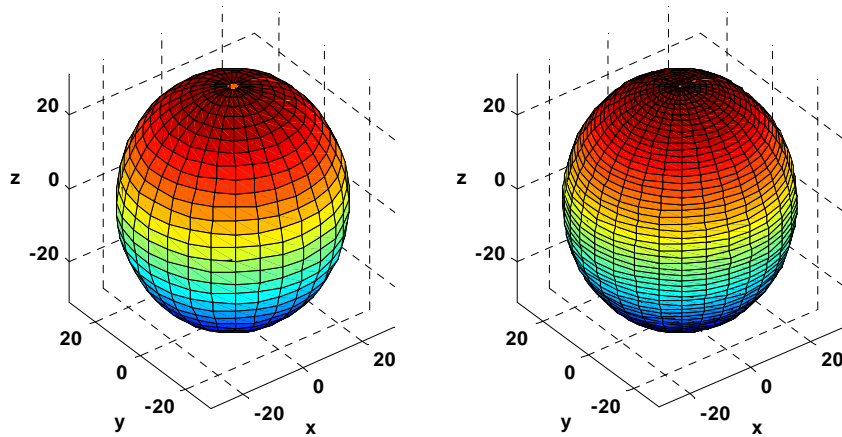


Figure 6-39: Computational grid, wave fronts for coarse and fine grid

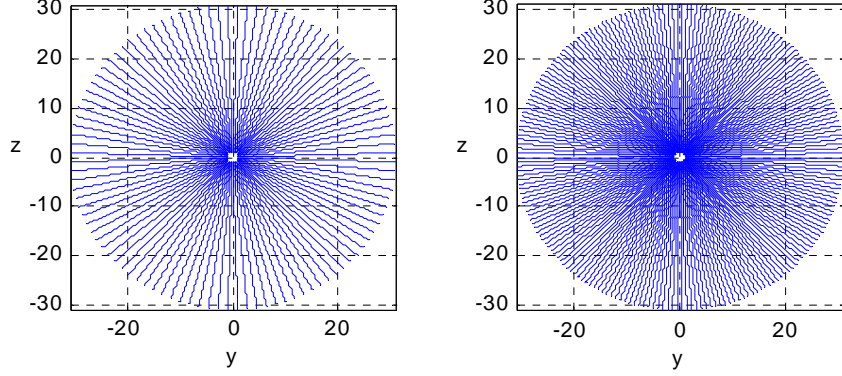


Figure 6-40: Computational grid, rays for coarse and fine grids

#### 6.4.2 Spherical FDTD Implementation

Holland [40] provided the first FDTD implementation in spherical coordinates which is the early work of conformal gridding. Then he reported [50] FDTD formulation for nonorthogonal curvilinear coordinates based on Stratton's work [51]. The results of [40] which provides us field update equations in spherical coordinates can be summarized as in Eqn(6.23). We define analytical  $E_0$  field as the input over given initial spherical wave front surface. It is sufficient to specify only tangential electric field which is  $E_0$  [40]. The nature of the problem dictates radial outgoing wave only.

$$\begin{aligned}
 E_R^{n+1}(i,k) &= E_R^n(i,k) + \frac{\Delta t}{\varepsilon_0 R(i) \sin \theta(k)} \left( \frac{\sin \theta(k) H_\phi^{n+1/2}(i,k) - \sin \theta(k-1) H_\phi^{n+1/2}(i,k-1)}{\Delta \theta} \right) \\
 E_\theta^{n+1}(i,k) &= E_\theta^n(i,k) - \frac{\Delta t}{\varepsilon_0 R(i)} \left( \frac{R(i) H_\phi^{n+1/2}(i,k) - R(i-1) H_\phi^{n+1/2}(i-1,k)}{\Delta R} \right) \\
 H_\phi^{n+1/2}(i,k) &= H_\phi^{n-1/2}(i,k) - \frac{\Delta t}{\mu_0 R(i)} \left( \frac{R(i+1) E_\theta^n(i+1,k) - R(i) E_\theta^n(i,k)}{\Delta R} \right. \\
 &\quad \left. - \frac{E_R^n(i,k+1) - E_R^n(i,k)}{\Delta \theta} \right)
 \end{aligned} \tag{6.23}$$

Throughout the simulations for Sample problem III and IV, we again assume  $f_{\max} = 1\text{GHz}$ . Since ramp signal is smoother than rectangular pulse, assumption of  $f_{\max} = 1\text{GHz}$  is still secure for both ramp and Gaussian as verified in Section 5.2.2. We adopt again two kinds of grid structure. The specification in Table 6-2 applies to discretization on initial wave front where initial field is defined.

Table 6-2: Coarse and fine grid for Sample Problem III and IV.

	<b>Coarse grid</b>	<b>Fine Grid</b>
$\Delta R$	$\lambda_{\min} / 5$	$\lambda_{\min} / 10$
$\Delta \theta$	$R_0 \Delta \theta = \lambda_{\min} / 5 = \pi / M \Rightarrow M = 52$	$R_0 \Delta \theta = \lambda_{\min} / 10 = \pi / M \Rightarrow M = 105$

$\Delta t$  is selected to satisfy CFL stability condition using smallest grid dimensions.

$$\Delta t \leq 1/c \sqrt{\left(\frac{1}{\Delta R}\right)^2 + \left(\frac{1}{R_0 \Delta \theta}\right)^2} \quad (6.24)$$

For simulations, we set it to

$$\Delta t = 1/\sqrt{2}c \sqrt{\left(\frac{1}{\Delta R}\right)^2 + \left(\frac{1}{R_0 \Delta \theta}\right)^2} \quad (6.25)$$

Let us assume our excitation so that  $ZI dl/4\pi = 1$  in Eqn(6.22), and proceed further.

#### 6.4.2.1 Ramp Pulse

The computational grid extends from sphere of  $R_0 = 1\text{m}$  to  $R = 31\text{m}$  with corresponding increment  $\Delta R$  for coarse and fine grids. Next figures depict tangential electric field at the positions  $i = 400\Delta R$  (far field),  $i = 100\Delta R$  (near field) for coarse grid and  $i = 800\Delta R$  (far field),  $i = 200\Delta R$  (near field) for fine grid. The observation time is  $1000\Delta t$  (coarse) and  $2000\Delta t$  (fine). Elevation angle observation point is at  $k = M/4 = 13$  for coarse and  $k = M/4 \cong 26$  for fine grid. That means we are looking at the response with an angle of  $45^\circ$  from  $z$ -axis and at a distance of  $25\text{m}$  (far field) and  $7\text{m}$  (near field) from the origin approximately. Computed  $E_\theta$  results are as follows:

Coarse Grid:

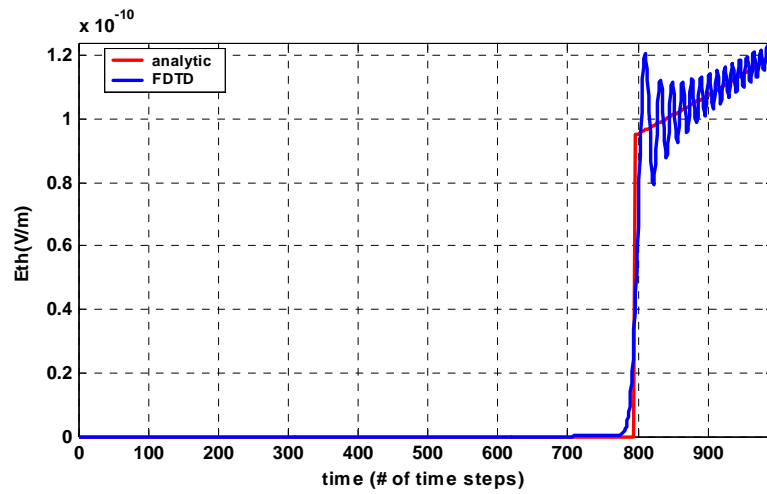


Figure 6-41: Propagation of FDTD ramp response (*far field*)

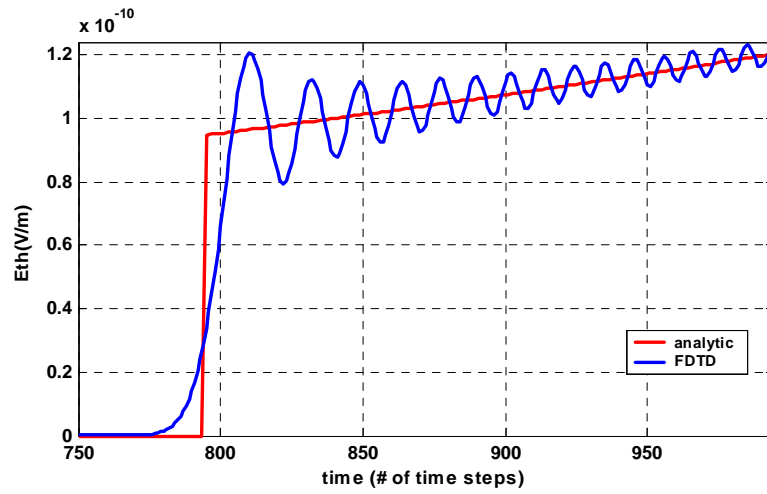


Figure 6-42: A closer look at the propagating pulse (*far field*)

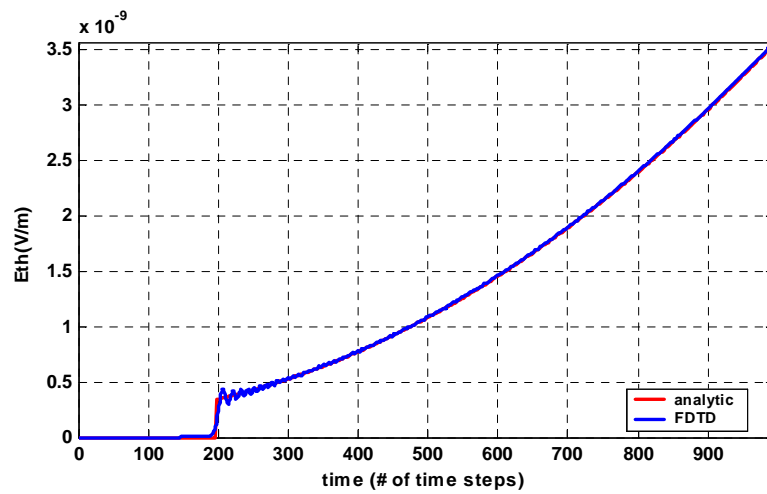


Figure 6-43: Propagation of FDTD ramp response (*near field*)

Although the ramp input is smooth, there exists numerical dispersion in the response because dipole produces step discontinuity in  $E_\theta$  (the first term in Eqn(6.22)). FDTD can not track that discontinuity. As seen from Figure 6-41, Figure 6-42, Figure 6-43, numerical dispersion is more at far field as expected. Now we do our computations for fine grid as described in Table 6-2.

**Fine Grid:**

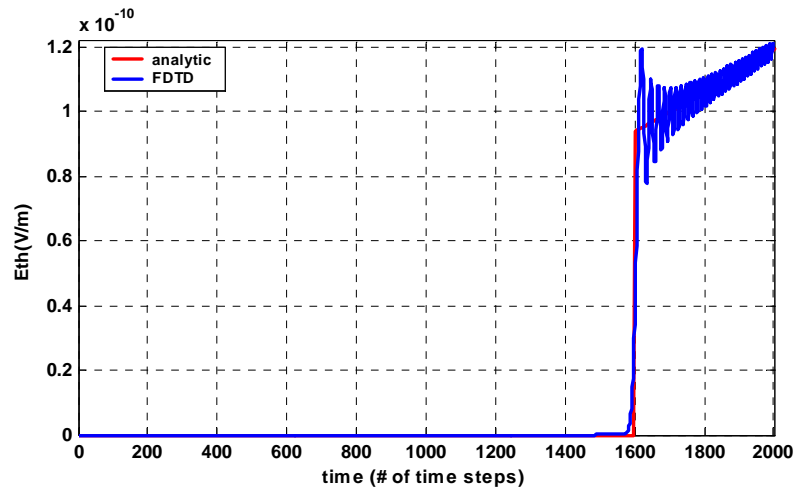


Figure 6-44: Propagation of FDTD ramp response (*far field*)

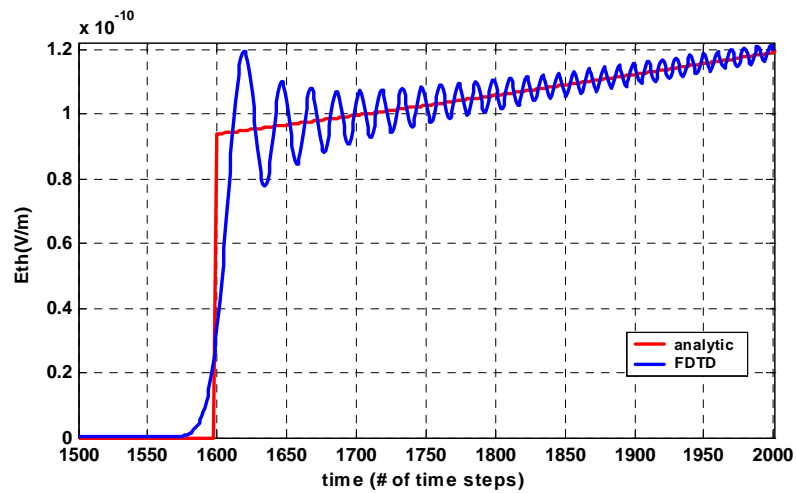


Figure 6-45: A closer look at the propagating pulse (*far field*)

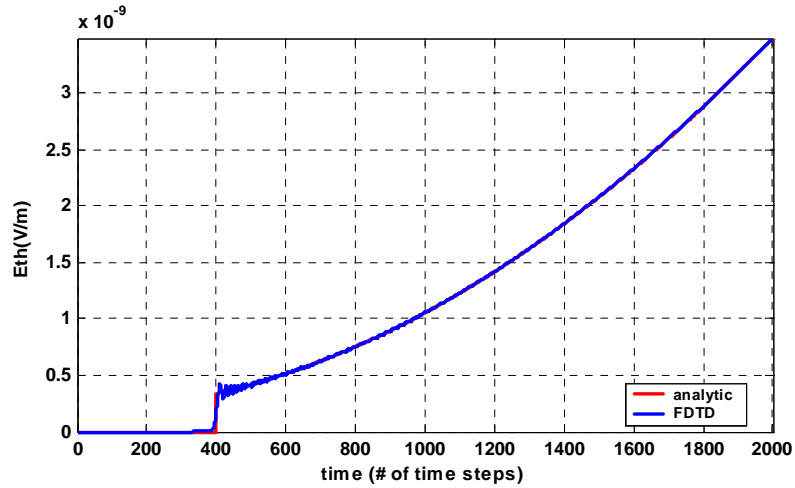


Figure 6-46: Propagation of FDTD ramp response (*near field*)

### 6.4.2.2 Gaussian Pulse

For Gaussian input,  $u(t)$ ,  $r(t)$  and  $q(t)$  in Eqn(6.22) are replaced by derivative of Gaussian, Gaussian and integral of Gaussian (error function) respectively. Different than the plots upto here, we now look at the propagating pulse in both space and time, that is, at all grid points along a ray at the end of observation time and at a fixed grid point (near field and far field) during observation time. Grid structures are as described in Table 6-2.

**Coarse Grid:**

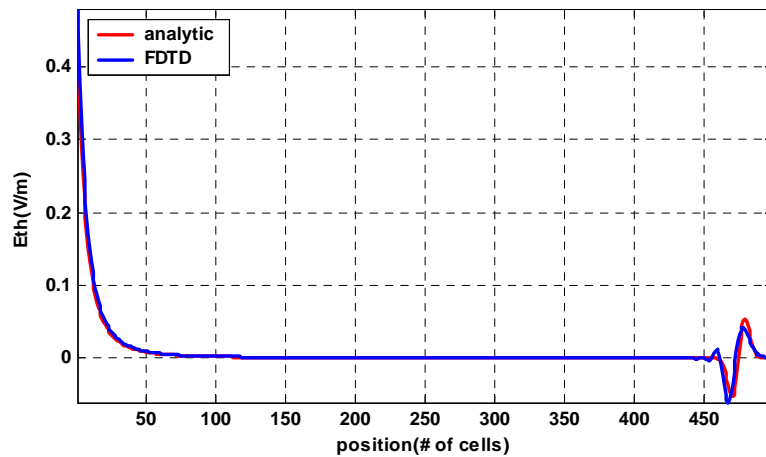


Figure 6-47: Propagating FDTD Gaussian response (*spatial*)

Observe that there exists significant signal at the source (initial wave front) although the Gaussian wave arrives at the end of computational domain. This is due to the integral of Gaussian term in Eqn(6.22), which may be called as static term. This static term can easily be conferred from impulse response, Eqn(6.21). Physically, as soon as the dipole is turned on, charges immediately move to  $z = dl/2$  and  $z = -dl/2$ . Then they remain static and produce static field effective in near field. Since it decays with  $1/R^3$  in Eqn(6.21), it becomes negligible at far field.

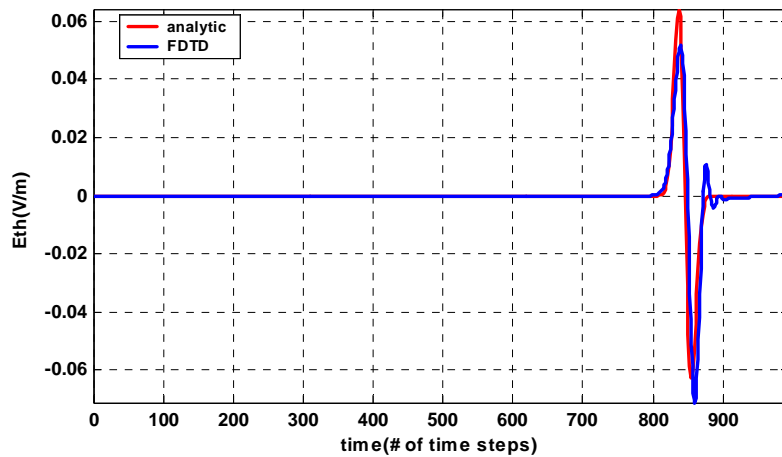


Figure 6-48: Propagating FDTD Gaussian response (*temporal, far field*)

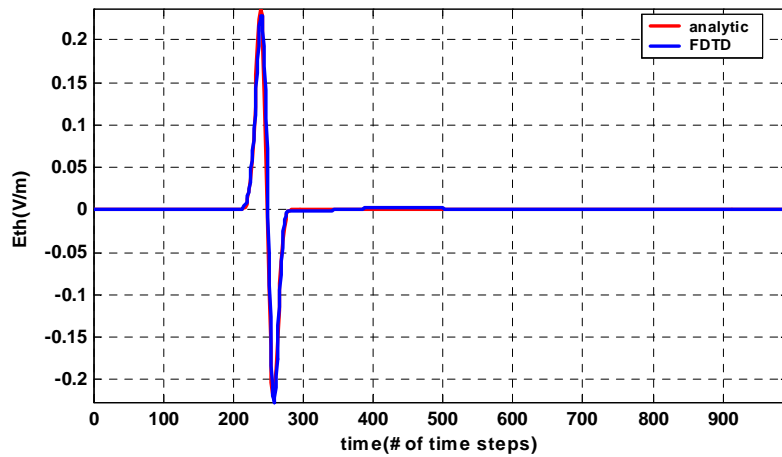


Figure 6-49: Propagating FDTD Gaussian response (*temporal, near field*)

**Fine Grid:**

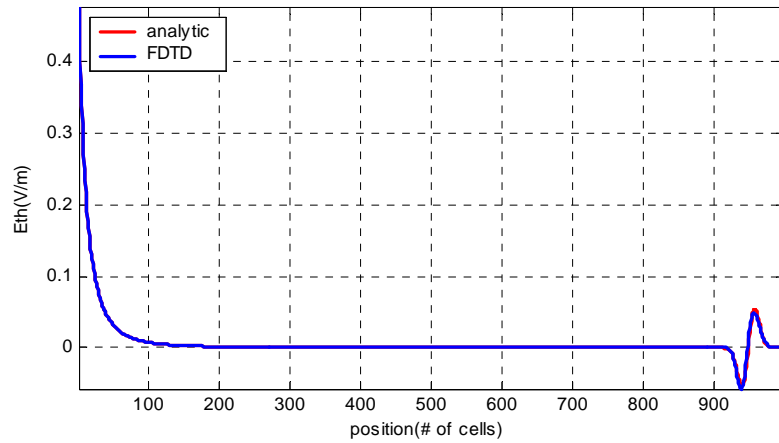


Figure 6-50: Propagating FDTD Gaussian response (*spatial*)

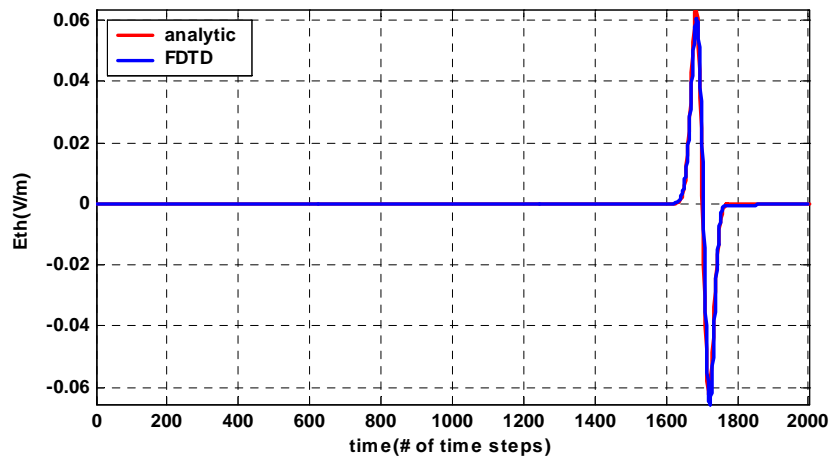


Figure 6-51: Propagating FDTD Gaussian response (*temporal, far field*)

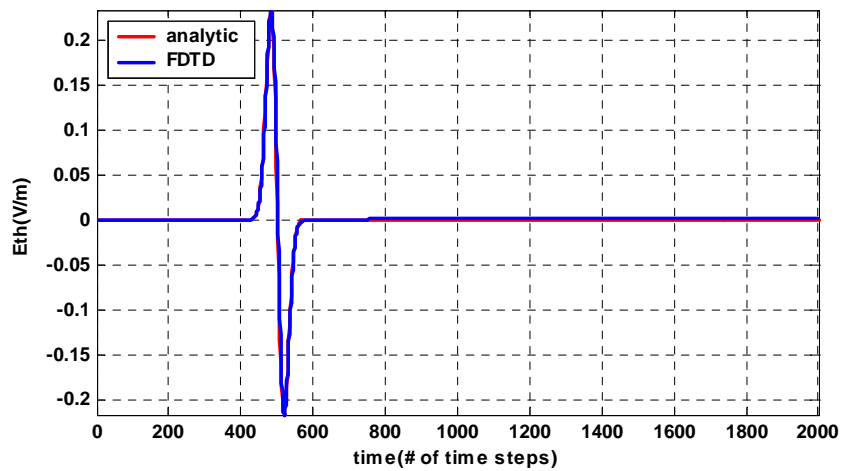


Figure 6-52: Propagating FDTD Gaussian response (*temporal, near field*)

Comparing Figure 6-47, Figure 6-48 with Figure 6-51, Figure 6-52, we find that distortion in the pulse is highly reduced for fine grid. Anyway we don't expect distortion in the near field pulse (Figure 6-49, Figure 6-52). Regarding above plots, an important remark could be that the grid structure in spherical coordinates used for this problem is very advantageous for FDTD due to the nature of problem. However, had we used standard Yee algorithm in Cartesian coordinates for FDTD, results would be worse.

### 6.4.3 RBTD Implementation

Now we repeat the simulations with novel method RBTD. We treat first ramp input and then Gaussian input. The grid structure is as shown in Figure 6-39, Figure 6-40 for wave fronts and rays and as described in Table 6-2.

**Determination of Discontinuities:** Recall that discontinuities are *finite jumps* in field quantities and their successive time derivatives. Then by inspection of Eqn(6.22), one can immediately determine discontinuities on the initial wave front where excitation is enforced. Since RBTD deals with only one of the field quantities (either  $\mathbf{E}$  or  $\mathbf{H}$ ), considering only  $\mathbf{E}$  field, the first discontinuity comes from step function term which is

$$\mathbf{A}_0(R, \theta) = [\mathbf{E}] = \frac{\sin \theta}{cR} \hat{\theta} \quad (6.26)$$

The second one comes from derivative of ramp function term, which is also a step.

$$\mathbf{A}_1(R, \theta) = \left[ \frac{\partial \mathbf{E}}{\partial t} \right] = \frac{2 \cos \theta}{R^2} \hat{\mathbf{R}} + \frac{\sin \theta}{R^2} \hat{\theta} \quad (6.27)$$

The last one is obtained by differentiating  $\mathbf{E}$  twice in time. That is, quadratic function turns out to be a step function and yields the third jump discontinuity.

$$\mathbf{A}_2(R, \theta) = \left[ \frac{\partial^2 \mathbf{E}}{\partial t^2} \right] = \frac{2c \cos \theta}{R^3} \hat{\mathbf{R}} + \frac{c \sin \theta}{R^3} \hat{\theta} \quad (6.28)$$

Note that successive differentiation produces no more discontinuities in the sense of jumps. By means of this *preprocessing*, we determine the discontinuities since we assume input field is known over the initial wave front before we start computation at  $t = 0$ . Alternative implementation methods are possible, for example, determination of discontinuities and propagation of them can be done in parallel synchronously like time-marching as the input signal samples are launched into the computational grid.

**Transport of Discontinuities:** Discontinuities are transported via transport equations along the rays (radial straight lines) in the computational grid. For isotropic, homogeneous medium ( $n = 1, \nabla n = 0$ ), then transport equations can be written as:

$$2 \frac{d \mathbf{A}_v}{d\tau} + \mathbf{A}_v \Delta_\mu \Psi = -c \nabla^2 \mathbf{A}_{v-1} \quad (6.29)$$

Noting that  $ds = n d\tau$ ,  $s = R$  and noting that  $\Delta_\mu \Psi = \nabla^2 \Psi = n^2 \nabla \cdot \mathbf{s} = 2/R$ , Eqn(6.29) becomes

$$\frac{d \mathbf{A}_v}{dR} + \frac{\mathbf{A}_v}{R} = -\frac{c}{2} (\nabla(\nabla \cdot \mathbf{A}_{v-1}) - \nabla \times \nabla \times \mathbf{A}_{v-1}) \quad (6.30)$$

Slope estimate method [101] has been utilized in the predictor-corrector sense such that

$$\begin{aligned} slope_{v1} &= \left. \frac{d \mathbf{A}_v}{dR} \right|_{i,k} = \left( \frac{\mathbf{A}_v}{R} - \frac{c}{2} (\nabla(\nabla \cdot \mathbf{A}_{v-1}) - \nabla \times \nabla \times \mathbf{A}_{v-1}) \right) \Big|_{i,k} \\ \mathbf{A}_{vpre} \Big|_{i+1,k} &= \mathbf{A}_v \Big|_{i,k} + slope_{v1} \Delta R \\ slope_{v2} &= \left. \frac{d \mathbf{A}_{vpre}}{dR} \right|_{i+1,k} = \left( \frac{\mathbf{A}_{vpre}}{R} - \frac{c}{2} (\nabla(\nabla \cdot \mathbf{A}_{(v-1)pre}) - \nabla \times \nabla \times \mathbf{A}_{(v-1)pre}) \right) \Big|_{i+1,k} \\ \mathbf{A}_v \Big|_{i+1,k} &= \mathbf{A}_{vcor} \Big|_{i+1,k} = \mathbf{A}_v \Big|_{i,k} + 0.5(slope_{v1} + slope_{v2}) \Delta R \end{aligned} \quad (6.31)$$

The right hand side of Eqn(6.30) is zero for  $\mathbf{A}_0$  and we have a simple ODE. In our implementation,  $\mathbf{A}_0$  is computed first throughout the computational domain. After having all  $\mathbf{A}_0$  available, then  $\mathbf{A}_1$  is computed throughout the computational domain with non-zero right-hand side. In a similar way  $\mathbf{A}_2$  is computed with non-zero right hand side. In all computations, slopes are calculated as described in Eqn(6.31). *Recursive* nature of transport equations make the computations of right-hand side cumbersome. Those right-hand sides are computed numerically using 2<sup>nd</sup> order accurate difference scheme in ray and transverse to ray directions. Next section presents the results for  $\mathbf{A}_{00}$ ,  $\mathbf{A}_{10}$ , and  $\mathbf{A}_{20}$  in coarse and fine grid.

### Coarse Grid:

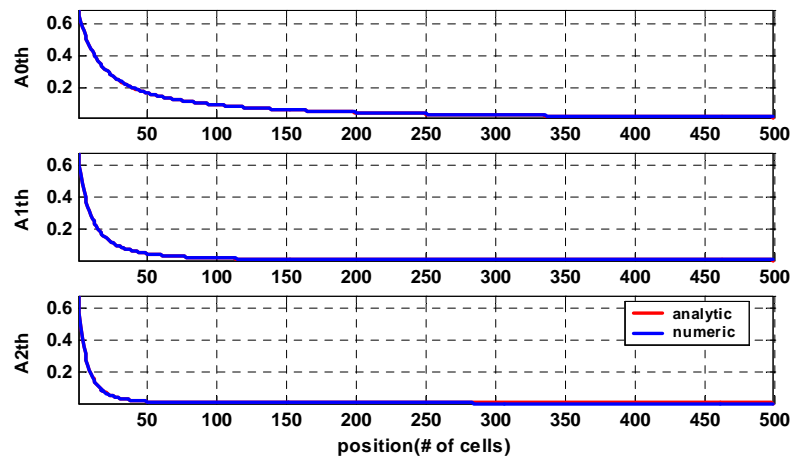


Figure 6-53: Transport of discontinuities ( $\mathbf{A}_{00}$ ,  $\mathbf{A}_{10}$ ,  $\mathbf{A}_{20}$ )

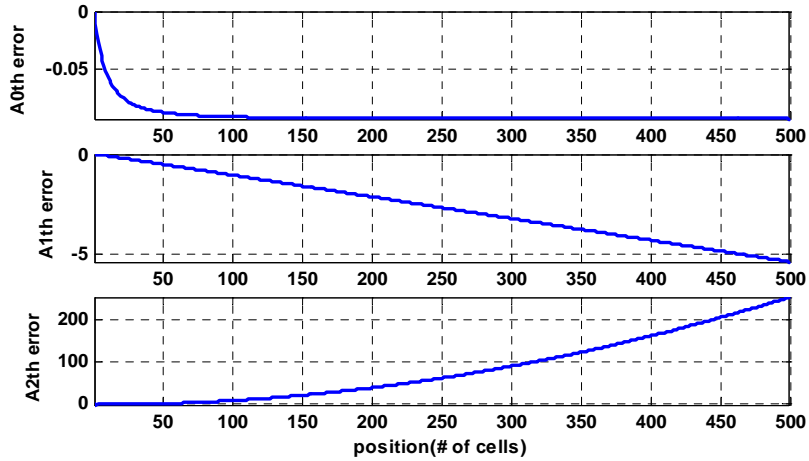


Figure 6-54: Percent error

Although the results in Figure 6-53 appears to be overlapped for analytical and numerical values, that does not depict the actual picture for small values. Figure 6-54 provides the percent error to asses the results. Numerical scheme transports  $\mathbf{A}_{00}$  very accurately, maximum error is almost %0.1 at the end of computational domain. But  $\mathbf{A}_{10}$  has some error (maximum %6) and  $\mathbf{A}_{20}$  has dramatic error (maximum %240). Error increases toward the end of computational domain or stating otherwise as the discontinuity propagates along ray. One of the source of error is the recursive nature of transport equations. Error in one stage inputs to the next stage. Moreover there are heavy numerical computations there, namely Laplace operator acting on a vector. The second one is the variation characteristics of discontinuities. Note from Eqns(6.26), (6.27), (6.28) that  $\mathbf{A}_{00}$ ,  $\mathbf{A}_{10}$ ,  $\mathbf{A}_{20}$  exhibit  $1/R$ ,  $1/R^2$  and  $1/R^3$  spatial variations. And the numerical scheme in Eqn(6.31) can not transport accurately higher order discontinuities due to their rapid variations. Better methods could be found. However we should not worry about this issue because higher order discontinuities decay rapidly and lose their effect at far field. They are essential to accurately compute time-dependent near field and we are already transporting them accurately in that region. We will turn back to this issue while discussing construction of time-dependent field from discontinuities.

## Fine Grid:

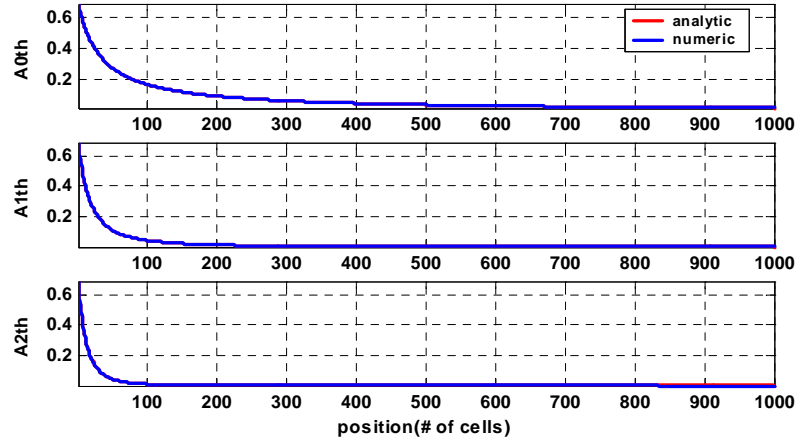


Figure 6-55: Transport of discontinuities ( $A_{00}$ ,  $A_{10}$ ,  $A_{20}$ )

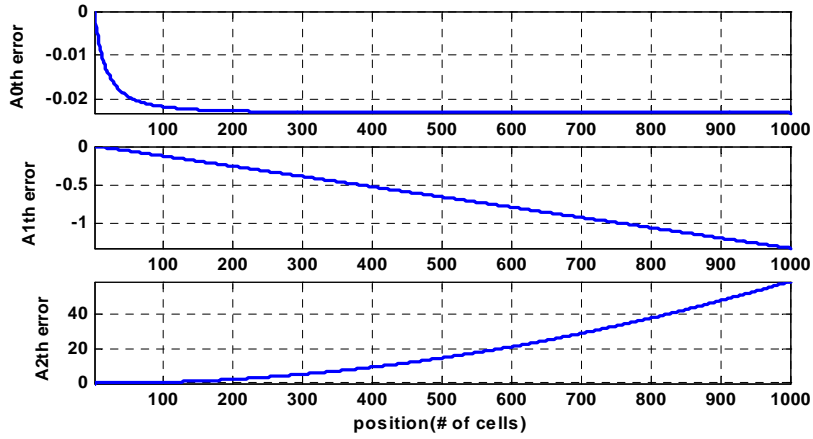


Figure 6-56: Percent error

From Figure 6-55, Figure 6-56, it is evident that fine grid performs well in transporting discontinuities. Errors are reduced by a factor of 4 or 5. This indicates us that numerical scheme is *consistent* with the actual transport equations because error tends to zero as grid spacings are reduced as described in Table 6-2. Note that in above plots  $A_{00}$ ,  $A_{10}$ ,  $A_{20}$  are normalized values, that is,  $A_{00}$  is multiplied by  $c$ ,  $A_{10}$  is as it is, and  $A_{20}$  is divided by  $c$ .

**Construction of Time-Dependent Field:** After having all discontinuities available at every grid point, we can directly construct time-dependent field at any point  $(i,k)$  of  $\mathbf{R}$ .

$$E(\mathbf{R}, t) = \begin{cases} A_0(\mathbf{R}) + A_1(\mathbf{R})(t - t_0) + A_2(\mathbf{R}) \frac{(t - t_0)^2}{2} & t \geq R/c \\ 0 & t < R/c \end{cases} \quad (6.32)$$

### 6.4.3.1 Ramp Pulse

We construct time-dependent field ( $E_\theta$ ) from discontinuities of ( $\mathbf{A}_{0\theta}$ ,  $\mathbf{A}_{1\theta}$ ,  $\mathbf{A}_{2\theta}$ ) utilizing Taylor series. For this purpose results are presented at far field ( $i = 400$  and  $i = 800$ ) and near field ( $i = 100$  and  $i = 200$ ) during observation interval of  $500\Delta t$  and  $1000\Delta t$  for coarse and fine grid respectively. Our aspect angle is  $45^\circ$  measured from  $z$ -axis ( $k = 13$  for coarse and  $k = 26$  for fine grid). Recall that RBTD implements  $\Delta s = \Delta R = c\Delta t$ , CFL condition (magic time step), along rays. Thus in effect,  $\Delta t$  of RBTD is larger than the  $\Delta t$  of FDTD, so we need less for the same grid spacings ( $\Delta R$ ,  $\Delta\theta$ ).

#### Coarse Grid:

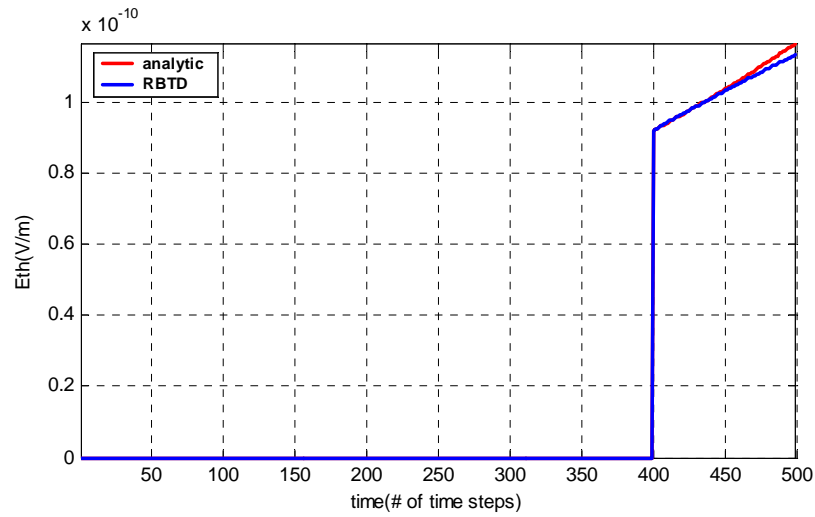


Figure 6-57: RBTD constructed ramp response (*far field*)

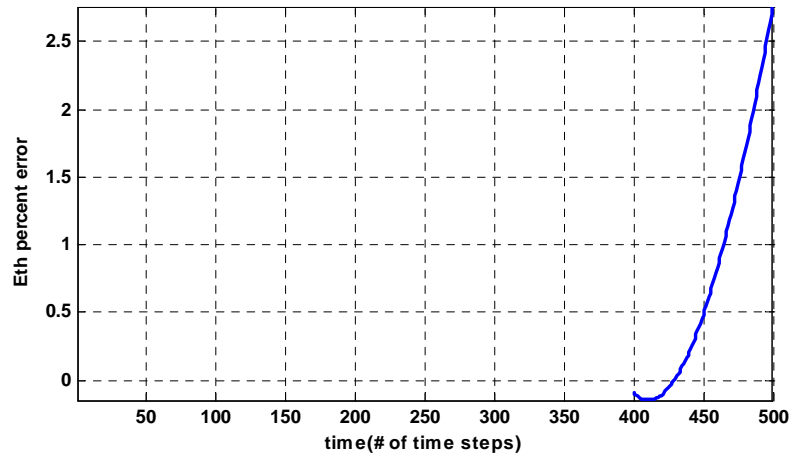


Figure 6-58: Percent error (*far field*)

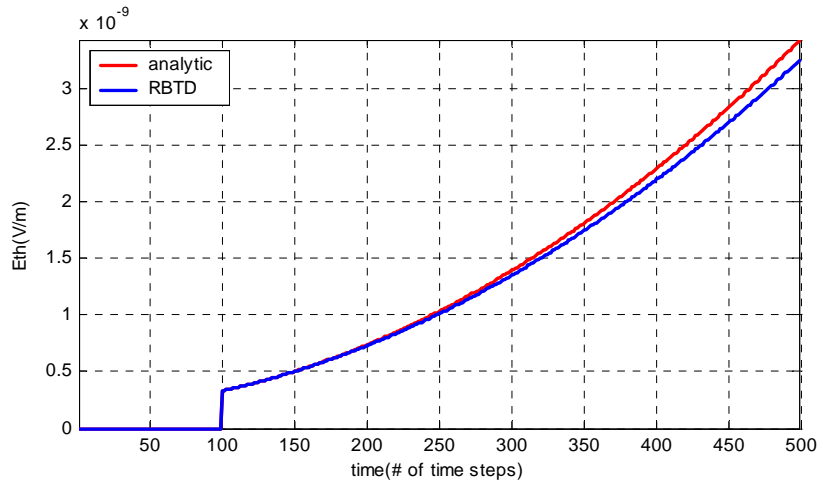


Figure 6-59: RBTD constructed ramp response (*near field*)

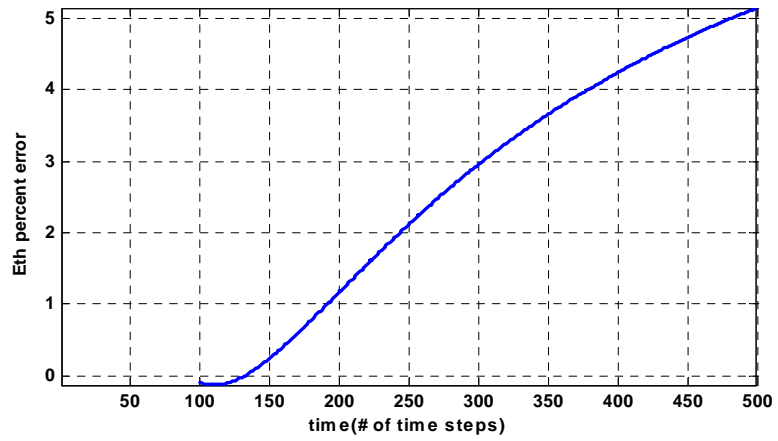


Figure 6-60: Percent error (*near field*)

**Fine Grid:**

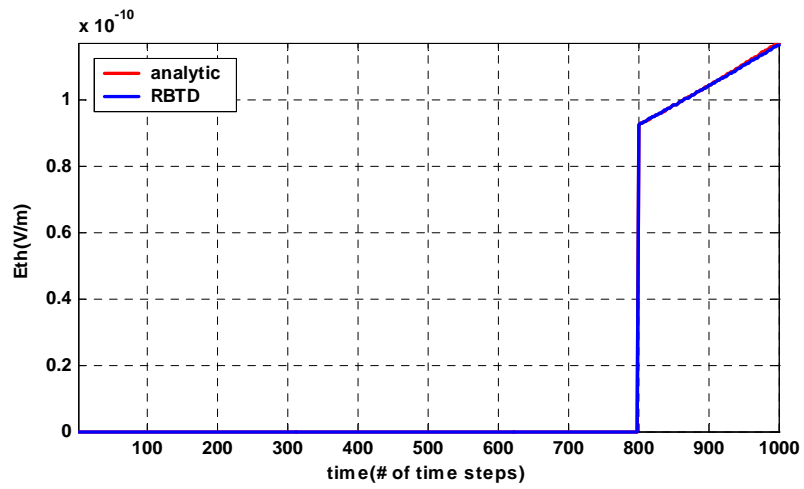


Figure 6-61: RBTD constructed ramp response (*far field*)

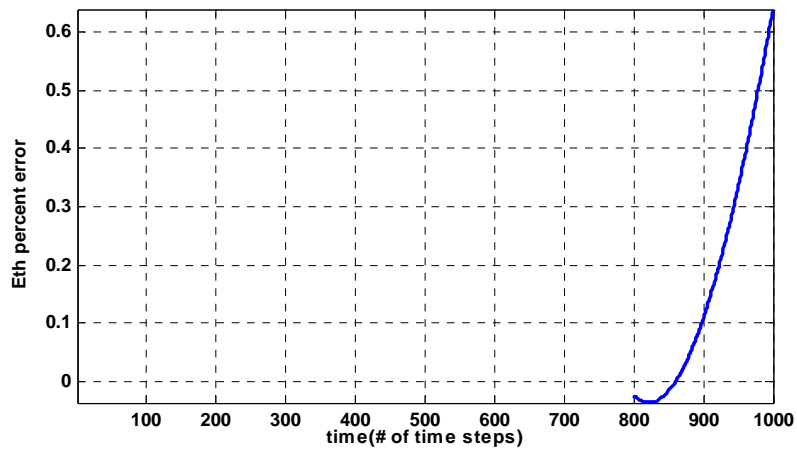


Figure 6-62: Percent error (*far field*)

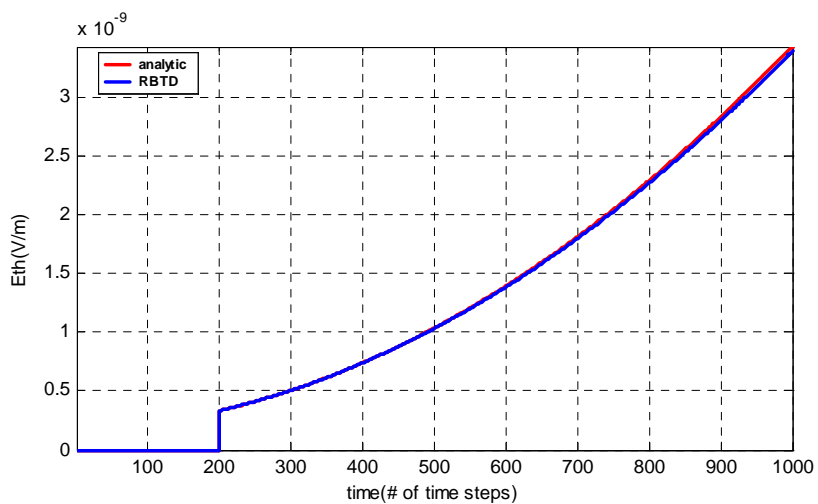


Figure 6-63: RBTD constructed ramp response (*near field*)

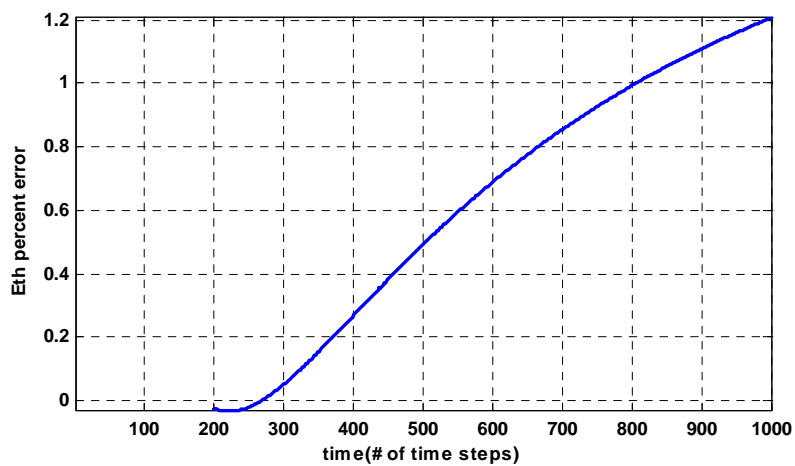


Figure 6-64: Percent error (*near field*)

Examining coarse grid plots (Figure 6-57, Figure 6-58, Figure 6-59, Figure 6-60) and fine grid plots (Figure 6-61, Figure 6-62, Figure 6-63, Figure 6-64), one can conclude that far constructed field exhibits some error if one sits at a point and makes *long* time observation because Taylor series expansion is an approximation in a neighborhood. Higher order discontinuities are not so accurately transported to far field by our numerical scheme. However there is an advantage that higher order discontinuities are weak, small coefficients of Taylor series at far field. Near field constructed datum are accurate. Both 0<sup>th</sup> order and higher order discontinuities are computed very accurately in that region. Thus, constructed time-dependent field is also accurate. Results also proves that fine grid is much better than coarse grid as expected.

### 6.4.3.2 Gaussian Pulse

In Sample Problem I and II. we have approximated Gaussian pulse by shifted rectangular pulses. By the same reasoning, since ramp response of Hertzian dipole has already been computed, then it is easy to construct the Gaussian response. For this purpose, input Gaussian pulse is approximated by ramp functions within  $\Delta t$  interval and Gaussian response is computed as the weighted sum of the shifted ramp responses. Both near/far field and spatial/temporal plots are presented in the next section under the same simulation parameters and conditions.

#### Coarse Grid:

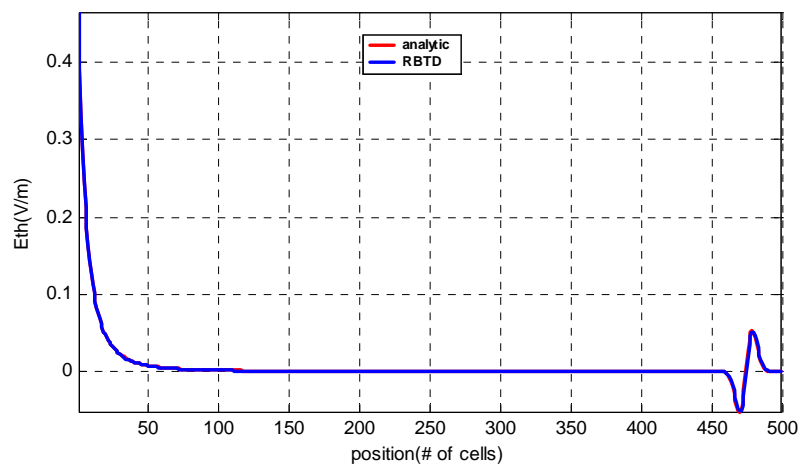


Figure 6-65: RBD constructed Gaussian response (*spatial*)

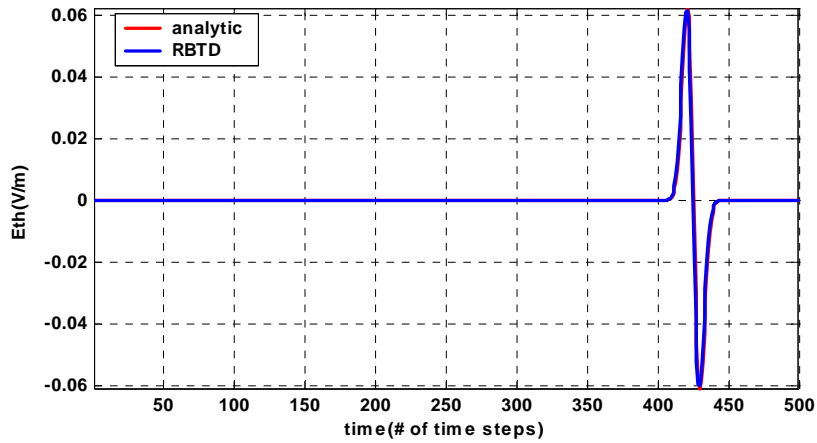


Figure 6-66: RBD constructed Gaussian response (*temporal, far field*)

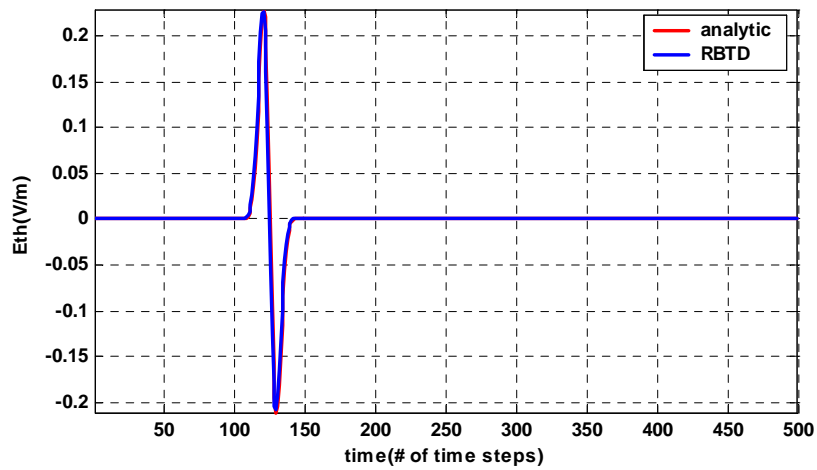


Figure 6-67: RBD constructed Gaussian response (*temporal, near field*)

**Fine Grid:**

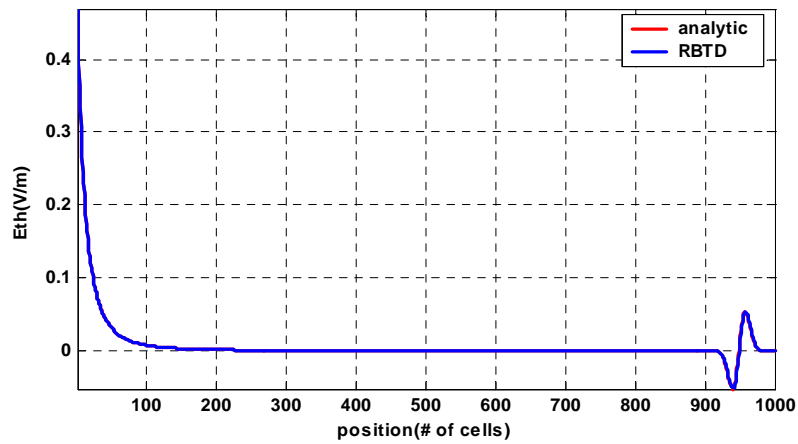


Figure 6-68: RBD constructed Gaussian response (*spatial*)

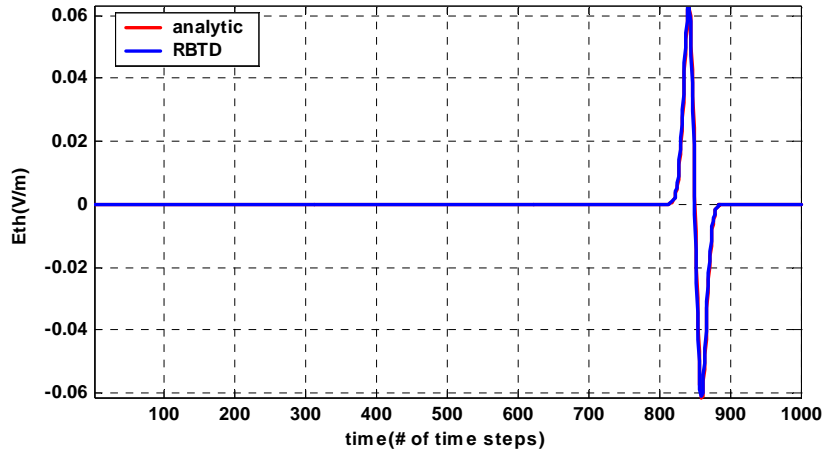


Figure 6-69: RBTD constructed Gaussian response (*temporal, far field*)

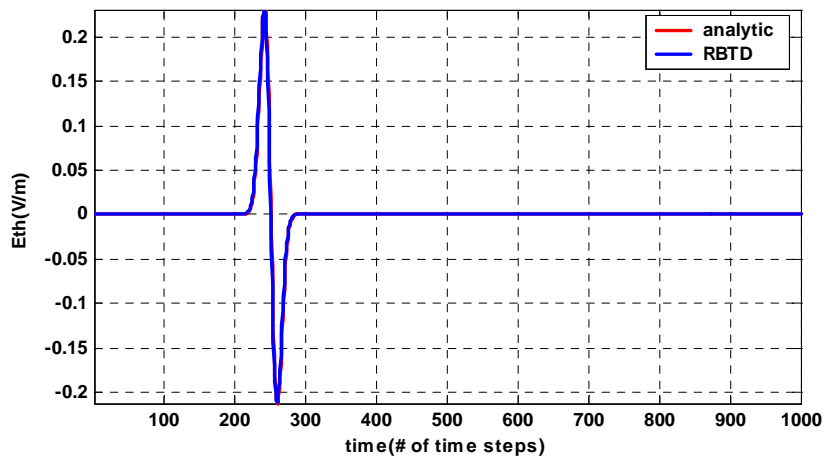


Figure 6-70: RBTD constructed Gaussian response (*temporal, near field*)

Comparing the RBTD plots with those of FDTD, It is certain that RBTD achieves what FDTD can not. There is no numerical dispersion either at far field or near field. As discussed in Section 5.4.3, our numerical scheme induces errors during the transport of higher discontinuities. But this error has nothing to do with numerical dispersion. It is just numerical computation error and better algorithms could be found. However This is not the purpose of this thesis study. Moreover, we conclude that their erroneous nature is not important at far field. As for near field, they are already computed very accurately and time-dependent near field is also constructed accurately. This is consistent with the understanding of frequency domain GO/GTD research. Dominek [104] tried to interpret the higher order terms in Luneburg-Kline series in Eqn (4.1). His study concluded that higher order terms in that expansion is not significant for propagation, reflection and refraction at some canonical

scattering surfaces such as spherical, cylindrical etc. It should also be mentioned that computational burden of RBTD is not heavier than that of FDTD. Simple physical facts on wave phenomena must be implemented wisely.

### 6.5 Sample Problem IV: Electric Dipole in Inhomogeneous Medium

Now we introduce inhomogeneity to Sample Problem III. To do this, considering Figure 6-39, Figure 6-40 we define a medium 2 having relative dielectric profile of

$$\varepsilon_r(z) = \begin{cases} 1 - (z+10)/5 & z \leq -10 \\ 1 & \text{elsewhere} \end{cases} \quad (6.33)$$

Note that  $\varepsilon_r$  has variation only in  $z$ -direction. At the boundary, continuity of  $\varepsilon_r$  is assured so that there exists no reflection. The medium 1 is free space ( $\varepsilon_0, \mu_0$ ). In real life,  $\varepsilon_r$  exhibits frequency dependence. We ignore this point for simulations because it creates no problem to demonstrate applicability of methods. Within the scope of this problem three simulations have been conducted: Firstly, *Spherical FDTD* implementation in standard spherical coordinates, secondly *Conformal FDTD* implementation in conformal grids and finally *RBTD* which already necessitates conformal gridding.

#### 6.5.1 Computational Grid

Computational grid for spherical FDTD is the one used in Sample Problem III (Figure 6-39, Figure 6-40) and as in Table 6-2. However, RBTD requires grid to conform wave fronts and rays. In this problem, wave fronts and rays remain same in medium 1 as in Sample Problem III but are bent toward  $z$ -axis, deformed in medium 2 (inhomogeneous) as depicted in Figure 6-71, Figure 6-72. We will use this grid structure for conformal FDTD simulations too.

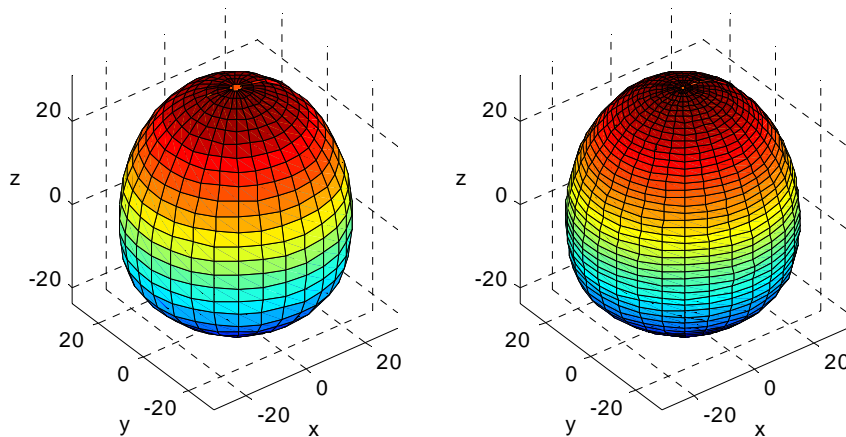


Figure 6-71: Wave fronts for coarse and fine grids.

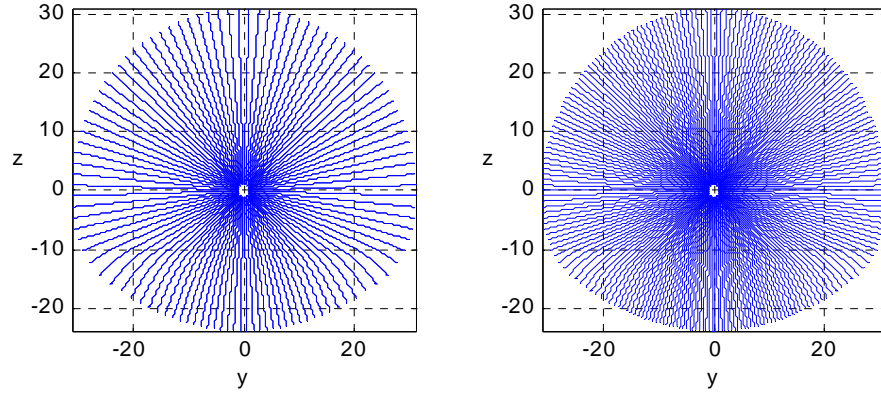


Figure 6-72: Rays on  $yz$ -plane for coarse and fine grids

### 6.5.2 Spherical FDTD Implementation

Taking into account medium parameters, field update equations Eqn(6.23) turn into Eqn(6.34).  $\Delta t$  is again set to its value by Eqn(6.25) according to homogeneous part of medium because smallest grid dimensions lie here on initial wave front. From now on, simulations are conducted only for Gaussian pulse. For inhomogeneous medium, we don't have analytical results in our hand, so we only provide numerical results and compare them.

$$\begin{aligned}
 E_{\mathbf{R}}^{n+1}(i,k) &= E_{\mathbf{R}}^n(i,k) + \frac{\Delta t}{\varepsilon_0 \varepsilon_r(i,k)} \left( \frac{\sin \theta(k) H_{\varphi}^{n+1/2}(i,k) - \sin \theta(k-1) H_{\varphi}^{n+1/2}(i,k-1)}{\sin \theta(k) R(i) \Delta \theta} \right) \\
 E_{\theta}^{n+1}(i,k) &= E_{\theta}^n(i,k) - \frac{\Delta t}{\varepsilon_0 \varepsilon_r(i,k)} \left( \frac{R(i) H_{\varphi}^{n+1/2}(i,k) - R(i-1) H_{\varphi}^{n+1/2}(i-1,k)}{R(i) \Delta R} \right) \\
 H_{\varphi}^{n+1/2}(i,k) &= H_{\varphi}^{n-1/2}(i,k) - \frac{\Delta t}{\mu_0 R(i)} \left( \frac{R(i+1) E_{\theta}^n(i+1,k) - R(i) E_{\theta}^n(i,k)}{\Delta R} \right. \\
 &\quad \left. - \frac{E_{\mathbf{R}}^n(i,k+1) - E_{\mathbf{R}}^n(i,k)}{\Delta \theta} \right)
 \end{aligned} \tag{6.34}$$

**Coarse Grid:** Figure 6-73, Figure 6-74 depict  $E_{\theta}$  in space at the end of observation time,  $1000\Delta t$ , for  $k$  values of 31, 36, 42, 47, and 49 in the 4<sup>th</sup> quadrant of  $yz$ -plane (Figure 6-40) of coarse grid.  $k=31$  radial line has no intersection with inhomogeneous medium in the computational domain. So wave on it never enters into inhomogeneous medium.  $k=36$ ,  $k=42$ ,  $k=47$ ,  $k=49$  radial lines (ray in homogeneous medium but not ray in inhomogeneous one) lie in both media. Recall that  $M=52$  for coarse grid in Table 6-2. Then  $k$  values and corresponding elevation angles are as follows.

Table 6-3:  $k$  values and corresponding elevation angles in coarse grid

$k(\text{integer})$	$0.6M = 31$	$0.7M = 36$	$0.8M = 42$	$0.9M = 47$	$0.95M = 49$
angle	$105^\circ$	$122^\circ$	$143^\circ$	$160^\circ$	$167^\circ$

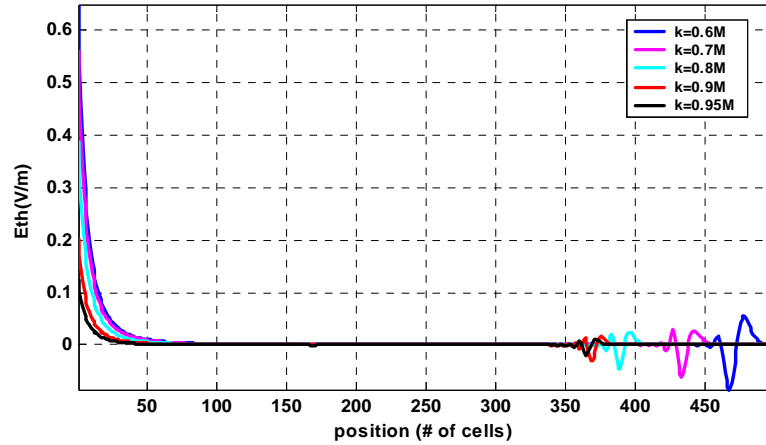


Figure 6-73: Spherical FDTD propagated Gaussian response (*spatial*)

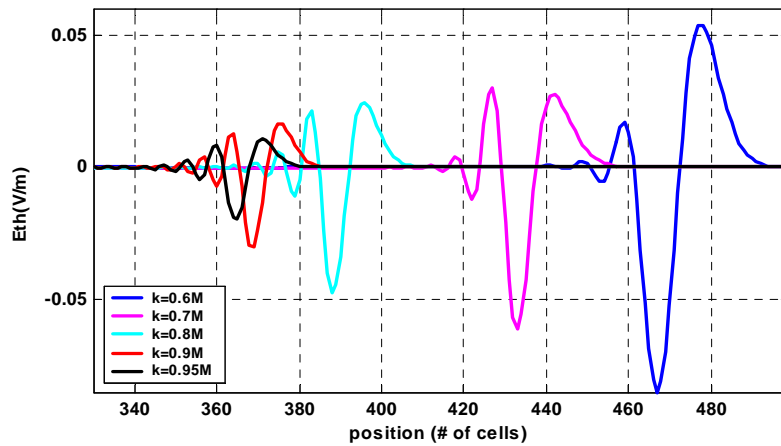


Figure 6-74: A closer look at the Gaussian response (*spatial*)

**Fine Grid:** Figure 6-75, Figure 6-76 depict  $E_\theta$  in space at the end of observation time  $k$  values and corresponding elevation angles for fine grid are shown in Table 6-4. Observation time is  $2000\Delta t$ . Recall that  $M = 105$  for fine grid in Table 6-2.

Table 6-4:  $k$  values and corresponding elevation angles in fine grid

$k(\text{integer})$	$0.6M = 63$	$0.7M = 74$	$0.8M = 84$	$0.9M = 95$	$0.95M = 100$
angle	$107^\circ$	$126^\circ$	$143^\circ$	$162^\circ$	$170^\circ$

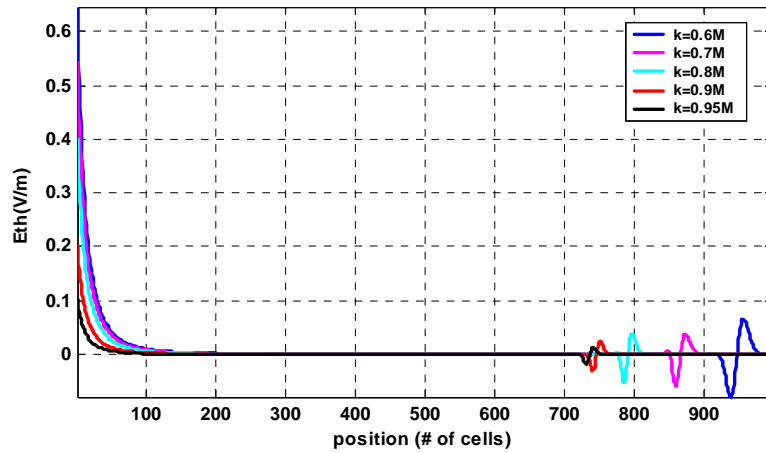


Figure 6-75: Spherical FDTD propagated Gaussian response (*spatial*)

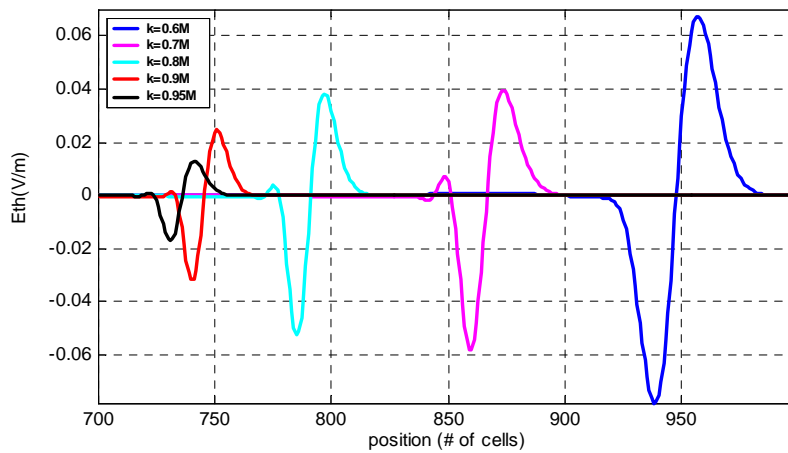


Figure 6-76: A closer look at the Gaussian response (*spatial*)

Waves in inhomogeneous medium is more distorted than homogeneous medium because propagation direction of wave changes continuously and approaches toward  $z$ -axis. Since spherical coordinate grids do not follow *ray bending* (propagation direction) in medium 2, wave is additionally more liable to numerical dispersion. Both *discretization* and *propagation direction* dependence contributes to numerical dispersion in this problem. Note that wave is compressed in inhomogeneous medium and it lags as it travels due to decreased phase velocity. Comparing with coarse grid results, it is understood that fine grid reduces distortion much while increasing computational complexity. Note that waves entering more obliquely to inhomogeneous medium exhibits more distortion ( $k = 36$ ,  $k = 42$  and  $k = 74$ ,  $k = 84$ ). Other waves ( $k = 47$ ,  $k = 49$  and  $k = 95$ ,  $k = 100$ ) enter into inhomogeneous medium close to normal incidence and their propagation direction changes are very smooth. Recall

from Section 2.6.2 that Teixeira [69] reported angle optimized FDTD algorithm to alleviate dependence of numerical dispersion on propagation direction. For that purpose, we have a new, better idea, which is *Conformal FDTD*, as by-product of this thesis.

### 6.5.3 Conformal FDTD Implementation

Formulation of FDTD in nonorthogonal curvilinear coordinate system was first introduced by Holland [50]. Then Fusco et.al [52], [53] provided FDTD implementation in curvilinear coordinates. Palandech, Mittra [54] generalized Fusco's approach. But this conformal gridding concept has been understood and used with FDTD to conform only the geometry of scatterer body in order to avoid staircase approximation. And people preferred standard FDTD algorithm in the rest of the computational domain. As we discussed earlier, our understanding of conformal grid in RBTD is the one *conforming to wave fronts and rays*. To the best of our knowledge, there has been no attempt to use such a grid for FDTD. We will see what is the meaning of this grid during simulations. Before proceeding further, let us introduce conformal grid structure. Results of [54] for our implementation can be summarized as follows. Each cell in the computational domain can be approximated as a parallelepiped in nonorthogonal curvilinear coordinates  $(u^1, u^2, u^3)$  as shown in Figure 6-77.

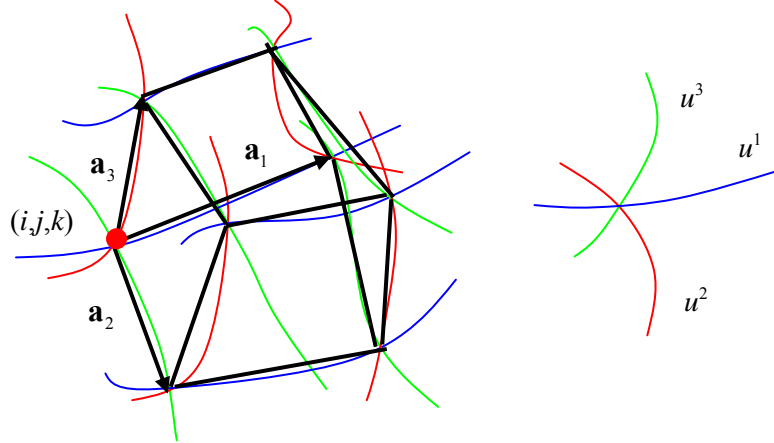


Figure 6-77: Oblique coordinate system and a typical cell

Sides of parallelepiped, the vectors  $(\mathbf{a}_1, \mathbf{a}_2, \mathbf{a}_3)$ , are called covariant basis vectors. Contra-variant basis vectors are defined as:

$$\mathbf{b}_1 = \frac{\mathbf{a}_2 \times \mathbf{a}_3}{V}, \quad \mathbf{b}_2 = \frac{\mathbf{a}_3 \times \mathbf{a}_1}{V}, \quad \mathbf{b}_3 = \frac{\mathbf{a}_1 \times \mathbf{a}_2}{V} \quad (6.35)$$

where  $V = \mathbf{a}_1 \cdot (\mathbf{a}_2 \times \mathbf{a}_3)$  is the volume of a cell (parallelepiped). The metric and inverse metric tensor also have the following elements respectively.

$$g_{ij} = \mathbf{a}_i \cdot \mathbf{a}_j, \quad h_{ij} = \mathbf{b}_i \cdot \mathbf{b}_j \quad (6.36)$$

Finally from Eqn(6.35), one can derive the relation  $\mathbf{a}_i \cdot \mathbf{b}_j = \delta_{ij}$  where  $\delta_{ij}$  is the Kronecker delta. In nonorthogonal coordinates,  $\mathbf{E}$  and  $\mathbf{H}$  are expressed by their covariant and contravariant components. For example,  $\mathbf{E}$  is expanded as:

$$\mathbf{E} = \sum_{i=1}^3 E_{b_i} \mathbf{a}_i = \sum_{i=1}^3 E_{a_i} \mathbf{b}_i \quad (6.37)$$

The coefficients of summation are called contravariant and covariant components of  $\mathbf{E}$  respectively. These components of any vector, say  $\mathbf{E}$ , can be obtained by

$$E_{b_j} = \mathbf{E} \cdot \mathbf{b}_j, \quad E_{a_j} = \mathbf{E} \cdot \mathbf{a}_j \quad (6.38)$$

One can also derive the relationship between these components as

$$E_{a_i} = \sum_{j=1}^3 g_{ij} E_{b_j}, \quad E_{b_i} = \sum_{j=1}^3 h_{ij} E_{a_j} \quad (6.39)$$

After discretizing Maxwell's equations, similar to spherical FDTD but now with slight differences, we end up with the following update equations in terms of covariant and contravariant components of  $\mathbf{E}$  and  $\mathbf{H}$ . Although we have introduced inhomogeneity in along  $z$ -axis, we can still utilize the  $\phi$ -axis symmetry and work on only  $yz$ -plane.

$$\begin{aligned} E_{b_1}^{n+1}(i,k) &= E_{b_1}^n(i,k) + \frac{\Delta t}{\varepsilon_0 \varepsilon_r(i,k) V(i,k)} \left( H_{a_3}^{n+1/2}(i,k) - H_{a_3}^{n+1/2}(i,k-1) \right) \\ E_{b_2}^{n+1}(i,k) &= E_{b_2}^n(i,k) - \frac{\Delta t}{\varepsilon_0 \varepsilon_r(i,k) V(i,k)} \left( H_{a_3}^{n+1/2}(i,k) - H_{a_3}^{n+1/2}(i-1,k) \right) \\ H_{b_3}^{n+1/2}(i,k) &= H_{b_3}^{n-1/2}(i,k) - \frac{\Delta t}{\mu_0 V(i,k)} \left( \begin{aligned} &E_{a_2}^n(i+1,k) - E_{a_2}^n(i,k) \\ &E_{a_1}^n(i,k+1) - E_{a_1}^n(i,k) \end{aligned} \right) \end{aligned} \quad (6.40)$$

Note that in this general nonorthogonal space,  $\Delta u^i$  are effectively 1 since the physical edge lengths are incorporated in covariant basis vectors and thus  $\Delta u^i$  are included in  $V(i,k)$ . This formulation is much more general because basis vectors are cell dependent and coordinates can be deformed in a general manner. The right-hand sides of Eqn(6.40) involve the covariant components of  $\mathbf{E}$  and  $\mathbf{H}$ , whereas the components being time-stepped are contravariant components. Once the time-dependent contravariant fields are computed, they can be mapped back to the physical space. Using this grid structure conforming to wave fronts and rays, we have made simulations for both coarse and fine grid. The terms, 'coarse' and 'fine' grid, still pertain to homogeneous part of medium where  $z \geq -10\text{m}$  and as

described in Table 6-2. Please keep in mind that the medium is inhomogeneous for  $z < -10m$  with the given permittivity profile in Eqn(6.33).  $\Delta t$  is selected to be same as with that of spherical FDTD since smallest cells lie in homogeneous part of medium on the initial wave front.

**Coarse Grid:** Figure 6-78, Figure 6-79 illustrate the results for  $E_\theta$  on a wave front  $i = 400$  for different  $k$  values of Table 6-3. The observation duration is  $1000\Delta t$ . Observation points on the 400<sup>th</sup> wave front, of course, have different radial distance from the origin contrary to spherical FDTD case because wave fronts and rays are deformed due to permittivity profile and grid conforms to it, that is grid follows *ray bending* (propagation direction). Also note that angles corresponding to  $k$  values are valid for homogeneous part where rays are radial lines.

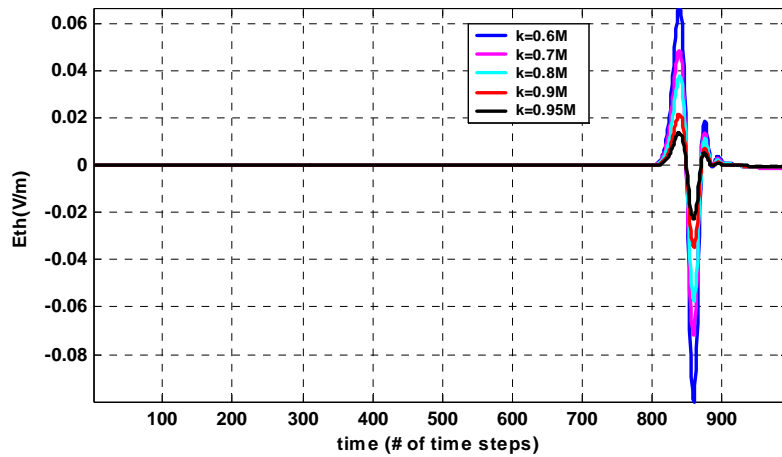


Figure 6-78: Conformal FDTD propagated Gaussian response (*temporal*)

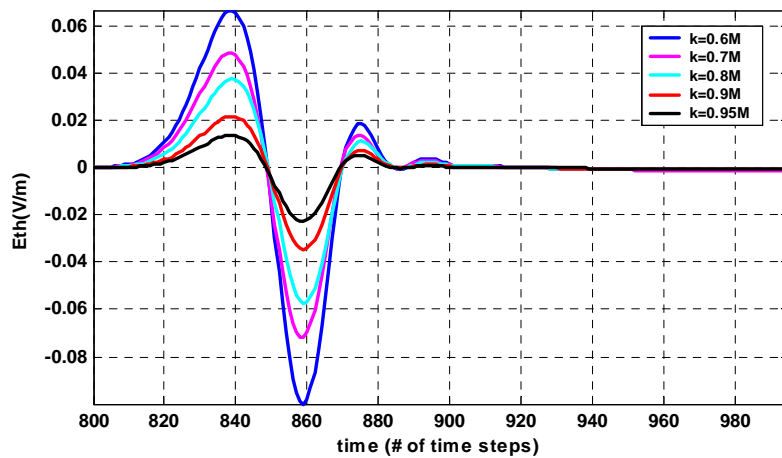


Figure 6-79: A closer look at the propagating Gaussian response (*temporal*)

Waves are lined up and experience the same type of dispersion error. There is no dependence on *ray bending* (propagation direction) because our conformal grid is aligned, oriented with it. This conformal grid approach to FDTD is completely new and eliminates dependence of numerical dispersion on propagation direction. It contributes directional property to FDTD which did not have that capability upto now. Then numerical dispersion stems only from PDE nature of FDTD and discretization of it. That can be removed by having ODE. This is what RBTD method achieves. *RBTD is both directional and ODEs-based*. If computation at the same grid points were done by spherical FDTD, we would have the next figure.

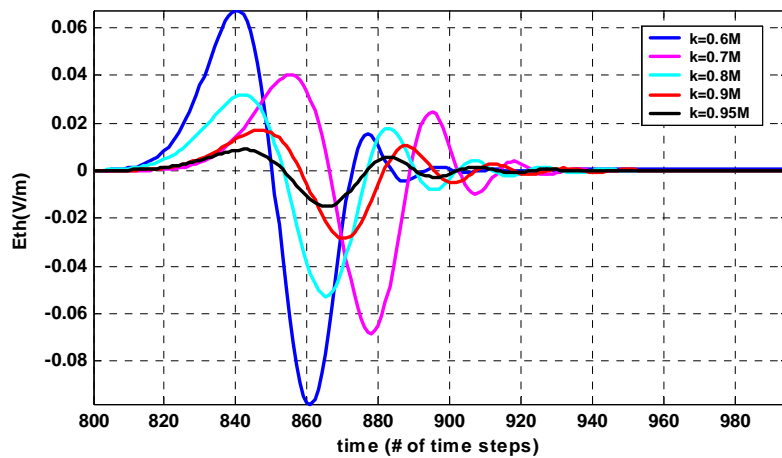


Figure 6-80: Spherical FDTD propagated Gaussian response (temporal)

**Fine Grid:** Similar to previous case, Figure 6-81, Figure 6-82 illustrate the results for  $E_\theta$  on a wave front  $i = 800$  for different  $k$  values of Table 6-4. The observation duration is  $2000\Delta t$ . The comments done for coarse grid totally apply to them but with an addition that fine grid performs better. Had we computed results by spherical FDTD at the same grid points, we would have Figure 6-83. In addition to that fine grid is, of course, better than coarse grid, same comments apply to following plots.

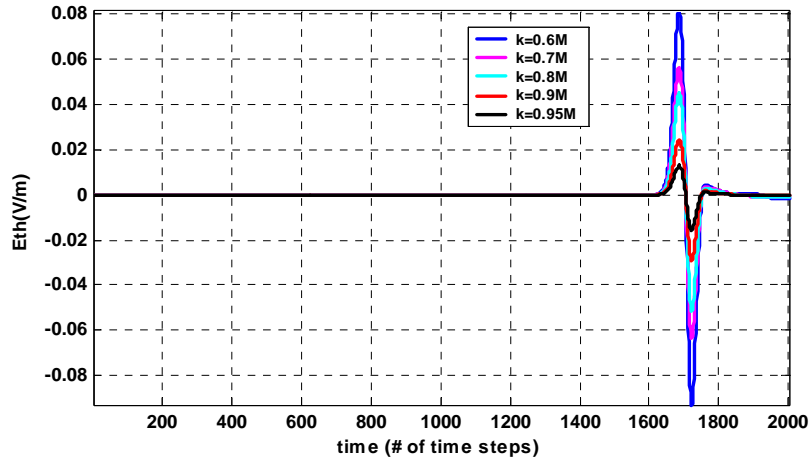


Figure 6-81: Conformal FDTD propagated Gaussian response (*temporal*)

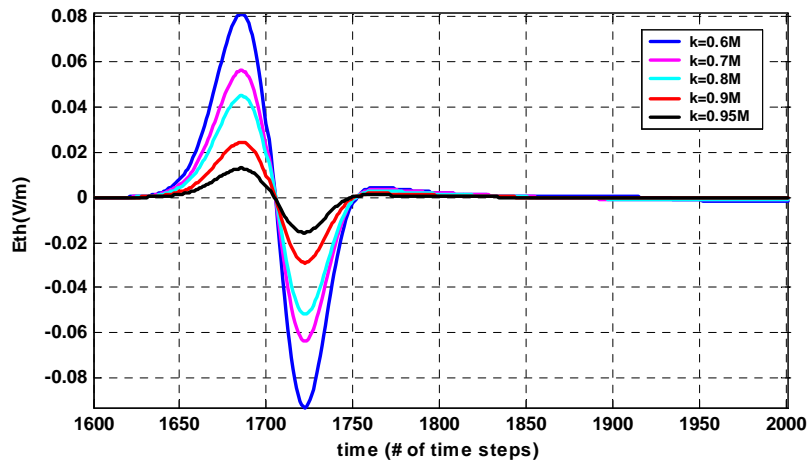


Figure 6-82: A closer look at the propagating Gaussian response (*temporal*)

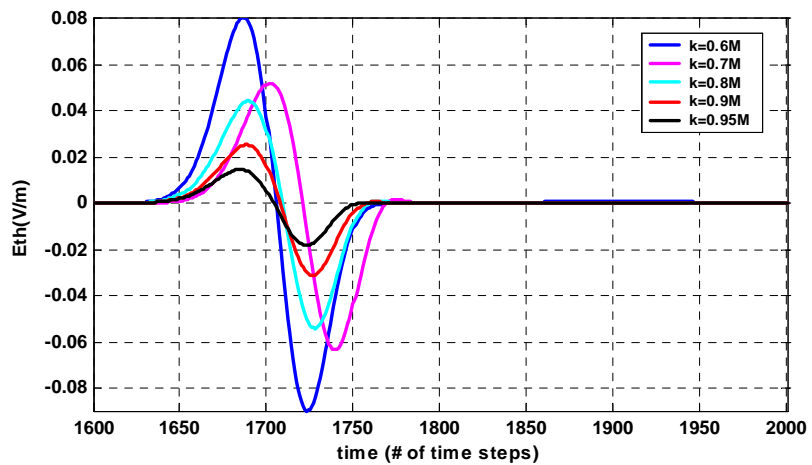


Figure 6-83: Spherical FDTD propagated Gaussian response (*temporal*)

#### 6.5.4 RBTD Implementation

In Section 5.4.3, after demonstrating construction of time-dependent near and far field, we have concluded that higher order discontinuities are negligible at far field but essential at near field. They have been transported accurately to near field but with some error to far field. However transport of 0<sup>th</sup> order discontinuity  $\mathbf{A}_0$  is very accurate everywhere. Its reflection, refraction can be performed easily and accurately as well. In this section, we deal with only  $\mathbf{A}_0$ , which is GO field term, to find the time-dependent the far field using covariant and contravariant components in nonorthogonal curvilinear *grid conforming to wave fronts and rays*, which is the requirement of RBTD.

**Determination of Discontinuities:**  $\mathbf{A}_0$  on the initial wave front (in homogeneous medium) is the same as in Sample Problem III.

$$\mathbf{A}_0(\mathbf{R}_0) = \frac{\sin \theta}{cR} \hat{\theta} \quad (6.41)$$

**Transport of Discontinuity:** The transport equation is

$$2 \frac{d\mathbf{A}_0}{d\tau} + \mathbf{A}_0 \Delta_\mu \Psi + \frac{2}{n} (\mathbf{A}_0 \cdot \nabla n) \nabla \Psi = 0 \quad (6.42)$$

This is homogeneous ODE. Using  $\Delta_\mu \Psi = (n^2 \nabla \cdot \mathbf{s} + n d\varepsilon/\varepsilon ds)$ , Eqn(6.42) becomes

$$2n \frac{d\mathbf{A}_0}{ds} + \mathbf{A}_0 \left( n^2 \nabla \cdot \mathbf{s} + \frac{nd\varepsilon}{\varepsilon ds} \right) + \frac{2}{n} (\mathbf{A}_0 \cdot \nabla n) \nabla \Psi = 0 \quad (6.43)$$

$\nabla \Psi = \mathbf{p}$  is wave normal and indicates ray direction. Considering grid structure and typical cell in Figure 6-77, one can infer that  $\nabla \Psi$  is

$$\nabla \Psi = \mathbf{p} = n \mathbf{a}_1 / |\mathbf{a}_1| \quad (6.44)$$

And since  $\mathbf{p} \cdot \mathbf{s} = 1$ , this leads to

$$\mathbf{s} = \mathbf{a}_1 / n |\mathbf{a}_1| \quad (6.45)$$

Then transport equation turns out to be

$$\frac{d\mathbf{A}_0}{ds} + \frac{\mathbf{A}_0}{2} \left( n \nabla \cdot \mathbf{s} + \frac{d\varepsilon}{\varepsilon ds} \right) + \left( \frac{\mathbf{A}_0 \cdot \nabla n}{n} \right) \frac{\mathbf{a}_1}{|\mathbf{a}_1|} = 0 \quad (6.46)$$

$\nabla \cdot \mathbf{s}$  and  $\nabla n$  can be computed numerically in forward difference manner.

$$\begin{aligned} \nabla \cdot \mathbf{s} \Big|_{i,k} &= \frac{1}{V(i,k)} \left( \frac{V(i+1,k)}{n(i+1,k) |\mathbf{a}_1(i+1,k)|} - \frac{V(i,k)}{n(i,k) |\mathbf{a}_1(i,k)|} \right) \\ \nabla n \Big|_{i,k} &= (n(i+1,k) - n(i,k)) \mathbf{b}_1 + (n(i,k+1) - n(i,k)) \mathbf{b}_2 \end{aligned} \quad (6.47)$$

The last term in Eqn(6.46) has  $\mathbf{a}_1$ . Then  $\mathbf{A}_0$  must be expanded in contravariant components.

$$\mathbf{A}_0 = A_{0b_1} \mathbf{a}_1 + A_{0b_2} \mathbf{a}_2 \quad (6.48)$$

Finally we can write the point slopes as:

$$\frac{dA_{0b_1}}{ds} = -\frac{A_{0b_1}}{2} \left( \mathbf{n} \cdot \nabla \cdot \mathbf{s} + \frac{d\varepsilon}{\varepsilon ds} \right) - \left( \frac{\mathbf{A}_0 \cdot \nabla \mathbf{n}}{\mathbf{n} |\mathbf{a}_1|} \right), \quad \frac{dA_{0b_2}}{ds} = -\frac{A_{0b_2}}{2} \left( \mathbf{n} \cdot \nabla \cdot \mathbf{s} + \frac{d\varepsilon}{\varepsilon ds} \right) \quad (6.49)$$

Note that  $|\mathbf{a}_1|$  is the edge length of a cell along the ray and  $ds$  is arc length. Then  $\Delta s = |\mathbf{a}_1|$ . Hence using the same slope estimation and predictor-corrector method of Section 5.4.3, contravariant components can be computed as:

$$\begin{aligned} A_{0b_1}(i+1,k) &= A_{0b_1}(i,k) + \Delta s (0.5 \text{ slope } 1_{b_1}|_{i,k} + 0.5 \text{ slope } 2_{b_1}|_{i+1,k}) \\ A_{0b_2}(i+1,k) &= A_{0b_2}(i,k) + \Delta s (0.5 \text{ slope } 1_{b_2}|_{i,k} + 0.5 \text{ slope } 2_{b_2}|_{i+1,k}) \end{aligned} \quad (6.50)$$

They must be mapped back to physical space. For example,  $A_{0b_2}$  is similar to  $A_{0\theta}$  in spherical coordinates, hence mapping results in

$$A_{0\theta} = \sqrt{g_{22}} A_{0b_2} \quad (6.51)$$

**Coarse Grid:** Figure 6-84 depicts transported  $A_{0\theta}$ . Figure 6-85 is a closer view. Each ray (different  $k$  values in Table 6-3) enters into inhomogeneous medium at different positions (wave front locations) naturally.

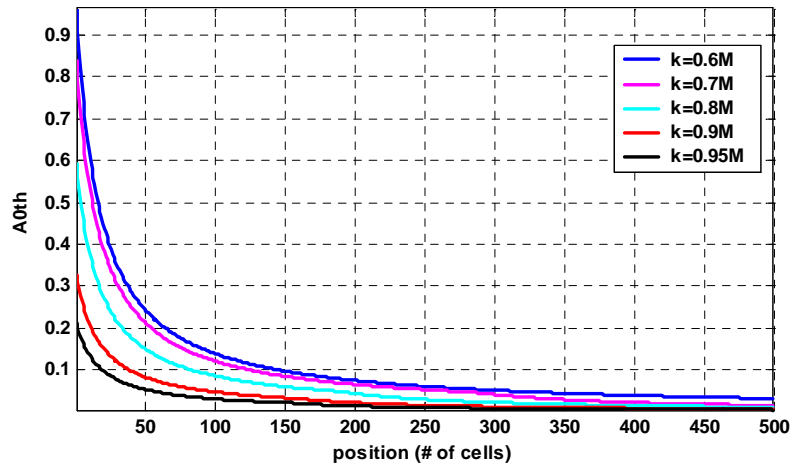


Figure 6-84: Transport of discontinuity  $A_{0\theta}$

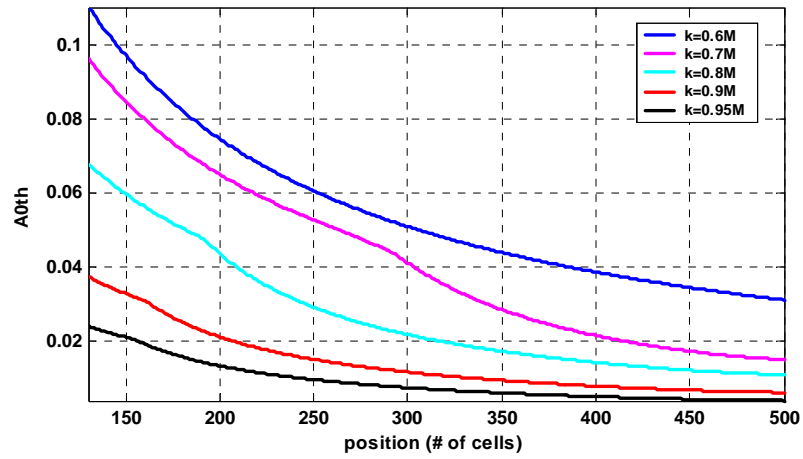


Figure 6-85: A closer look at  $A_{0\theta}$

**Fine Grid:** Figure 6-86 depicts transported  $A_{0\theta}$  for fine grid. Figure 6-87 is detailed view of  $A_{0\theta}$ . Different  $k$ -valued rays enter into inhomogeneous medium at different positions naturally.

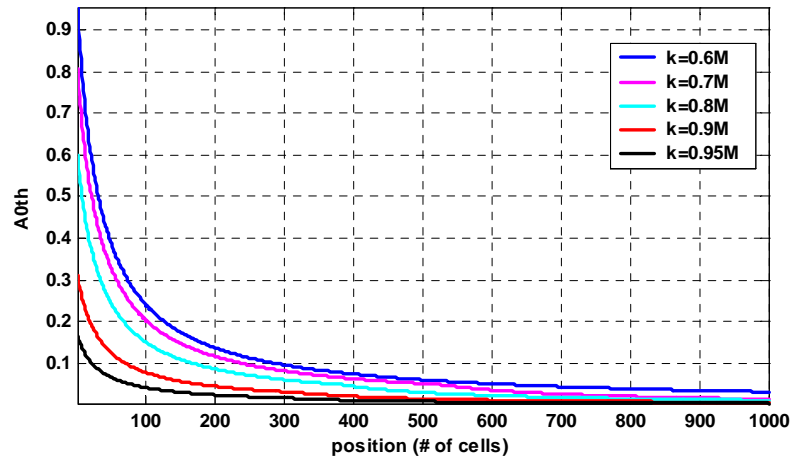


Figure 6-86: Transport of discontinuity  $A_{0\theta}$

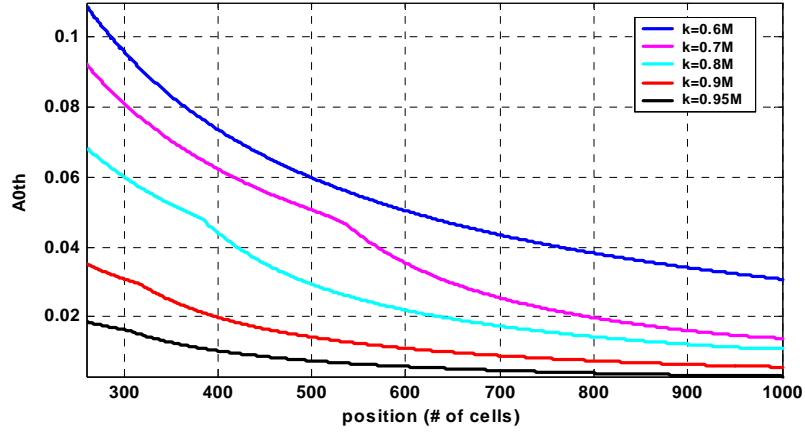


Figure 6-87: A closer look at  $A_{00}$

**Construction of Time-Dependent Field:** Using only GO field  $A_{0\theta}$ , time-dependent far field  $E_\theta$  can be constructed.

$$E_\theta(\mathbf{R}, t) = \begin{cases} A_{00}(\mathbf{R}) & t \geq t_i \\ 0 & t < t_i \end{cases} \quad (6.52)$$

$t_i$  corresponds to time associated with  $i^{\text{th}}$  wave front. On the  $i^{\text{th}}$  wave front, all the wave is in time-phase. Their variations are due to different  $k$ -values sitting on  $i^{\text{th}}$  wave front. For example, next we present constructed  $E_\theta$  at  $i = 400$  (coarse) and  $i = 800$  (fine) for different  $k$ -valued rays in the 4<sup>th</sup> quadrant of  $yz$ -plane. The observation interval is  $500\Delta t$  (coarse) and  $1000\Delta t$  (fine). Remember that RBTD uses  $\Delta s = \nu\Delta t$  along rays. Thus, physically no wave can exist at  $i = 400$  wave front for all  $k$ -valued rays before  $t_i = 400\Delta t$ . The same comment applies to fine grid with  $i = 800$  and  $t_i = 800\Delta t$ .

Coarse Grid:

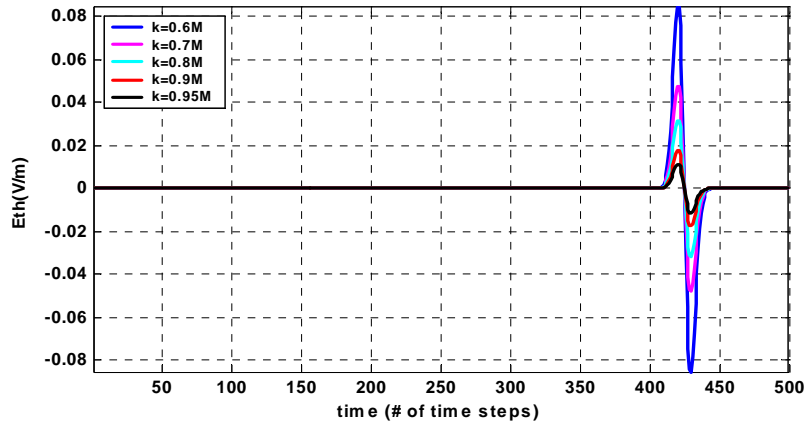


Figure 6-88: RBTD constructed Gaussian response (*temporal*)

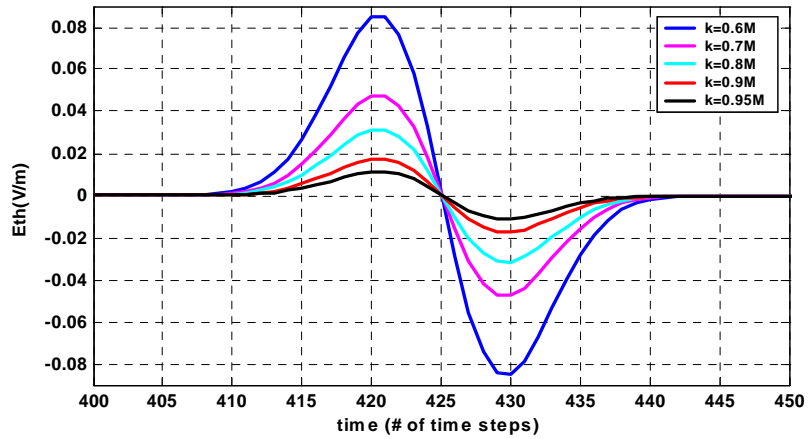


Figure 6-89: A closer look at the Gaussian response (*temporal*)

Fine Grid:

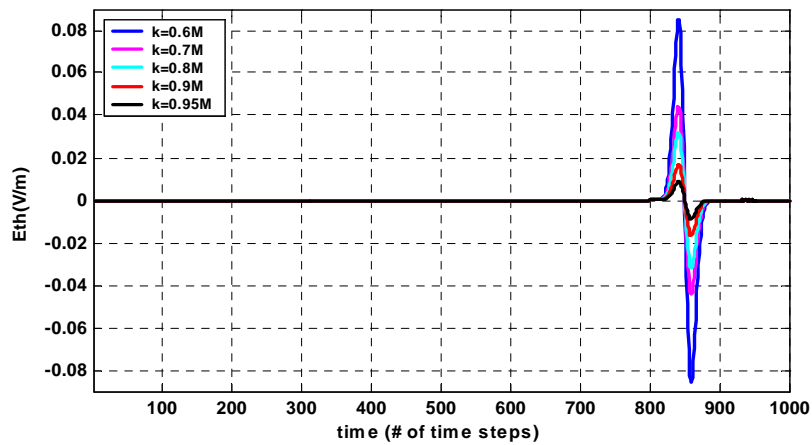


Figure 6-90: RBTD constructed Gaussian response (*temporal*)

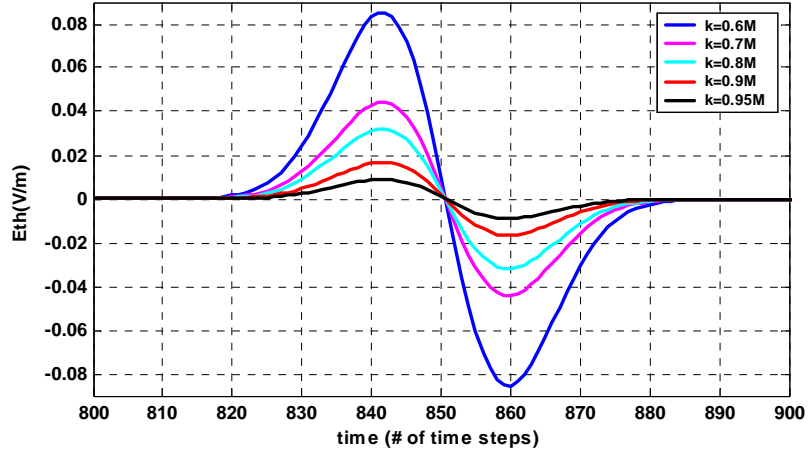


Figure 6-91: A closer look at the Gaussian response (*temporal*)

Figure 6-88, Figure 6-89 depict the constructed  $E_0$  for coarse grid while Figure 6-90, Figure 6-91 depict the constructed  $E_0$  for fine grid. RBTD excels in performance even Conformal FDTD. As stated earlier, RBTD is directional and ODEs-based. Thus, main sources of numerical dispersion have been eradicated. The only source of error in RBTD may stem from numerical computations.

## 6.6 Stability of Transport Equations

Transport equations in Eqn(5.12) for discontinuities are  $1^{st}$  order *Ordinary Differential Equations (ODEs)* and *recursive*. They reduce to homogeneous equations for  $0^{th}$  order discontinuity and non-homogeneous equations for higher order ones. The stability analysis of these  $1^{st}$  order ODEs is neither the aim nor within the scope of this thesis. That study has been well established and is available in many textbooks, for example [101]. Anyway, this issue is not a problem for RBTD as demonstrated by simulations.

## 6.7 Grid Generation

One of the peculiarity of RBTD is to generate computational grid conforming to wave fronts and rays in the medium as accurately as possible. Since computations start from a given initial wave front, consider a surface patch on it. First we find tangential vectors in transverse directions ( $\mathbf{T}_1$  and  $\mathbf{T}_2$ ) by fitting a circle to neighboring points (4,5,2) for  $\mathbf{T}_1$  and to neighboring points (1,5,3) for  $\mathbf{T}_2$ . Then we find the wave normal direction  $\mathbf{N}$ , which is the ray direction, by  $\mathbf{T}_2 \times \mathbf{T}_1$ . Finally next grid points are generated by going in ray direction by  $\Delta s = v \Delta t$  amount where  $\Delta s$ ,  $v$ , and  $\Delta t$  are arc length traversed, phase velocity at the point of

interest, and time step chosen. Repeating this procedure at each step, computational grid is created. Note that in RBTD, this is just like a 1-D wave motion along ray although the problem is higher dimensional.

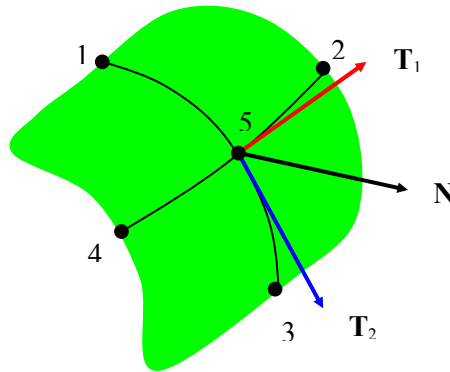


Figure 6-92: Grid generation

## 6.8 Accuracy of RBTD

The accuracy RBTD relies on the accuracy of grid generation, which must conform to wave fronts and rays, and the accuracy of finite difference solution of transport equations. Hence, for RBTD simulations upto here, a question may arise as to how accurate we generate our grid on which numerical computations are done. Grid can be generated perfectly in homogeneous medium starting from an initial wave front as in Sample Problem I, II and III. However, in inhomogeneous medium, depending on the nature of medium parameters and shape of initial wave front (degree of smoothness), there may be some errors. As an example, let us discuss Sample Problem IV. Permittivity profile has been defined in Eqn(6.33). Using it, the exact equation of rays on  $yz$ -plane can be written [3] as:

$$y(z) = \int_{z_0}^z \frac{ad\gamma}{\sqrt{(n(\gamma))^2 - a^2}} \quad (6.53)$$

Figure 6-93, Figure 6-94 depict the numerical rays generated by our grid generation procedure for RBTD and analytical rays computed by Eqn(6.53) Even for coarse case, results are excellent in inhomogeneous part of the medium. They overlap. Hence we can trust on accuracy of grid structure.

As for the accuracy of finite difference solution of transport equations, we have already discussed the accuracy of numerically computed discontinuities and their effects in Sample

Problem III. Results for  $\mathbf{A}_0$  was excellent everywhere in the computational domain. Transport equation of  $\mathbf{A}_0$  is homogeneous ODE and it can easily be solved for many physical permittivity profile. Higher order discontinuities have been transported accurately to near field but with an appreciable error to far field. Better numerical schemes could be found but this issue again is not the purpose of this thesis. Moreover, it has been concluded that higher order discontinuities are not significant in the far field. They are essential in the near field and they have been transported accurately to that region of computational domain. For this reason, only  $\mathbf{A}_0$  has been considered in Sample Problem IV for far field computations and results have been very accurate without loss of any information. Then it is claimed that RBTD computations are highly accurate.

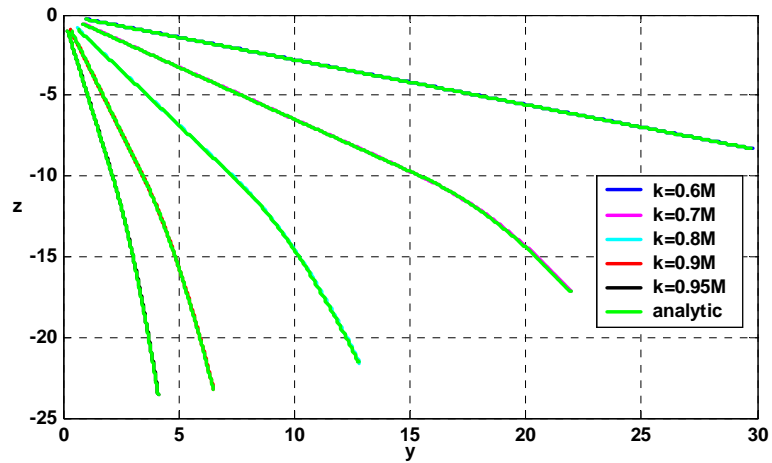


Figure 6-93: Analytical and numerical rays (coarse grid)

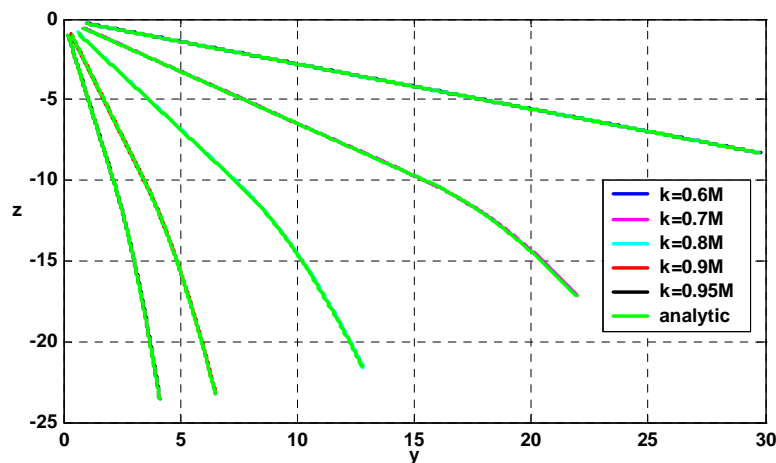


Figure 6-94: Analytical and numerical rays (fine grid)

## CHAPTER 7

### CONCLUSION

#### 7.1 Conclusion

We have started this study with motivation of developing dispersion free numerical algorithms for FDTD. Many aspects of FDTD and characteristic-based methods have been examined and finally we ended up with novel method, called RBTD by us, for the computation of time-dependent electromagnetic fields.

Although characteristic-based methods have many advantageous such as well-posedness, directional signal propagation, which improves the stability and numerical dispersion performance, the coefficient matrix cannot be diagonalised in higher dimensions. FDTD is very popular method for EM simulations and is widely used. It utilizes both  $\mathbf{E}$  and  $\mathbf{H}$  fields. The main drawback of FDTD is inherent numerical dispersion. There are two main factors causing numerical dispersion: discretisation of PDE Maxwell's equations (grid resolution, wavelength, time step) and propagation direction of wave in the grid. FDTD yields exact analytical solution only for 1-D wave and at CFL = 1 condition. Otherwise there always exists numerical dispersion. In Chapter 6, we have devised a novel grid structure conforming to wave fronts and rays (natural grid of RBTD) for FDTD and observed that this approach removes dependence of numerical dispersion to propagation direction because grid has been aligned to follow ray direction. Then numerical dispersion only due to discretization of PDE remains left. Although some researchers reported some angle optimized algorithms to alleviate numerical dispersion due to propagation direction and EM community used conformal gridding to conform the body of a scatterer, conformal gridding in the sense of wave fronts and rays for FDTD has been developed and implemented first in this thesis.

Contrary to FDTD, RBTD works on one of the field quantities, either  $\mathbf{E}$  or  $\mathbf{H}$ . RBTD is, in fact, also based on characteristic theory of PDEs. The grid structure of RBTD has to be wave fronts and rays, which are the characteristics and bicharacteristics of PDEs. RBTD deals with discontinuities of field quantities, transport of them along rays (incident, reflected, refracted), and reflection/refraction of them at a boundary interface. After RBTD computes

discontinuities in the computational domain, then it constructs time-dependent field by using Taylor series with coefficients being discontinuities transported to the point of interest. Thus RBTD preserve the advantageous of characteristic-based methods but does not deal with any matrix diagonalisation. Honoring directional signal propagation and ODE nature of transport equations provide to eliminate numerical dispersion, which is the biggest advantage of RBTD over FDTD. In Chapter 6, RBTD has been successfully applied to numerous EM problems in isotropic homogeneous/inhomogeneous medium (propagation, refraction, reflection). The same simulations have also been conducted for FDTD and results show that RBTD is superior to FDTD. RBTD not only eliminates *numerical dispersion* and *superluminal effects* of FDTD but we also believe it to be a completely new computational method in electromagnetic society.

Although rigorous analysis and study of stability of transport equations has not been undertaken, it can be inferred from the theory of ODEs that stability requirement of ODEs is less stringent than the stability requirement of PDEs. Thus we don't consider it to be a problematic issue for RBTD while FDTD algorithm has to satisfy CFL stability condition. RBTD implements  $\Delta s = v\Delta t$  1-D CFL condition (*magic time step*) along the rays. No matter what the dimension of problem is, it is treated as 1-D by RBTD.

FDTD needs ABCs at the end of the computational domain as discussed in Chapter 3. Improper termination causes unrealistic results. However RBTD does not require ABCs. RBTD implementation in Chapter 6 assumed a given input on the initial wave front. Performing some pre-processing, discontinuities have been determined and transported into computational domain as a spatial problem only. Hence no need to apply ABCs.

The presented theory of RBTD handles propagation, reflection and refraction of finite jump discontinuities. This is the condition for the convergence of Taylor series expansion. Otherwise series would diverge.

As far as the type of input waveform is concerned, there is no limitation for RBTD (smooth or discontinuous) whereas FDTD needs smooth excitations. However it is preferable to find the solution first for simple waveforms such as step, ramp or rectangular pulses. Then one can construct the response to an arbitrary waveform from the response of simpler waveform with the desired accuracy but depending on the accuracy of response of the simpler waveform. Considering only one period of waveform, one can treat even sinusoidal input.

## 7.2 Further Study

We believe RBTD to be very promising method. In future, following potential studies can be conducted so that RBTD gets mature and is widely used both in electromagnetics and in other branches of science for the solution of engineering problems.

- Better numerical methods to transport higher order discontinuities accurately can be further explored and found.
- RBTD can immediately be applied to ionospheric propagation and MUF calculation problems.
- Although we have given intuitively a sample treatment of 1<sup>st</sup> order discontinuity for reflection and refraction in Chapter 4, there is no neat, explicit formulas, like Fresnel formulas for GO fields, to determine reflected and refracted higher order discontinuities at discontinuous medium interface. This formulation can be further elaborated.
- For some problems, use of RBTD may be advantageous in some region while another method may be advantageous in the other region. Therefore hybridization of RBTD with other numerical methods can be considered.
- For some phenomena in electromagnetics, such as evanescent modes in waveguide, physical wave fronts and rays cannot be defined as in this study. To overcome this difficulty, complex-ray definition can be developed and RBTD formulation can be modified accordingly.
- Transport equations in RBTD have been implemented using finite differences. In Chapter 4, we have also provided the solution based on transport of energy terms related with discontinuities on a cross section of wave front. RBTD implementation, transporting energy terms in ray tubes, can also be demonstrated. Energy based implementation may exhibit better performance.
- Since the present theory of RBTD treats finite jump discontinuities, one of the important phenomena of electromagnetics, diffraction, cannot be handled. Infinite discontinuities resulting from caustic, foci points create diffracted field and make Taylor series go to infinity. So treatment of infinite discontinuities will add an important feature to RBTD. Incorporation of diffraction phenomenon by RBTD may lead to establishment of 3-D time domain theory of diffraction called ‘paragon=big problem’ in electromagnetics. In frequency domain, GO/GTD people neglect higher order terms in Luneburg-Kline series (as we did in Chapter 5 for Taylor series). They first obtain GO solution (the first term), then find the diffracted field from canonical problems of GTD and finally bring them together for total

solution. In our future study, we expect to follow the same reasoning and procedures in time domain to extend the RBTD.

- Problems in dispersive medium, where medium parameters changes with frequency are important in electromagnetics. FDTD solves them using convolution type integrals. This capability can be added to RBTD.
- Recall that in isotropic medium, wave normal and direction of energy propagation (ray direction) are parallel. Thus finding the wave normal in grid generation and transporting discontinuities in that direction means to follow energy flow. This thesis has dealt with isotropic medium. However in anisotropic medium, wave normal and ray directions are not parallel. Generation of wave fronts and rays need special care. Kline[92] provides the method how to transport GO field in anisotropic medium. But the method for higher discontinuities is not available. Due to these factors, developing the formulation and solving electromagnetic problems in anisotropic medium using RBTD is also considered to be a future study.
- Recall that there are there types of discontinuity hypersurfaces as mentioned in Chapter 3. In some problems, one must directly deal with source (charges and currents) to start the computation. During simulations we have assumed given input field on the initial wave front and treated stationary discontinuous boundary and propagating boundary separating zero/non-zero field regions. We have not treated discontinuous source boundary. This source boundary could be a wave front (Huygen's principle) or a non-wave front boundary (generator of wave fronts). In chapter 4, we have described how to determine ICs for discontinuities directly from source. Transport of these ICs from non-wave front source boundary to the nearest wave front is deferred to later studies.
- Transport equations for GO fields have an interesting and for some purpose useful interpretation if we consider their meaning in a special non-Euclidean geometry (Riemann geometry). GO fields move along the rays so that each remains parallel to itself in the sense of "*parallelism*" in Riemann geometry. In this "*parallel transfer*", GO field is said to be displaced parallel to itself if it satisfy a specific differential equation in Riemann geometry. And this differential equation is satisfied along special curves called *geodesic*. GO fields are parallel transferred along the rays when latter are regarded as geodesics in Riemann geometry. Hence RBTD concept may be applied/adapted to geodesic curves and geodesic flows which geophysics, magneto hydrodynamics deal with.
- Applicability of RBTD to fluid dynamics (Navier-Stokes equation), acoustics (acoustic wave equation) and quantum waves (Schrodinger equation) also needs to be explored.

## BIBLIOGRAHPY

- [1]. R.K. Luneburg, *Mathematical Theory of Optics*, Brown University Press, 1944.
- [2]. M. Kline, "An asymptotic solution of Maxwell's equations," *Comm. Pure Appl. Math.*, 4, 1951, pp.225-262.
- [3]. M. Kline, *The Theory of Electromagnetic Waves*, Dover Publication, 1951.
- [4]. J.B. Keller, "Geometrical theory of diffraction," *J. Optical Society of America*, vol.52, 1962, pp.116-130.
- [5]. R.G. Kouyoumjian, "Asymptotic high frequency methods," *Proc. IEEE*, vol.53, 1965, pp.864-876.
- [6]. R.G. Kouyoumjian, P.H. Pathak, "A uniform geometrical theory of diffraction for an edge in a perfectly conducting surface," *Proc. IEEE*, vol.62, 1974, pp.1448-1461.
- [7]. R.C. Hansen, *Geometrical Theory of Diffraction*, IEEE Press, NY, 1981
- [8]. R.F. Harrington, *Field Computation by Moment Methods*, NY, MacMillan, 1968.
- [9]. T.W. Veruttipong, "Time domain version of the uniform GTD," *IEEE Trans. AP*, vol.38, 1990, pp.1757-1764.
- [10]. E-Y Sun, W.V.T. Rusch, "Time domain physical optics," *IEEE Trans. AP*, vol.42, 1994, pp.9-15.
- [11]. P.R. Rousseau, P.H. Pathak, "Time domain uniform geometrical theory of diffraction for a curved wedge," *IEEE Trans. AP*, vol.43, 1995, pp.1375-1382.
- [12]. R.W. Scharstein, A.M.J. Davis, "Time domain three-dimensional diffraction by the isorefractive wedge," *IEEE Trans. AP*, vol.46, 1998, pp.1148-1158.
- [13]. P.M. Johansen, "Time domain version of the physical theory of diffraction," *IEEE Trans. AP*, vol.47, 1999, pp.261-270.
- [14]. A. Altintas, P. Russer, "Time domain equivalent edge currents for transient scattering," *IEEE Trans. AP*, vol.49, 2001, pp.602-606.
- [15]. K.S. Yee, "Numerical solution of initial boundary value problems involving Maxwell's equations in isotropic media," *IEEE Trans. AP*, vol.14, 1966, pp.302-307.
- [16]. A. Taflove, M.E. Brodwin "Numerical solution of steady-state electromagnetic scattering problem using the time-dependent Maxwell's equations," *IEEE Trans. MTT*, vol.23, 1975, pp.623-630.

- [17]. A. Taflove, M.E. Brodwin "Computation of the electromagnetic fields and induced temperatures within a model of the microwave irradiated human eye," IEEE Trans. MTT, vol.23, 1975, pp.888-896.
- [18]. G. Mur, "Absorbing boundary conditions for the finite difference approximation of the time domain electromagnetic field equations," IEEE Trans. EMC vol.23, 1981, pp.377-382.
- [19]. D.M. Sullivan, O.P. Gandhi, A. Taflove, "Use of the finite-difference time-domain method in calculating EM absorption in man models," IEEE Trans. Biomedical Engineering, vol.35, 1988, pp.179-186.
- [20]. X. Zhang, J. Fang, K.K. Mei, Y. Liu, "Calculation of dispersive characteristics of microstrips by the time-domain finite difference method," IEEE Trans. MTT, vol.36 1988, pp.263-267.
- [21]. R. Luebbers, F. Hunsberger, K. Kunz, R. Standler, M. Schneider, "A frequency-dependent finite-difference time-domain formulation for dispersive materials," IEEE Trans. EMC, vol.32 1990, pp.222-229.
- [22]. J.G. Maloney, G.S. Smith, W.R. Scott Jr., "Accurate computation of the radiation from simple antennas using finite-difference time-domain method," IEEE Trans. AP, vol.38 1990, 1059-1065.
- [23]. P.A. Tirkas, C.A. Balanis, "Finite-difference time-domain technique for radiation by horn antennas," 1991 IEEE APS vol.3, 1991, pp.1750-1753.
- [24]. S.M. El-Ghazaly, R.P. Joshi, R.O. Grondin, "Electromagnetic and transport considerations in subpicoseconds photoconductive switch modeling," IEEE Trans. MTT, vol.38, 1990, pp.629-637.
- [25]. A.C. Cangellaris, C.-C Lin, K.K. Mei, "Point-matched time-domain finite element methods for electromagnetic radiation and scattering," IEEE Trans. AP vol.35, 1987, pp.1160-1173.
- [26]. V. Shankar, A.H. Mohammadian, W.F. Hall, "A time-domain finite-volume treatment for the Maxwell's equations," Electromagnetics, vol.10, 1990, pp.127-145.
- [27]. N.K. Madsen, R.W. Ziolkowski, "A three-dimensional modified finite volume technique for Maxwell's equations," Electromagnetics, vol.10 1990, pp.147-161.
- [28]. J.S. Shang, "A characteristic-based algorithm for solving 3-D time domain Maxwell's equations," AIAA 30<sup>th</sup> Aerospace Sciences Meeting & Exhibit, NV, 1992.
- [29]. A. Taflove, Advances in Computational Electrodynamics, Artech House, MA, 1998.
- [30]. A. Taflove, Computational Electrodynamics: The Finite Difference Time Domain Method, Artech House, MA, 1995.
- [31]. K. Umashankar, A. Taflove, Computational Electromagnetics, Artech House, MA, 1993.

- [32]. M.N.O. Sadiku, Numerical Techniques in Electromagnetics, CRC Press, 1992.
- [33]. A. Taflove, K. Umashankar, "A hybrid moment method/finite difference time domain approach to electromagnetic coupling and aperture penetration into complex geometries," IEEE Trans. AP, vol.30, 1982, pp.612-657.
- [34]. K.S. Yee, J.S. Chen, "The finite difference time domain (FDTD) and finite volume time domain (FVTD) methods in solving Maxwell's equations," IEEE Trans. AP, vol.45, 1997, pp.354-363.
- [35]. Y. Wang, S. Safavi, S.J. Chaudhuri, "A hybrid technique based on ray tracing and FDTD method for site-specific modeling of indoor radio wave propagation," IEEE Trans. AP, vol.48, 2000, pp.743-754.
- [36]. A.C. Cangellaris, "Time domain finite methods for electromagnetic wave propagation and scattering," IEEE Trans. Magnetics, vol.27. 1991, pp.3780-3785.
- [37]. A.C. Cangellaris, D.B. Wright, "Analysis of the numerical error caused by the stair-stepped approximation of a conducting boundary in FDTD simulations of electromagnetic phenomena," IEEE Trans. AP, vol.39, 1991, pp.2883-2889.
- [38]. R. Holland, "Pitfalls of staircase meshing," IEEE Trans. EMC, vol.35, 1993, pp.434-439.
- [39]. D.E. Merewether, "Transients current on a body of revolution by an electromagnetic pulse," IEEE Trans. EMC, vol.13, 1971, pp.41-44.
- [40]. R. Holland, "THREDS: A finite-difference time-domain EMP code in 3D spherical coordinates," IEEE Trans. Nuclear Science, vol.30, No.6, 1983, pp.4592-4595.
- [41]. K.S. Kunz, K.M. Lee, "A three-dimensional finite difference solution of the external response of an aircraft to a complex transient EM environment: I- The method and its implementation," IEEE Trans. EMC, vol.20, 1978, pp.328-333.
- [42]. K.S. Yee, "A subgridding method for the finite difference time domain algorithm to solve Maxwell's equations," Tech. Report UCRL-96772, Lawrence Livermore National Laboratory, 1987.
- [43]. J.C. Kasher, K.S. Yee, "A numerical example of a 2-D scattering problem using a subgrid," Applied Comp. Electromag. Soc. J. and Newsletter, vol.2, 1987, pp.75-102.
- [44]. I.S. Kim, W.J.R. Hofer, "A local mesh refinement algorithm for the time domain finite difference method using Maxwell's curl equations," IEEE Trans. MTT, vol.38, 1990, pp.812-815.
- [45]. S.S. Zivanovic, K.S. Yee, K.K. Mei, "A subgridding method for the time domain finite difference method to solve Maxwell's equations," IEEE Trans. MTT, vol.39, 1991, pp.471-479.
- [46]. R. Holland, L. Simpson, "Implementation and optimization of the thin strut formalism in THREDE," IEEE Trans. Nuclear Science, vol.27, 1980, pp.1625-1630.

- [47]. J. Gilbert, R. Holland, "Implementation of the thin slot formulation in the finite difference EMP code THRED II," IEEE Trans. Nuclear Science, vol.28, 1981, pp.88-97.
- [48]. K.R. Umashankar, A. Taflove, B. Beker, "Calculation and experimental validation of induced currents on coupled wires in an arbitrary shaped cavity," IEEE Trans. AP, vol.35, 1987, pp.1248-1257.
- [49]. A. Taflove, K.R. Umashankar, B. Beker, H.F. Harfoush, K.S. Yee, "Detailed FDTD analysis of electromagnetic fields penetrating narrow slots and lapped joints in thick conducting screens," IEEE Trans. AP, vol.36, 1988, pp.247-257.
- [50]. R. Holland, "Finite difference solution of Maxwell's equations in generalized nonorthogonal coordinates," IEEE Trans. Nuclear Science, vol.30, No.6, 1983, pp.4589-4591.
- [51]. J.A. Stratton, Electromagnetic Theory, NY, McGraw-Hill, 1941.
- [52]. M. Fusco, "FDTD Algorithm in curvilinear coordinates," IEEE Trans. AP, vol.38, 1990, pp.76-89.
- [53]. M. Fusco, M.V. Smith, L.W. Gordon, "A three-dimensional FDTD algorithm in curvilinear coordinates," IEEE Trans. AP, vol.39, 1991, pp.1463-1471.
- [54]. J.-F. Lee, R. Palandech, R. Mittra, "Modelling three-dimensional discontinuities in waveguides using nonorthogonal FDTD algorithm," IEEE Trans. MTT, vol.40, 1992, pp.346-352.
- [55]. M. Celuch-Marcysiak, W.K. Gwarek, "Generalized TLM algorithms with controlled stability margin and their equivalence to finite difference formulations for modified grids," IEEE Trans., MTT, vol.43, 1995, pp.2081-2089.
- [56]. K.S. Yee, J.S. Chen, A.H. Chang, "Conformal finite-difference time-domain (FDTD) with overlapping grids," IEEE Trans. AP, vol.42, 1992, pp.1068-1075.
- [57]. T.G. Jurgens, A. Taflove, K.R. Umashankar, "Finite difference time domain modeling of curved surfaces," IEEE Trans. AP, vol.40, 1992, pp.357-366.
- [58]. S. Dey, R. Mittra, "A technique for implementing the FDTD algorithm for on a nonorthogonal grid," IEEE Microwave and Guided Wave Lett., vol.14, 1997, pp.213-215.
- [59]. N. Madsen, "Divergence preserving discrete surface integral methods for Maxwell's equations using nonorthogonal unstructured grids," J. Comp. Physics, vol.119, 1995, pp.34-45.
- [60]. S. Gedney, F. Lansing, "Full wave analysis of printed microstrip devices using a generalized Yee algorithm," Proc. IEEE AP Soc. Int. Symp. 1993, pp.1179-1182.
- [61]. C. Rowell, V. Shankar, W.F. Hall, A.H. Mohammadian, "Algorithmic aspect and computing trends in computational electromagnetics using massively parallel architectures," Proc. IEEE Conf. on Algorithms and Architectures for Parallel Processing, Brisbane, Australia, 1995.

- [62]. E.A. Navarro, C. Wu, P.Y. Chung, J. Litva, "Some considerations about the finite difference time domain method in general curvilinear coordinates," *IEEE Trans. Microwave and Guided Wave Lett.*, vol.4, 1994, pp.396-398.
- [63]. S.L. Ray, "Numerical dispersion and stability characteristics of time-domain methods on nonorthogonal meshes," *IEEE Trans. AP*, vol.41, 1993, pp.233-235.
- [64]. J. Fang, *Time Domain Finite Difference Computation for Maxwell's Equations*, PhD dissertation, University of California at Berkeley, Berkeley, CA, 1989.
- [65]. M. F. Hadi, M. Picket-May, "A modified FDTD (2,4) scheme for modeling electrically large structures with high phase accuracy," *IEEE Trans. AP*, vol.45, 1997, pp.254-264.
- [66]. J.B. Cole, "A high accuracy realization of Yee algorithm using nonstandard finite differences," *IEEE Trans. MTT*, vol.45, 1997, pp.158-165.
- [67]. Q. H. Liu, "The PSTD algorithm: A Time domain method requiring only two cells per wavelength," *IEEE Trans. Microwave and Optical Technology Lett.*, vol.15, 1997, pp.158-165.
- [68]. M. Krumpholz, L. P. B. Katehi, "MRTD: New time domain schemes based on multiresolution analysis," *IEEE Trans. MTT*, vol.45, 1997, pp.385-393.
- [69]. S. Wang, F.L. Teixeira, "A three-dimensional angle-optimized finite difference time domain algorithm," *IEEE Trans. MTT*, vol.51, 2003, 811-817.
- [70]. G.D. Smith, *Numerical Solution of Partial Differential Equations*, Oxford University Press, 1978.
- [71]. A. Bayliss, E. Turkel, "Radiation boundary conditions for wave-like equations," *Comm. Pure Appl. Math.* Vol.23, 1980, pp.707-725.
- [72]. B. Engquist, A. Majda, "Absorbing boundary conditions for the numerical simulation of waves," *Mathematic of Computation*, vol.31, 1977, pp.629-651.
- [73]. R.L. Higdon, "Absorbing boundary conditions for difference approximations to the multi-dimensional wave equation," *Mathematics of Computation*, vol.47, 1986, pp.437-459.
- [74]. R.L. Higdon, "Numerical absorbing boundary conditions for the wave equation," *Mathematics of Computation*, vol.49, 1987, pp.65-90.
- [75]. Z.P. Liao, P.L. Wong, B.P. Yang, Y.F. Yuan, "A transmitting boundary for transient wave analyses," *Scientia Sinica (series A)*, vol.XXVII, 1984, pp.1063-1076.
- [76]. J.P. Berenger, "A perfectly matched layer for the absorption of electro-magnetic waves," *J. Computational Physics*, vol.114, 1994, pp.185-200.
- [77]. D.S. Katz, E.T. Thiele, A. Taflove, "Validation and extension to three dimensions of the Berenger PML absorbing boundary condition for FD-TD meshes," *IEEE Microwave and Guided Wave Letters*, vol.4, 1994, pp.268-270.

- [78]. I.N. Sneddon, Elements of Partial Differential Equations
- [79]. S.M. Rao, Time Domain Electromagnetics, Academic Press, 1999.
- [80]. R. Courant, D. Hilbert, Methods of Mathematical Physics, Interscience Pub., 1962
- [81]. A.H. Mohammadian, V. Shankar, W.F. Hall, "Computation of electro-magnetic scattering and radiation using a time domain finite volume discretization procedure," Computer Physics Communication, Vol.68, 1991, pp.175-185.
- [82]. J.S. Shang, "Characteristic-based algorithm for solving the Maxwell's equations in the time domain," IEEE AP Magazine, Vol.37, 1995, pp.15-23.
- [83]. R.F. Warming, R.M. Beam, "Upwind second order difference schemes and applications in aerodynamics flows," AIAA Journal, vol.14, 1976, pp.1241-1249.
- [84]. J.S. Shang, D. Gaitonde, "Characteristic-based time dependent Maxwell equation solvers on a general curvilinear frame," AIAA Journal, vol.33, 1995, pp.491-498.
- [85]. J.P. Donohoe, J.H. Beggs, M. Ho, "Comparison of finite difference time domain results for scattered EM fields: Yee algorithm vs. a characteristic based algorithm," IEEE APS Int. Symp., 1995, pp.325-328.
- [86]. J.S. Shang, "A fractional step method for solving 3D time domain Maxwell's equations," Journal of Comp. Physics, vol.118, 1995, pp.109-119.
- [87]. D. Jiao, J-M. Jin, "Characteristic based time domain method for electro-magnetic analysis," IEEE APS. Int. Symp. 2000, pp.753-756.
- [88]. J.H. Beggs, W.R. Briley, "An implicit characteristic based method for electromagnetics," NASA/TM-2001-210862, Langley Research Center, VA.
- [89]. R. Courant, K. Friedrichs, H. Lewy, "On the partial differential equations of mathematical physics," IBM Journal, vol.11, 1967, pp.215-237.
- [90]. J.H. Beggs, "A linear bicharacteristic FDTD method," IEEE APS Int. Symp. 2001.
- [91]. J.H. Beggs, "2-D linear bicharacteristic FDTD method" IEEE APS Int. Symp. 2003
- [92]. M. Kline, I.W. Kay, Electromagnetic Theory and Geometrical Optics, Inter-science Publishers, 1965.
- [93]. R.W. Lewis, "Discontinuous initial value problems for symmetric hyperbolic linear differential equations," J. Math. Mech. 7, 1958, pp.571-592.
- [94]. J.B. Keller, "Geometrical acoustics I, the theory of weak shock waves," J. App. Physics 25, 1954, pp.938-947.
- [95]. F.G. Friedlander, Sound Pulses, Cambridge University Press, Cambridge, 1958.

- [96]. R.W. Lewis, "Asymptotic expansion of steady state solutions of hyperbolic differential equations," pp.593-628.
- [97]. R. Courant, Differential and Integral Calculus, vol.I, John Wiley and Sons, NY, 1937.
- [98]. C-S. Shin, R. Nevels, "Optimizing the Gaussian excitation function in the finite difference time domain method," IEEE Trans. Education, vol.45, 2002, pp.15-18.
- [99]. J.B. Schneider, C.L. Wagner, "FDTD dispersion revisited: faster than light propagation," IEEE Microwave and Guided Wave Letters, vol.9, 1999, pp.54-56.
- [100]. A. Taflove, S.C. Hagness, Computational Electrodynamics, 3<sup>rd</sup> edition, Artech House, 2005.
- [101]. S.C. Chapra, R.P. Canale, Numerical Methods for Engineers, McGraw-Hill, 1990.
- [102]. A. Sommerfeld, Partial Differential Equations in Physics, NY, Academic press, 1949.
- [103]. W.C. Chew, Waves and Fields in Inhomogeneous Media, Van Nostrand Reinhold, 1990.
- [104]. A.K. Dominek, L. Peters, W.D. Burnside, 'An additional physical interpretation in the Luneburg-Kline expansion,' IEEE Trans. AP, vol.35, 1987, pp.406-411.
- [105]. D.M. Sullivan, Electromagnetic Simulation Using the FDTD, IEEE Press, 2000.

## **CURRICULLUM VITA**

### **PERSONAL INFORMATION**

Nationality: Turkey ( TC)

Birth Place and Date: 20 January 1971, Ankara

### **EDUCATION**

MS METU in Electrical and Electronics Engineering 1995

BS METU in Electrical and Electronics Engineering 1993

(high honors, with CGPA 3.78/4.00)

Maltepe Askeri Lisesi Izmir 1989

(top first, 1/450)

### **WORK EXPERIENCE**

2003- Present Havelsan-Boeing, Seattle, WA, USA

Sr. Systems Engineer: Turkish AEWACS program

1998-2003 TAI-TUSAS, Ankara, Turkey

Sr. Design Engineer: Avionics, EMI/EMC, and Radar

1993-1998 ASELSAN, Microwave & Systems Technologies Group, Ankara, Turkey

R&D Engineer: RF/Microwave, telecommunication

### **FOREIGN LANGUAGES**

Advanced English, Medium German

### **HOBBY**

Gourmet, Sports, Nature, Turkish History, Military, Literature and Music.